POLITECNICO
MILANO 1863

SCUOLA DI INGEGNERIA INDUSTRIALE
E DELL'INFORMAZIONE

Executive Summary of the Thesis

Design Modelling and Mechanical/Acoustic Experimental Characterization of Piezoelectric Micro-Ultrasound Transducers

Laurea Magistrale in Materials Engineering and nanotechnology - Ingegneria dei materiali e delle nanotecnologie

Author: Matteo Colosio

Advisor: Prof. Alberto Corigliano

Co-advisor: Gianluca Massimino, Marco Soldo, Domenico Giusti and Pedro Haro Garcia

Academic year: 2020-2021

1. Introduction

In the last several decades, ultrasounds have found ever-expanding industrial and biomedical applications, such as non-destructive evaluation (NDE), medical imaging and finger-printing recognition at frequencies ranging from tens of kilohertz to hundreds of megahertz. Among the several ways to excite ultrasound waves, the most common one is the piezoelectric effect. Piezoelectric Micromachined Ultrasonic Transducers (PMUTs) are layered diaphragms that exploit this effect to emit and receive ultrasound perturbation. This thesis deals with 4x4 array of circular transducers with removal of passivation layers to avoid instability phenomena such as buckling and reduce as much as possible the cross-talk between membrane (see Fig.1). They are used for in-air application with performing resonance frequency of 140 kHz. The engine of the device is a thin piezoelectric film ($1\mu m$) made of PZT (Lead Zirconate Titanate) and it is deposited through a sol-gel technique. The main purposes of the thesis are to model and characterize the mechanical and acoustic behavior of these device. First of all, the deformed static deformation both of the membranes and the whole device are measured by means of topography measurements using Polytec MSA500 and then such configuration is simulated through finite element models using Comsol Multi-physic 5.6. This non flat shape is due to the residual stresses introduced by the fabrication process and moreover its variation as a function of the DC voltage applied is determined. Then the frequency response of the membranes is evaluated: its first six modes of vibration are computed both experimentally and with modelling simulation. Once the deformed initial configuration and the resonance frequency of the first piston-like mode are known, the following analysis deals with the oscillation ring down of the vibration in air and in vacuum. Even in this case a comparison between model and experimental evidences is proposed: unlike the previous Comsol model, this one will include several physics such as Solid mechanics, Electrostatic, Piezoelectricity, Pressure acoustic and Structure-fluid interaction. Thanks to this measurement, the damping characterizing the device (Q factor) is evaluated by changing the surrounding fluid. In addition, in presence of air, the intensity of the emitted acoustic field is determined at 2 cm above the membrane and

it will be compared with the experimental pressure level. Lastly, the presence of the unwanted cross-talk between membranes within the same die is experimentally demonstrated. This last phenomena shows its contribution both by causing the oscillation of the close membranes and by affecting the frequency response. It is evaluated in vacuum and air in order to divide the acoustic and mechanic contribution. The executive summary is organize as follows. In the second section, the sample under investigation is introduced in terms of geometry and materials constituting the layered membrane. After that, the following section is aimed at describing the numerical models: the 3D model of a single membrane and the 3D model of the whole device with all their features are presented. In section 4, first the topography and vibrometry experimental measurements and set-up will be discussed. Finally the simulation and experimental results will be shown in parallelism to validate or not the models and then as a closing section a brief conclusion is proposed [1] [2] [3].

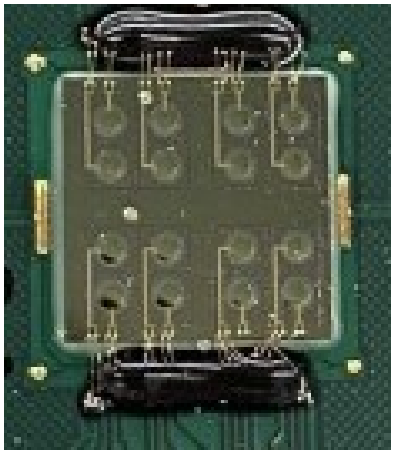

Figure 1: Picture of the whole die.

2. Sample Description

The whole die is a Silicon rectangular box with dimensions 6950 μm x 6950 μm and thickness equal to 400 μm containing 16 membranes with diameter of the cavity equal to 860 μm. The layered membrane has a total thickness of 6.84μm and thus the aspect ratio diameter/thickness is equal to 125.7. The structural layer is Polycristalline Silicon with a thickness of 4 μm and the circular PZT layer, having a diameter equal to 600 μm, is deposited co-axially with that. Additionally, an important feature of this device is the open back cavity of each membrane.
Each layer of the PMUTs is characterized by a certain amount of fabrication induced residual stresses: this altered stress state is responsible of the deformed static configuration. The layered stack of the membrane is shown in Fig.2.

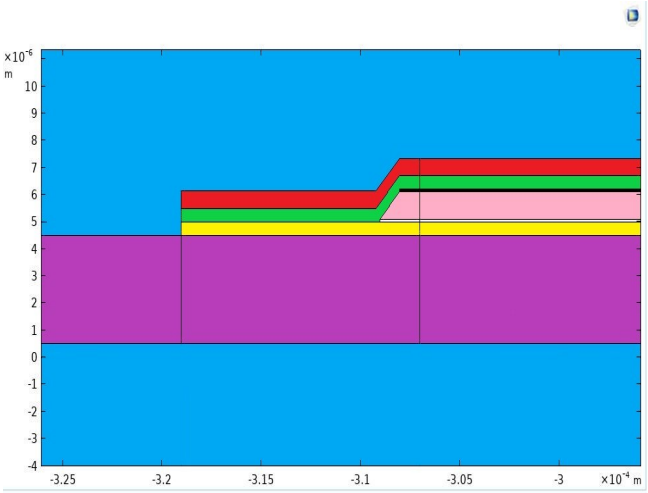

Figure 2: Cross-section of the layered stack over the cavity. The violet layer is the Polysilicon, the pink one represents the PZT while the others are different passivation layers.

3. Modelling simulation

This section is focused on describing the models used to simulate the single membrane PMUT and the entire die. In particular, the single membrane is devoted to the investigation of the membrane's deformation and its resonance frequencies while the second one is aimed at simulating the die's deformation, oscillation ring down and the acoustic pressure propagation. Indeed, the oscillation ring down analysis can not be performed with the single membrane because it does not reproduce properly the boundary conditions.
Starting from the single membrane, the geometry and the selected mesh are shown in the Fig.3 and 4. Concerning the meshing step, it is realized by using tetrahedral elements belonging to the serendipity family and the size is chosen by means of an iterative process in order to balance accuracy and computational cost. The model includes only the solid domain and the physics involved are the structural mechanics, electrostatic and piezoeletricity. All materials layers are governed from elastic equations except the piezoelectric layer which is described

by the electro-mechanics coupled equations with the stress-charge dependence. The boundary condition and the residual stress levels are added in the structural nodes.

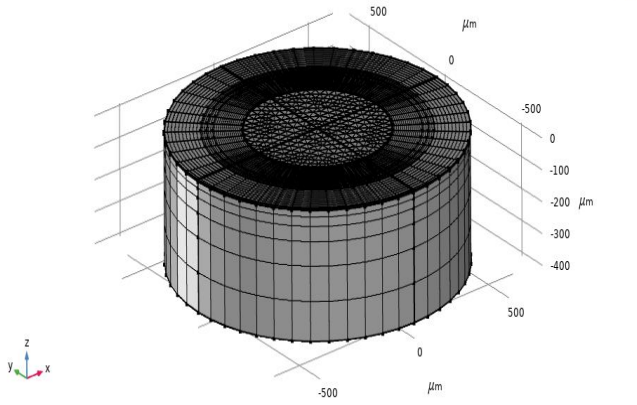

Figure 3: View of the single membrane with the selected mesh.

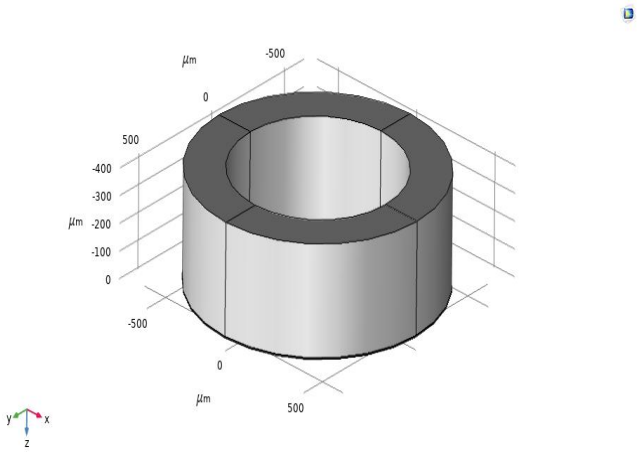

Figure 4: View of the membrane's cavity.

The boundary condition consists of a clamped condition onto the bottom surface of the Silicon substrate while the stresses are different for each layer and they can be compressive or tensile. Moreover, in order to simulate the application of a DC voltage and an AC harmonic one, it is needed to introduce an electric DC voltage and a AC voltage in the electrostatic node. The AC voltage will be used in the modal analysis and it has an amplitude equal to 0.1V while the following values of DC voltage will be applied: 5, 10, 15 and 20V. The model includes the stationary study and the eigenfrequency pre-prestressed ones.

As regards to the second model, it takes into account the whole die and the presence of the fluid domain. In Fig.5 and in Fig.6, the geometry and mesh of the solid domain and fluid one are shown.

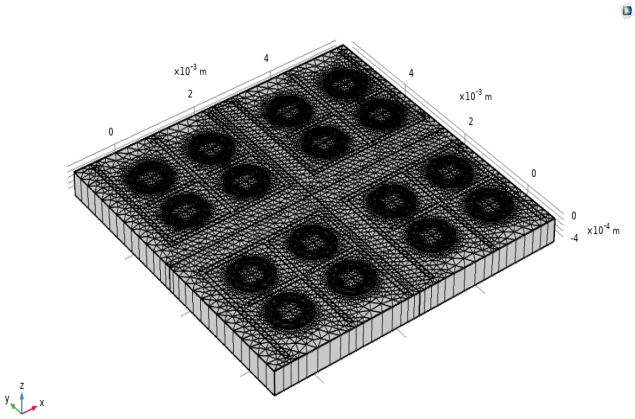

Figure 5: Geometry and mesh of all the die.

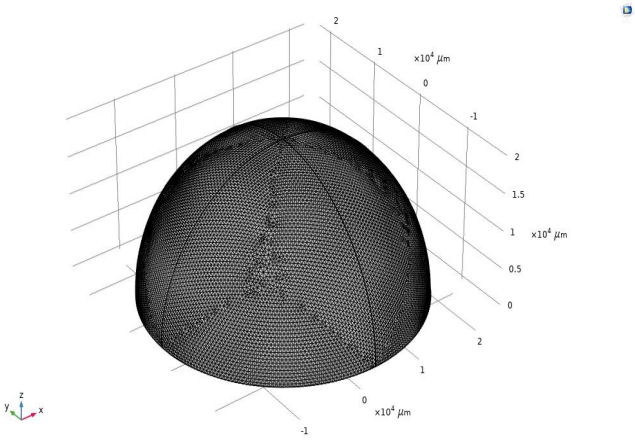

Figure 6: Meshing of the fluid domain over the die.

The meshing step of the solid part follows the same iterative approach while the fluid one has to consider the wavelength of the emitted acoustic field. The maximum size of the mesh must be equal to $\lambda/6$ and considering the relation with the sound velocity it will be:

$$\frac{c}{6 \cdot f} = \frac{343\frac{m}{s}}{135kHz \cdot 6} = 4.23 \cdot 10^{-4}m \qquad (1)$$

In addition to the previous model, the Pressure acoustic physics is considered to simulate the presence of air: this domain does not consider viscous losses and it only behaves as a fluid

through which a linear acoustic field can propagate. To simulate the presence of air or vacuum and their different damping effect on the membrane's vibration, the damping loss factors for each layer are added together with a thin-film damping at the interface between structure and fluid (the second contribution only in air). Always regarding the fluid domain, a condition of spherical wave radiation is applied onto the external surface: in this way all the outcoming acoustic waves are not reflected back. At this point, the electro-mechanical-acoustic response of the system is computed by applying a single sinusoidal pulse at the resonance frequency of the first mode. The signal is centered in 4V DC and it has an AC voltage having amplitude equal to 4V.

4. Experimental characterization

The experimental characterization is performed by using Polytec MSA500 in topography and vibrometry configuration. By means of the first operational mode the static deformation of the membranes and the whole device is measured. The physical set-up and an example of Polytec image output is shown in Fig.7 and 8. Once the deformation at 0V is computed, the next step is to measure the displacement variation of the membrane as a function of the DC voltage applied. In order to do that a DC power generator is connected to the membranes through the proper pins: the values of voltage applied are 5, 10, 15 and 20V.

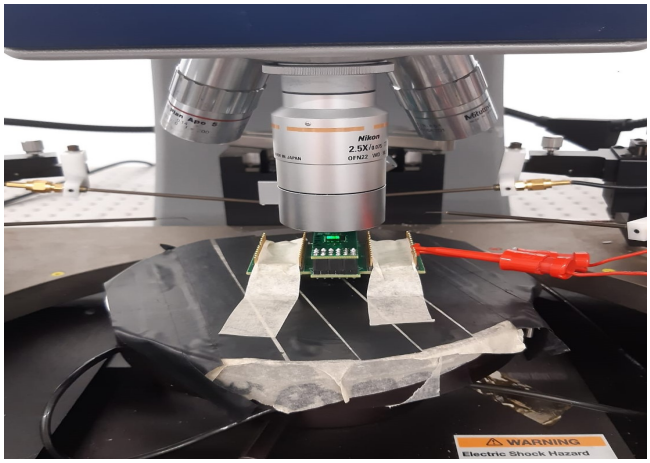

Figure 7: PMUTs sample under the microscope objective.

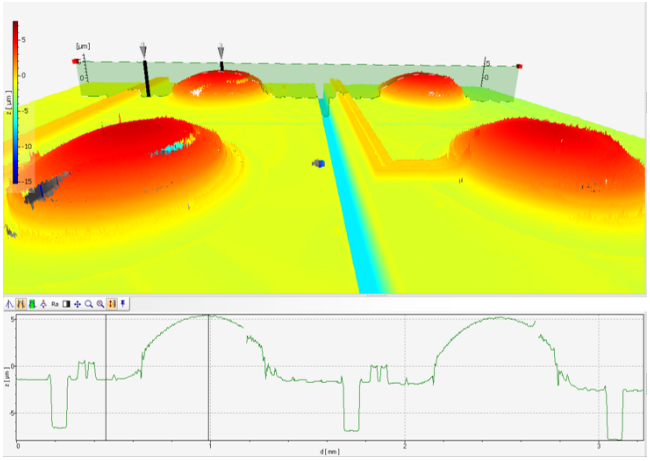

Figure 8: Topography image of the membranes.

The second experimental campaign deals with the small dynamic signal (AC voltage 0.1V) to measure the resonance frequency of the membranes and the oscillation Ring down by applying an AC dynamic signal having amplitude equal to 4V. Both investigation are carried out with Polytec MSA500 in laser doppler vibrometer configuration. Concerning the small signal analysis, it is performed in the interval of frequency ranging from 100 kHz up to 450kHz: this interval contains the first six modes of vibration. For the first mode (see Fig.9), the one used in application, its variation as a function of the DC voltage applied is measured.
The oscillation ring down analysis is realized with the same physical set-up but changing the driving voltage: single sinusoidal pulse with amplitude equal to 4V centered in 4V DC. The measurements will be done with two different surrounding fluids: air and vacuum (10^{-5}Pa).

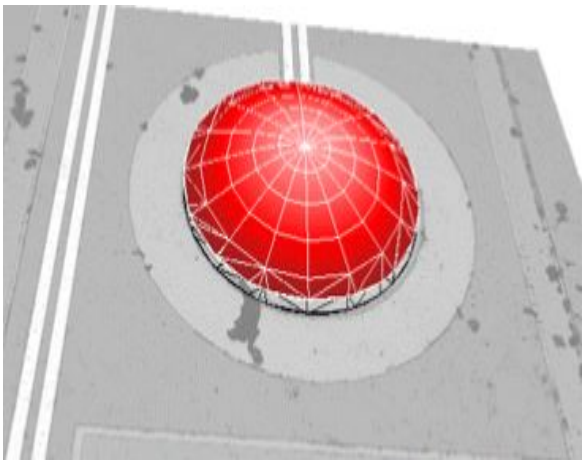

Figure 9: Fist mode of vibration of the membrane at 140kHz.

In addition to the measurements of the ring down of the activated membrane, the experimental investigations of the cross-talk between close membranes is carried out. The oscillation of one membrane can put in motion the other ones and modify the frequency response: the analysis is performed both in air and vacuum to divide the mechanic and acoustic contributions. In this case the approach is based on dividing the 16 membranes in 4 quadrant, activate the central membrane of the quadrant with a single pulse signal 4V DC and 4V AC and then measure the displacement of all the membranes belonging to the quadrant.

5. Experimental and Numerical results

In this section the main results of the several investigations are resumed. Starting from the experimental deformation of the membranes and its variation upon the application of a DC voltage, the analysis is done on all the membranes within die and the average results of the displacement of the membrane's centre are shown in Table1. Moreover, the results of the Comsol simulation model are pointed out in the same table and in Fig.10 the deformed profile is shown.

Displacement of the membrane's centre

	Experimental	Simulation
0V	7.04 μm	7.21 μm
5V	5.9 μm	6.23 μm
10V	5.15 μm	5.5 μm
15V	4.85 μm	4.72 μm
20V	3.77 μm	3.54 μm

Table 1: Displacement of the membrane's centre in z^+ direction.

Because of the the residual stresses induced by the fabrication process, the membranes have a upward initial configuration. Applying a voltage the stress state of the piezoelectric layer changes for electro-mechanical coupling behavior and the deformed tends to flatten. A good match between simulation and experimental evidences is obtained: the piezoelectric model and the residual stress values inserted in the model correctly simulate the static and piezoeletric behavior of the device.

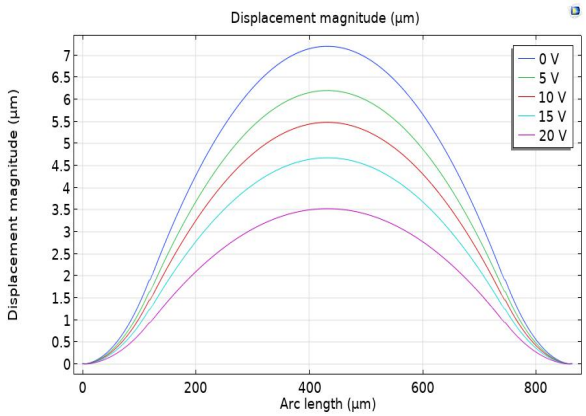

Figure 10: Deformed profile of the 3D single membrane model at different values of DC voltage applied.

The second static measurements deals with the deformed of the whole device. This does not change with the DC voltage and the main causes are the fabrication process and the curing process of the epoxy glue with which the die is attached on the Printed Circuit Board (PCB). In order to simulate the real deformation, the boundary conditions used are the following: clamped vertices, Wrinkler's springs to simulate the glue on the edges and a superficial load directed toward z^+ axis. After an iterative approach to define the stiffness of the springs and the intensity of the load, the simulated die properly fits the real deformation. In Fig.11 the result is shown.

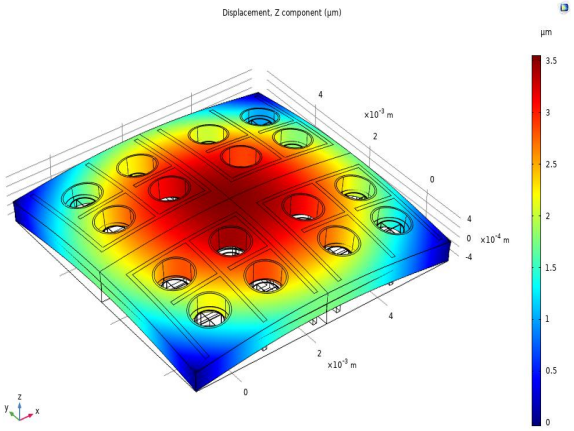

Figure 11: Deformed shape of the entire die. It is chosen to show the silicon substrate only to make more visible its deformation.

Once the deformed shape is well simulated, the following analysis concerns the frequency analysis. The experimental average values of the first six modes of vibration at OV DC are the following: 140.9, 206.4, 215.4, 321, 324.3 and 386.3 kHz. Moreover, the dependence of the resonance frequencies as a function of the DC voltage applied was investigated. It is noted that the frequencies of all the modes decrease as the DC voltage increases: the electro-mechanical coupling reduce the initial state stress and the structure becomes less rigid. Similarly to all the activity, the experimental evidence are compared with the simulation results obtained through the eigen-frequency pre-stressed study performed with Comsol. Within this document, only the comparison between the experimental and simulated frequencies of the first mode is shown (Fig.12).

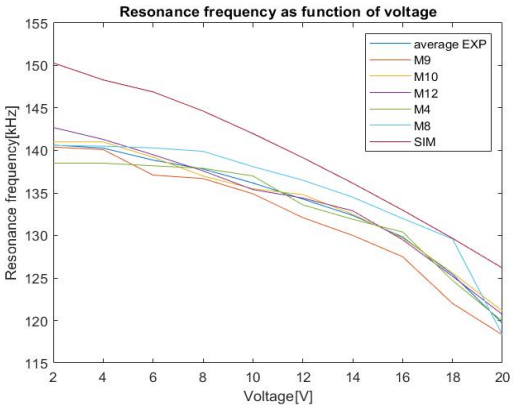

Figure 12: Comparison between the resonance frequencies of the 1^{st} mode of vibration.

Looking at the graph a good match between the simulation and experimental value is obtained: considering the variability of the fabrication process an error lower than 10% is acceptable.
At this point, the attention moves toward the analysis of the oscillation ring downs. The obtained results are shown in Fig.13 and 14 for air and vacuum respectively. Starting from the vibration of the membrane's centre, the Q factor parameter is measured by means of the exponential fitting of the oscillation and logarithmic decrement: both gives the same results. The Q factor values obtained are summarized in Table 2 together with the maximum amplitude of the oscillation (peak-peak). The results have contrasting feedback: the damping is simulated quite well both in air and in vacuum by the loss factors and the thin-film damping condition while on the other hand the amplitude of displacement shows a high mismatch.

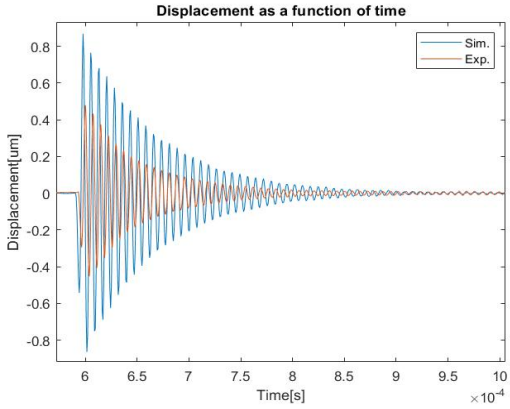

Figure 13: Ring down comparison in air.

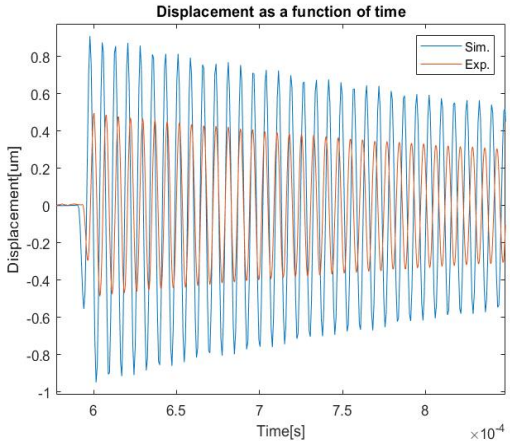

Figure 14: Ring down comparison in vacuum.

Ring down in air and vacuum

	Experimental	**Simulation**	Error%
Q (air)	22	27	18.5
Amp.(air)	921[nm]	1834[nm]	50
Q(vacuum)	182	208	12.5
Amp.(vacuum)	973[nm]	1850[nm]	47

Table 2: Displacement of the membrane's centre in z^+ direction.

Concerning the error of the displacement amplitude, the reason is related to the piezoelectric linear model implemented in the software. Un-

like the previous static case, in a dynamic regime where an AC voltage is applied over the time, the model is not able anymore to simulate the real behavior. In order to overcome this limit a new non linear hysteric model is mandatory and it must be built starting from the typical polarization curves of the PZT.
Moreover, by exploiting this analysis the cross-talk is measured both in vacuum and in air. It is noted that the close membranes experience an oscillation even if they are not activated. This oscillation related to the interaction of the membranes is much higher in air than in vacuum. This evidence allows us to consider the acoustic cross-talk component higher than the mechanical one. The presence of this phenomena gives another justification of the mismatch observed in the displacement's amplitude because part of the energy used to activate one membrane is lost to put in motion the other ones.
Lastly, hereinafter the acoustic pressure is analyzed. In Fig.15, the sound pressure over time measured at 2cm above the activated membranes is shown.

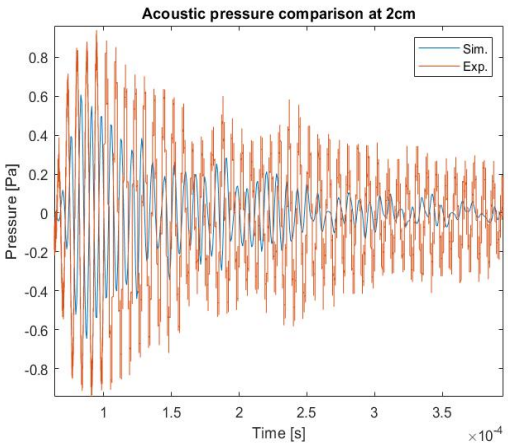

Figure 15: Comparison of the sound pressure [Pa] at 2cm over the activated membrane.

Looking at the previous graph, a mismatch between the experimental and simulated pressure is evident. Conversely to the oscillation ring down, in this case the experimental pressure overestimates the simulated one. This evidence can be explained by considering again the cross-talk oscillation of the other membranes. Indeed, the simulation is not completely able to reproduce this phenomena and the acoustic perturbation emitted by the unwanted oscillations of the close membranes interferes positively with the emitted acoustic field by the activated one and in turn the pressure intensity increases. A new model able to simulate the cross-talk phenomena should be built or on the other hand the cross-talk phenomena should be avoided. Some possibilities are to close the cavities to avoid the communication intra-membranes or to maintain the open cavities with a better modelling of the chambers to simulate the communication through the back side.

6. Conclusion

Taking into account the initial purposes of the activity, the following closing remarks can be done. The static characterization, frequency analysis and their variations upon the application of a DC voltage are performed with satisfactory results. On the other hand, the dynamic behavior must be improved both in term of displacement and acoustic pressure. In particular, the cross-talk has to be taken into account because its presence reduces the experimental displacement and increases the measured acoustic pressure. The former consequence is due to the energy losses to put in motion the other membranes (not all the electric energy is exploited by activated membrane) while the latter is related to the constructive interference between the acoustic perturbation of the activated membrane and the acoustic field emitted by the other ones for the cross-talk. In addition, another future development aimed at improving the matching in dynamic regime concerns the modification of the piezoelectric constitutive model. Instead of the linear model, a new hysterical nonlinear model must be built starting from the typical polarization curves.

7. Acknowledgements

First of all, I thank the company STMicroelectronics for giving me the opportunity to work in a group of talented and competent people. It has been a formative and amazing experience which taught me how to approach a research activity. In particular, my most sincere thanks goes to Marco Soldo, Domenico Giusti, Cristina D'Argenzio and Fabio Quaglia. Moreover, I would like to thank Prof.Alberto Corigliano and Dott.Gianluca Massimino for their advises and support during all the activity and Prof. Pedro Haro Garcia for the for the help and patience.

Lastly, I thank my family for the continuous support.

References

[1] Alberto Corigliano, Raffaele Ardito, Claudia Comi, Attilio Frangi, Aldo Ghisi, and Stefano Mariani. *Mechanics of Microsystems*. John Wiley & Sons, 2017.

[2] G. Massimino, L. D'Alessandro, F. Procopio, R. Ardito, M. Ferrera, and A. Corigliano. Air-coupled pmut at 100 khz with pzt active layer and residual stresses: Multiphysics model and experimental validation. In *2017 18th International Conference on Thermal, Mechanical and Multi-Physics Simulation and Experiments in Microelectronics and Microsystems (EuroSimE)*, pages 1–4, 2017.

[3] Yongqiang Qiu, James V. Gigliotti, Margeaux Wallace, Flavio Griggio, Christine E. M. Demore, Sandy Cochran, and Susan Trolier-McKinstry. Piezoelectric micromachined ultrasound transducer (pmut) arrays for integrated sensing, actuation and imaging. *Sensors*, 15(4):8020–8041, 2015.

Politecnico di Milano

School of Industrial and Information Engineering

Master of Science in Materials Engineering and Nanotechnology

Design Modelling and Mechanical/Acoustic Experimental Characterization of Piezoelectric Micro-Ultrasound Transducers

Supervisor: Prof. Alberto Corigliano
Supervisor: Prof. Pedro Haro Garcia
Supervisor: Dr. Ing. Gianluca Massimino
Supervisor: Dr. Ing. Marco Soldo
Supervisor: Ing. Domenico Giusti

Master thesis of:
Matteo Colosio
928425

Academic Year 2020-2021

Abstract

This master thesis is realized in STMicroelectronics thanks to a collaboration between the company and Politecnico di Milano. The activity is aimed at modelling and experimentally characterizing a Piezoelectric Micro-machined Ultrasound Transducer (PMUT). This is a new generation MEMS (Micro Electro Mechanical System) able to send and receive ultrasound waves by exploiting the piezoelectric effect: here the attention will be focused on the sending mode only. Throughout all the activity a continuous comparison between numerical simulation and experimental results is proposed. This approach is the typical work flow to launch a product into the market. The design modelling is done by using the finite element software COMSOL Multiphysics 5.6 while the laboratory campaign is carried out through Polytec MSA500 and other electronic equipment. The analysis performed are mainly focused on investigating the static and dynamic mechanical behavior of the device and only as a closing section the emitted acoustic field has been considered. Concerning the mechanical characterization, the main fields of investigation are the deformed configurations both of the single membrane and the whole device, the resonance frequencies of the membranes, the dynamic oscillation and the cross-talk phenomena through which the membranes within the same die can interact. Starting from the distorted geometry of the membranes, this is due to the fabrication process which introduces residual stresses and in turn causes a non flat configuration of the membrane: it is noted that the initial upward deformation flattens by applying an increasing DC voltage. Similarly, even the deformation of the die is caused by the presence of residual stresses. Going on, the modal analysis is performed: the first six modes are evaluated to have a complete characterization but the only one exploited in applications is the first one, having a frequency equal to 140kHz. Once the frequency is known, a dynamic analysis is carried out. The membranes are activated by means of a single sinusoidal voltage signal at the resonance frequency and the oscillation ring down is analyzed. Thanks to these measurements, it has been possible to measure the damping of the device by computing the Q factor. This is carried out in presence of Air and Vacuum and the values obtained are respectively 22 and 182: in this way the fluid and mechanic contributions to the damping are divided. Furthermore, by studying the oscillation ring down it appears the need to develop a non linear hysterical piezoelectric model to simulate the dynamic behavior of PZT layer: it will be part of the future activity. Subsequently, the presence of the undesired phenomena of cross-talk has been experimentally investigated. Because of this effect, the membranes can interact each other and the oscillation of one membrane can put in motion the close ones. The analysis has been performed in vacuum and air: it is noted that the acoustic contribution to the cross-talk has a higher influence and in particular the communication occurs through the back cavities. The last part of the thesis is devoted to the acoustic measurements of the emitted field in terms of directionality and sound pressure level. The radiation pattern of the emitted acoustic field by the

membrane is simulated by means of a 2D axysimmetric model. Moreover, the pressure intensity has been evaluated at 2cm over the membrane both through simulation and experimentally: a mismatch is noted and it is due to the inability of the model to consider the oscillation cross-talk of the other membranes. From here comes the second future development to be investigated: the emitted acoustic field considering the oscillation of the other membranes or avoid the cross-talk by changing the design of the device, i.e closing the cavity at the bottom of the membranes.

This thesis is the starting point of future activities aimed at modelling the non linear hysterical piezoelectric behavior to better match the dynamic response and studying the cross-talk effect in the acoustic emission.

Sommario

Questa tesi di Laurea Magistrale è realizzata in Stmicroelectronics grazie ad una collaborazione tra l'azienda e il Politecnico di Milano. L'attività è finalizzata alla modellazione e alla caratterizzazione sperimentale di un micro trasduttore ad ultrasuoni piezoelettrico (PMUT). Si tratta di un MEMS (Micro Electro Mechanical System) di nuova generazione in grado di inviare e ricevere onde ultrasoniche sfruttando l'effetto piezoelettrico: qui l'attenzione è focalizzata sulla sola modalità di invio. Durante tutta l'attività viene proposto un confronto continuo tra simulazione numerica e risultati sperimentali. Questo approccio è il tipico flusso di lavoro per introdurre un prodotto nel mercato. La modellazione numerica viene effettuata utilizzando il software ad elementi finiti COMSOL Multiphysics 5.6 mentre la campagna sperimentale di laboratorio viene effettuata tramite Polytec MSA500 insime ad altre apparecchiature elettroniche. L'analisi effettuata è principalmente focalizzata sullo studio del comportamento meccanico statico e dinamico del dispositivo e solo nel capitolo di chiusura è stato analizzato il campo acustico emesso. Per quanto riguarda la caratterizzazione meccanica, i principali campi d'indagine sono le configurazioni deformate sia della singola membrana che dell'intero dispositivo, le frequenze di risonanza delle membrane, l'oscillazione dinamica e i fenomeni di cross-talk attraverso i quali le membrane all'interno dello stesso die possono interagire tra loro. A partire dalla geometria distorta delle membrane, questa è dovuta al processo di fabbricazione che introduce tensioni residue e a sua volta provoca una configurazione non piatta della membrana: si nota che la deformazione iniziale verso l'alto si appiattisce applicando una tensione CC crescente. Allo stesso modo, anche la deformazione dell'intero dispositivo è causata dalle tensioni residue. Proseguendo, l'analisi modale viene eseguita per conoscere le frequenze di risonanza: primi sei modi di vibrazione sono valutati per avere una caratterizzazione completa ma l'unico sfruttato in applicazione è il primo, con una frequenza pari a 140 kHz. Una volta che la frequenza è nota, viene effettuata un'analisi dinamica. Le membrane vengono attivate mediante un singolo impulso sinusoidale di tensione alla frequenza di risonanza e a seguire viene analizzato lo smorzamento dell'oscillazione. Grazie a queste analisi è stato possibile misurare lo smorzamento del dispositivo calcolando il fattore Q. La misura viene effettuata sia in presenza di aria che in vuoto: in tal modo vengono divisi i contributi fluidi e meccanici dello smorzamento. I valori ottenuti di Q per aria e vuoto sono rispettivamente 22 e 182. Inoltre, studiando lo smorzamento della vibrazione appare la necessità di sviluppare un modello piezoelettrico isteretico non lineare per simulare il comportamento dinamico dello strato di PZT: questo sarà parte dell'attività futura. Successivamente, la presenza di fenomeni indesiderati di cross-talk è stata analizzata sperimentalmente. A causa di questo effetto, le membrane possono interagire tra loro e l'oscillazione di una membrana può mettere in movimento quelle vicine. Anche in questo caso, l'analisi è stata eseguita in vuoto e nell'aria: si è notato che il contributo acustico ha un'influenza maggiore e in particolare la comunicazione avviene

attraverso le cavità posteriori. L'ultima parte della tesi è dedicata alle misurazioni acustiche del campo emesso in termini di direzionalità e livello di pressione sonora. Il radiation pattern del campo acustico emesso dalla membrana viene simulato mediante un modello assial-simmetrico 2D. Inoltre, l'intensità della pressione in funzione del tempo è stata valutata a 2 cm sopra la membrana sia attraverso simulazione che sperimentalmente: si osserva un disallineamento che è dovuto all'incapacità del modello di considerare il fenomeno di cross-talk. Da qui nasce il secondo sviluppo futuro, il quale dovrà investigare il campo acustico emesso tenendo in considerazione l'oscillazione delle altre membrane o annullarlo cambiando design del dispositivo, i.e chiudendo la cavità inferiore delle membrane.

Questa tesi è il punto di partenza di attività future volte a modellare il comportamento piezoelettrico isteretico non lineare e studiare l'effetto del cross-talk nell'emissione acustica.

Contents

List of Figures

List of Tables

Chapter 1

Introduction

1.1 Thesis objective

Micro Electro Mechanical System (MEMS) are emerging devices that almost inevitably influence our daily life. They are based on Silicon and integrated circuit's fabrication processes and nowadays they are used in a lot of fields ranging from automotive, augmented reality, consumers application up to medical equipment. Their main advantages, that have ensured a rapid expansion and use, are the miniaturization of the device which enables an easy integration in many technologies, the low cost and mass production and finally the possibility to couple electro-mechanical proprieties. This master thesis has been carried out in the company STMicroelectronics and this amazing and formative experience has been possible thanks to the strong collaboration between the society and the Department of Civil and Environmental Engineering of Politecnico di Milano. Both are leaders in their working field and having regard to the developments and future needs in the semiconductor sector they are increasing even more their relations. In the specific, I was introduced into a skilled and multidisciplinary team composed from an electronic engineer, a design engineer, a product development engineers and a master student with which I shared the job. We all have worked together and have added our own knowledge to the research activity with a continuous interaction and collaboration with the academical counterpart. It is worth to say that this master thesis will be discussed not only in Politecnico di Milano but also in the Universidad de Sevilla as part of a double degree program. The main aims are simulate by means of finite element models the experimental mechanical and acoustic evidences detected through the experimental characterization. In particular the initial part is related to the analysis of the static deformation through topography test and to the investigation of the resonance frequencies of the device. After that, the discussion moves on the dynamic response of the device: in such a way it is possible to measure the damping parameter (Q factor) and to investigate the cross-talk between different membranes. These last tests are performed both in air and in vacuum to divide the acoustic contributions to these phenomena. Once the device is completely characterized mechanically, the following steps concern the acoustic measurements of the ultrasound field emitted. Among the several information, the attention is paid to the sound pressure level and to the directionality of the acoustic field.

1.2 Work organization

First, a general introduction is provided in Chapter 2 about MEMS technology where the main devices and fabrication processes are described. Within the same chapter, the discussion moves towards an overview of the PMUTs, the main character of the thesis, whose working principle and the main manufacturing characterization processes are analyzed.

The third chapter of the manuscript deals with piezoeletricity. Initially, a description of the electrical-mechanical coupled behavior characterizing the piezoelectric effect is proposed and then the discussion moves on the atomic structure that characterizes the main piezoelectric materials. Once the crystalline structure is introduced, a detailed presentation of the PZT layer (Lead Zirconate Titanate) used in the device under examination is proposed along with the main deposition technique. Finally, the last part of the chapter is dedicated to the derivation of the main equations that govern the behavior of these materials and that will be used in COMSOL models to simulate their effect.

The fourth chapter concerns the description of the acoustic phenomena. First of all, the acoustic field is introduced and then the mathematical linear model to describe its physics is derived. Even in this case the equations discussed will be the same used in the numerical modelling.

After these chapters related to the state of the art of technology and the main equations involved in their working principle, attention is paid to the experimental campaign and modelling. The initial part of the fifth chapter is aimed at presenting the design of the device and its main features; then a description of the experimental equipment (Polytec MSA500) and the finite element software is proposed (COMSOL Multi-physics). All the rest of the chapter is dedicated to the introduction of experimental set-up and simulation models used for each study carried out. Firstly, the mechanical studies are introduced and then the acoustic one. In particular the chapter will describe the analysis by following this scheme: static deformation of the membrane, static deformation of the whole die, frequency analysis of the membrane, oscillation ring down, cross-talk and finally sound pressure level measurements.

The sixth chapter resumes all the results obtained for each investigation introduced in the previous chapters. After this, a critical discussion of the results obtained and the future works to be done are proposed in the last chapter of the thesis.

Chapter 2

Overview of PMUTs

The aim of this chapter is to introduce the MEMS (micro-electro-mechanical system) technology in terms of products, fabrication processes and possible applications. After this brief introduction, the discussion moves toward the piezoelectric micro-ultrasounds transducer (PMUT) whose working principle, specific fabrication processes and applications will be discussed.

2.1 Introduction to MEMS

A MEMS is an integrated system able to couple and combine the electrical and mechanical properties and interact with the surrounding environment. They are usually produced together with an application specific integrated circuit (ASIC), whose purpose is to control the electrical input and read out the electrical output in order to get environmental information. The former ability to receive an electrical signal coming from the ASIC and translate it into a mechanical stimulus toward the environment defines the actuator working principle. On the other hand, when the device is subjected to an environmental perturbation (pressure, inertial forces, humidity, ultrasounds) then the sensor working principle is exploited: the device transforms the physical information into an electrical signal and the ASIC reads it out giving back some information related to the environmental stimulus. Thanks to the double capabilities through which these devices can interact with the external environment, the MEMS technology perfectly fits with the increasing demand of interconnected devices able to guarantee the needs of the nowadays famous paradigm 'Internet of Things'.

Let us analyse the acronym MEMS to have a deep insight into the technology:

- **Micro**: it refers to the characteristic dimensions of these devices. Actually, the size of the smallest MEMS part may also be at the submicrometer scale and the complete packaged device ASIC-MEMS can achieve the size of some mm pointing out the multi scale nature of this objects. Some scientist are trying to overcome the micro going down to the nanoscale (i.e. exploiting 2D materials [1]) but at that characteristic size a lot of limitations arise due to fabrication process and nonlinear dynamic behaviour. Nonetheless, even at the microscale these devices allow an exceptional integration in huge amount of common life smart products such as phones, glasses, watches and cars.

- **Electro**: it highlights the need to have electric and electronic component. As introduced before, this is a crucial characteristic in order to interact with the exterior environment and

can be done exploiting electronic components or materials such as the piezoelectric one, in which the electric domain is inside the material itself. It will be seen that the latter is the one used in the PMUT tecnology.

- **Mechanical**: This characteristic defines the need to have some mechanical components: this portion of the device is the one directly in relation with the environments. For instance in accelerometers, the mechanical portion is represented by micro plates and beam that are load by inertial forces or in case of PMUT is a thin film layered membrane able to oscillate if activated or if impressed by an acoustic ultrasonic wave.

- **System**: it refers to the complexity of the product. MEMSs have to integrate a lot of components and so these devices represent complex systems: as a consequence the fabrication process becomes more and more difficult.

2.1.1 MEMS products and fabrication process

Nowadays the MEMS technology covers a huge amount of possible applications and it is playing a more and more crucial role in emerging technologies. Among others the main products are accelerometers, gyroscopes, pressure sensors, gas sensors, ink jet printers head, micro-mirror for augmented reality and CMUTs/PMUTs.

The first two devices are strictly related to the inertial forces affecting a mass inside the MEMS box; accelerometers enable to measure a linear acceleration while the gyroscopes allow to compute the angular velocity exploiting the Coriolis force: by combining a 3 axis accelerometer, 3 axis gyroscopes and a 3 axis magnetometer has been possible to build a 9 axis sensor in a MEMS volume of only 10.5 mm^3 [2]. Accelerometeres and Gyroscopes are used a lot in automotive industry and thanks to their limited dimensions are being used for some customers applications such as drone control and image stabilizer in mobile phone's camera.

Moving on to the other products, their working principle is not affected by the inertial forces and they can be classified depending on their operational mode: sensor MEMS able to measure pressure and gas concentrations and actuator MEMS that thanks to piezo or capacitive activation system can put in motion their movable parts and interact with the environment. PMUT is located in the middle between these two classes due to its ability to work on both modes.

During their development, the MEMS technology experienced a great advantage that allowed to assert itself very quickly: all the devices belonging to MEMS family can be produced using the already existing fabrication processes used for the electronic devices and integrated circuits such as surface silicon micromachinig and bulk silicon micromachinig including lithography, electrodeposition, PVD (physical vapor deposition), CVD (chemical vapor deposition), molding and chemical etching.

Basically, the fabrication process for current micro systems starts with the production of a mono crystal Silicon wafer with a diameter up to 12 inch through Czochralski method. Once the wafer is obtained, a specific sequence of material layers is deposited above it by means of various possible technique. Each added layer has a defined thickness and a role in the design and behaviour of the whole device. Besides the deposition step, the fabrication of micro system is characterised by another crucial phase which is the selective elimination of portions of one or more deposited layer: the so called lithography process.

This last step is the core of this technology and it allows to engrave the desired geometry by removing the undesired portions by alternating photoactivation and etching phases.

The main steps of this process can be resumed as follow (Fig.2.1):

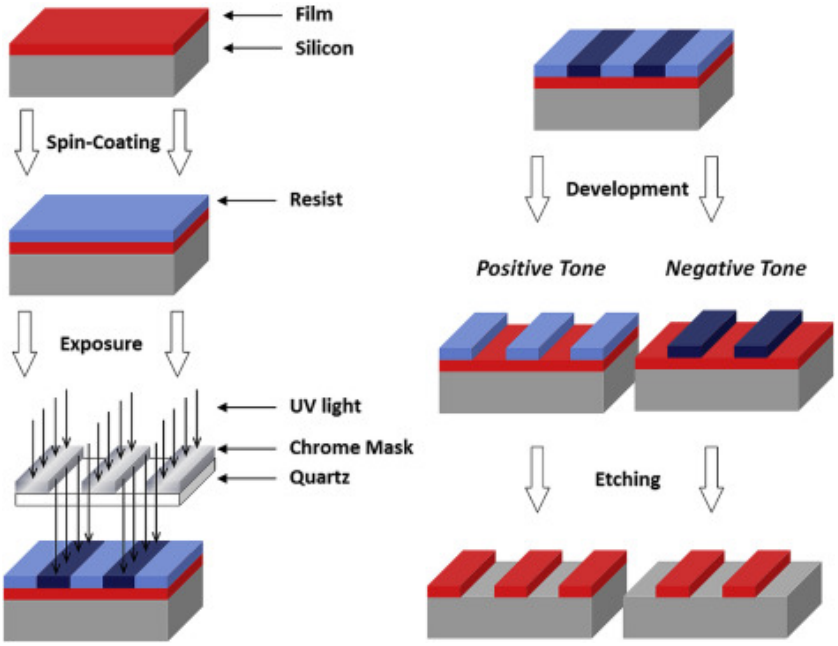

Figure 2.1: *General work flow of the photolitography process [3].*

It is worth to add some comments regarding this kind of process:

- Due to the huge variety of products and the flexibility and complexity of the process each semiconductor company has developed an own ad hoc method. Specifically the company STMicroelectronics uses the so called ThELMA^{TM} (Thick Epipoly Layer for Microactuators and Accelerometers)[4].

- In micro system fabrication, it is possible to remove material layers below some pre-deposited layers and then get suspended portions of the structure that are usually the movable parts.

- Once the patterned wafer is obtained, a second wafer is produced, usually with an easier design, to be used as a cap of the whole device. In order to paste together the two pieces a wafer-to-wafer bonding must be performed.

- During the process different materials are coupled together and they experience several thermal cycle: the mismatch of the thermal properties causes residual stresses which in turn can deform the structure. As will be analyzed in chapter 4, this issue is experienced by the device under study; indeed, the PMUT membrane in static regime is not flat but it shows an upward deformation.

- By the fact MEMS dimensions are very small, it is possible to pattern many device on the same wafer: it brings many advantages in terms of cost reduction and yield improvements.

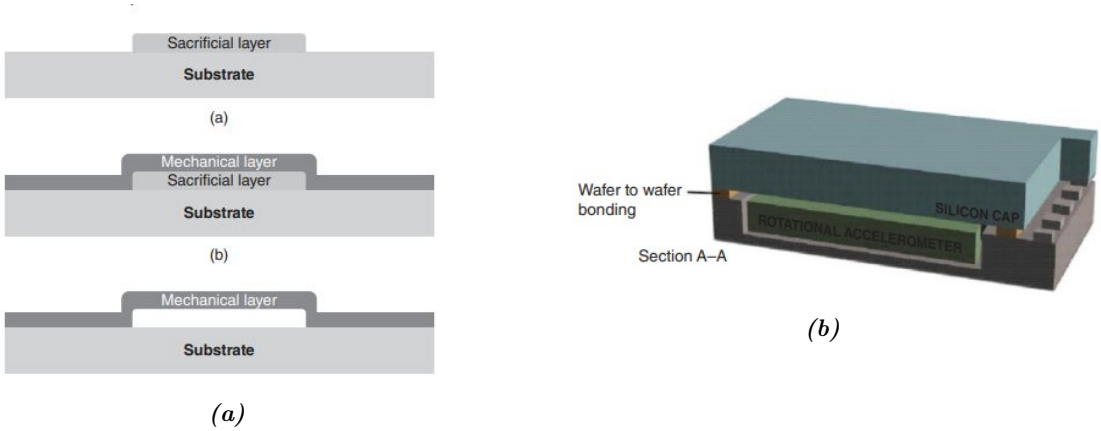

Figure 2.2: *a) Simplified example of a suspended structure obtained through a lithographic process. b) Geometry of the cross section of two wafers glued together.[5]*

2.2 PMUTs

PMUTs (Piezo Micro-machined Ultrasound Transducers) are devices able to send and receive ultrasound waves having a frequency above the conventional limit of 20 kHz by exploiting respectively the converse and direct piezoelectric effect. They are an emerging technology and they mainly could be used as a rangefinder and in medical imagining to carry out ultrasounds scans guaranteeing a great reduction of the product cost. In comparison with CMUT (Capacitive Micro-machined Ultrasound Transducer) and bulk wave resonator, that represent the actual technology used to perform these scopes, the PMUTs differ in terms of working principle with the former and dimensions with the latter.

The possibility to use the micro fabrication processes enables the production of layered structures with a total thickness of the order of 10-20 μm where it is included a piezoelectric layer (few μm thick) between two electrodes. The piezo layer actually represents the engine of the whole device: applying an AC voltage through the electrode it is possible to cause a deformation of the laminated membrane and in turn the propagation of an acoustic wave. Conversely, in case of deformation due to accidental waves a potential variation will be detected. In the next chapter, the piezoelectric effect, the most common materials used and lastly the different techniques usable to deposit the piezoelectric layer will be explained in details, as well as how they can affect the properties of the material. The layered membrane is clamped on the edges and its first mode of vibration can be compared with the movement of a piston: the vibration matches properly with the impedance of the possible propagating mediums such as water and air and its frequency value depends on the medium and it will be of the order of tens MHz for water and hundreds kHz for air.

In the following sections of the chapter a deeper analysis of the working principle, the possible fabrication processes and applications will be described.

2.2.1 Working principle

PMUTs can be considered as a clamped disk or membrane and their elastic energy is strictly related to the out-of plane bending. In converse piezoelectric effect, the bending momentum is

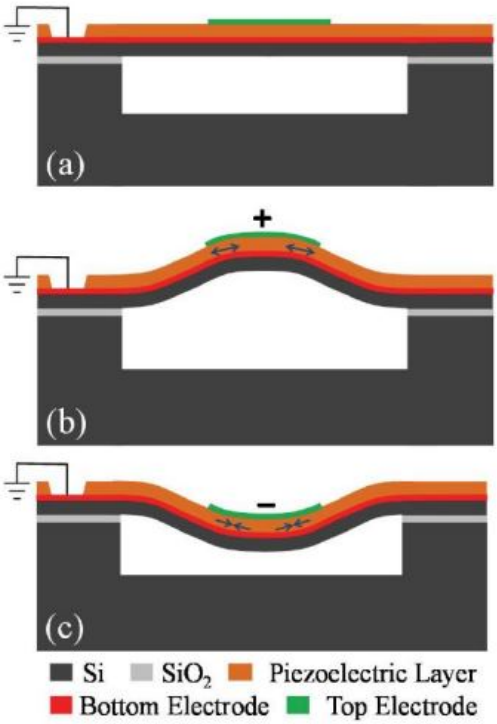

Figure 2.3: *Working principle in the direct piezoelectric mode. a) Static situation without residual stresses; b) Positive voltage at the bottom electrode; c) Negative voltage at the bottom electrode [6].*

.

provided by the electric field across the piezoelectric layer through its electro-mechanical coupled intrinsic behavior that converts the electric energy into a mechanical one (Fig.2.3); conversely, in the direct piezoelectric effect the bending momentum is provided by an incident ultrasound wave. From structural mechanics theory [7], the resonance frequency of the first vibration mode f_R of a circular, clamped and homogeneous plate is given by the following formulae:

$$f_R = \frac{(3.19)^2}{2\pi a^2}\frac{Et^2}{12(1-\nu^2)\rho} = \frac{(3.19)^2}{2\pi a^2}(\frac{D}{\mu})^{\frac{1}{2}}, \tag{2.1}$$

$$D = \frac{Et^3}{12(1-\nu^2)}, \tag{2.2}$$

$$\mu = \rho t, \tag{2.3}$$

where a and t are respectively the radius and thickness of the plate; E, ν and ρ are the Young's Modulus, the Poisson's ratio and the density of the plate; D is the bending rigidity of the plate; and μ the mass per plate area.[8]

In the case of multi-layer plates or membrane, Eq. 2.1 has to be modified in order to consider varying material constants. For that purpose, the position of the neutral plane must first be

determined under the hypothesis that this position coincides with the stress center. Denoting by z the height above the bottom surface of the plate, t_n the thickness of the n_{th} layer finishing at height $h_n = \sum_{k=1}^{n} t_k$ (see Fig. 2.4), and $se(n)$ the relevant compliance term of the n_{th} layer, the stress center is obtained as:

$$Z_s = \frac{1}{2} \frac{\frac{h_n^2 - h_{n-1}^2}{se(n)}}{\frac{t_n}{se(n)}} \tag{2.4}$$

In the previous equations, it must be considered that the term $se(n)$ depends on the position in the plate: at the centre it assumes a value different than that on the edges. In case of clamped plates and with the hypothesis of almost equal Poisson's ratio for all the layers the following assumption can be done : $se(n) = se_{11}(n)$ where $se_{11}(n)$ is the term 11 of the compliance matrix for the n_{th} layer. [8] [9] Taking into account this last consideration the equations 2.2 and 2.3 will become as follow:

$$D = \frac{1}{3} \sum \frac{(h_n - z_s)^3 - (h_{n-1} - z_s)^3}{s_{11}^{(n)}(1 - (\nu_{12}^{(n)})^2)} \tag{2.5}$$

$$\mu = \sum \rho_n t_n \tag{2.6}$$

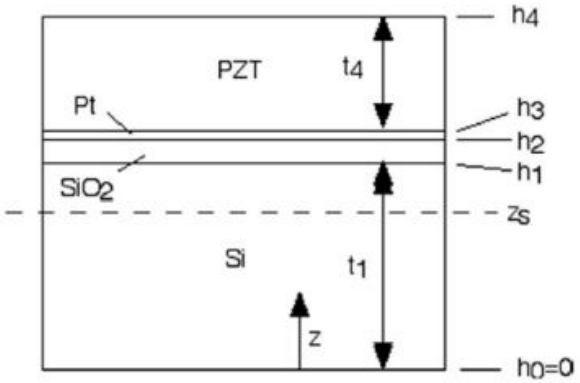

Figure 2.4: *Cross section of a single PMUT membrane.[8]*

By substituting the last Eq. 2.5 and Eq. 2.6 in the Eq. 2.1, it is possible to compute the resonance frequency of a layered clamped plate.

Looking at the Eq. 2.1, the resonant frequency of the diaphragm is strictly controlled by changing the diameter of the diaphragm (the terms is raised to the square) and for that it is useful to investigate their relation. In the Fig. 2.5 are shown the frequencies corresponding to the first fourth vibration modes as a function of the membrane diameter computed through a finite element analysis (FEA): a higher diameter implies a lower resonance frequency. [10]

In addition, it is worth to point out that the resonance frequency is related to the residual stress state as well. As a matter of fact, the presence of stresses due to the fabrication process not only affects the initial deformation of the membrane but it also influences the geometric stiffness of the device and in turn the resonance frequency as appears in the Eq.2.1 [11].

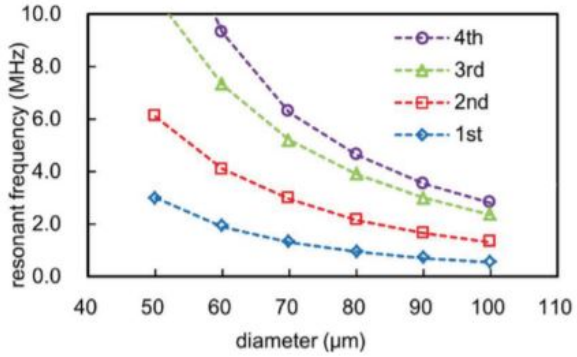

Figure 2.5: *Calculated resonant frequencies with changing the diameter of the PMUTs for various resonant modes.[10]*

In the layered structure of the PMUT membrane, these residual stresses are mainly due to the mismatch between the thermal expansion coefficients of the several materials: a designer can either avoid the overall effect of residual stresses by adding material layers for stress compensation or consider the residual stress as a part of the design space. A PMUT can behave predominantly like a membrane or a plate depending on the relative magnitude of initial tension (residual stress integrated over the thickness) and the flexural rigidity of the device. Although the net residual stress could be either tensile or compressive, it is better to have a tensile state stress because PMUTs with significant net compressive stress are likely to suffer from buckling related reliability issues in addition to sudden lowering of resonant frequency [12][13].

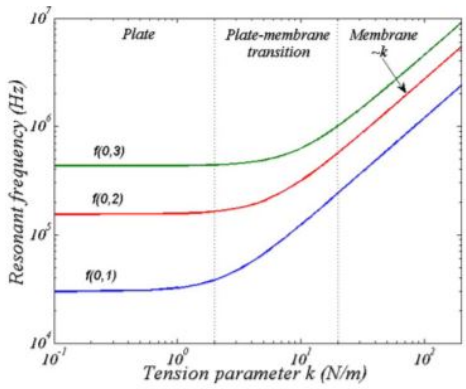

Figure 2.6: *Resonance frequency of the first three fundamental modes as a function of k in case of an overall tensile stress; the higher is k, the higher is the stress state. [13]*

2.2.2 Fabrication processes of PMUTs

In this subsection, two of the main important fabrication processes of PMUTs will be described: specifically attention will be focused on the diaphragm defined through sacrificial layer releasing and back-side etching.

- **Sacrificial layer releasing**: This method is probably the main used one and as the name says it implies the preparation of a sacrificial layer on the substrate. Once the completed and patterned layered stack is obtained, the sacrificial layer will be removed by etching through a small openings to form a cavity below the membrane: for the sake of clarity it must be remembered that for each hole it is possible to remove at most 6 μm of material horizontally. In Fig. 2.7 the production of ZnO-based PMUTs array with a low temperature oxide (LTO) as a sacrificial layer is resumed [3]:

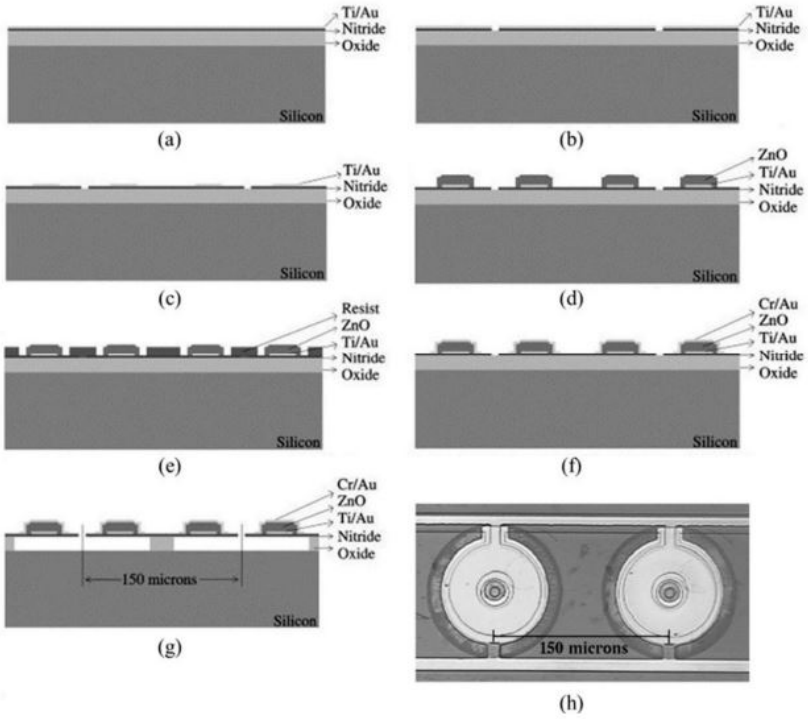

Figure 2.7: *Typical sacrificial layer work flow [3].*

.

Firstly, a) a layered structure composed by LTO, Silicon Nitride and the Ti/Au electrode is obtained above the Silicon substrate; in the second step b), the small openings for releasing are defined through wet etching of the eletrode and plasma etching of the Si_3N_4; after patterning of the bottom electrode c), a thick layer of ZnO is deposited above it and then patterned by wet etching d); in e) and f) the deposition and patterning of the Cu/Au top electrode is shown: in order not to add the layer on undesired portion a resist was previously deposited; Finally the LTO layer is etched g) and in the last image a top view of two adjacent membrane is shown.

In this example a ZnO was used as a active material but other thin film piezoelectric materials such as PZT, AlN can also be adopted. However, limitations still exist regarding the lateral etching rate of the sacrificial layer and the compatibility of the membrane stack with the etching processes for the sacrificial layers. Indeed, a wet etching process implies a low directional removal of the selected layer but at the same time an high selectivity; vice-

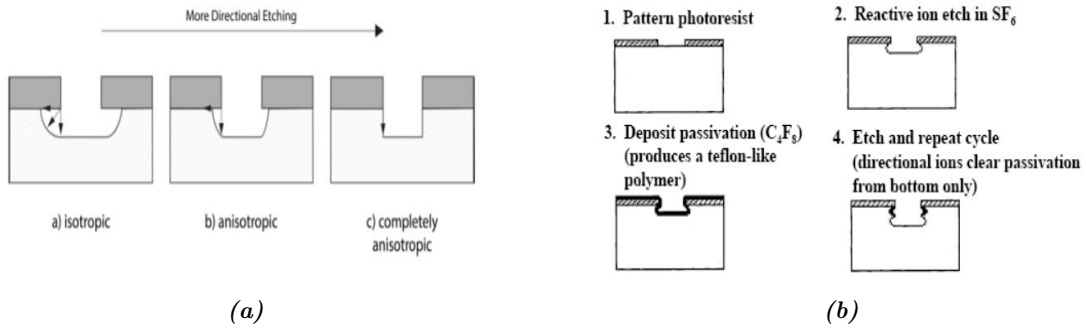

Figure 2.8: *a) Comparison of etching profile obtained with different level of directionality. b) DRIE work flow.*

versa the dry etching is characterized by a high level anisotropy but poor selectivity (Fig, 2.10a): a plasma etching characterised by the presence of reactive chemical components (selectivity) and Ionic component (directionality) perfectly accomplishes both purpose at the same time.

- **Back side etching**: An alternative is to define the diaphragm with back-side etching. The etching step itself can take place either before deposition of the piezoelectric layer or after completing the whole membrane stack. An example of this former process is proposed in the Fig.2.9.

  The first two steps of the work flow,namely high temperature oxidation and Boron diffusion, are performed to prepare the substrate and to reduce the stress state. After these, the actual back etching process begins:

  1. First of all, oxidation at low temperature (850°C) for 2 hours followed by the removal of oxide layer on the bottom surface through a buffered oxide etchant.

  2. Wet silicon etching in order to create the membrane: low directonality.

  3. Deposition of the Pt bottom electrode using a sputtering process.

  4. Fabrication of the Piezoelectric layer of PZT (Lead Zirconate Titanate) by means sol-gel deposition.

  5. The last step is the deposition of the Au top electrode followed by the patterning process.

  Even in this process, one of the disadvantages is the anisotropic etching and the creation of 54.7° sloping sidewalls [14]. This limits the minimum size of diaphragm and the pitch of the transducer array the process can create (the pitch is the distance between the centre of two adjacent membranes). Therefore, the back-side etching in current devices is usually performed with deep reactive-ion etching (DRIE), obtaining relatively perpendicular side walls and in turn a high aspect ratio. As can be notice in Fig.2.8b, the vertical side wall are not completely smooth but they show a roughness: the challenge is to reduce as much as possible this surface irregularity.

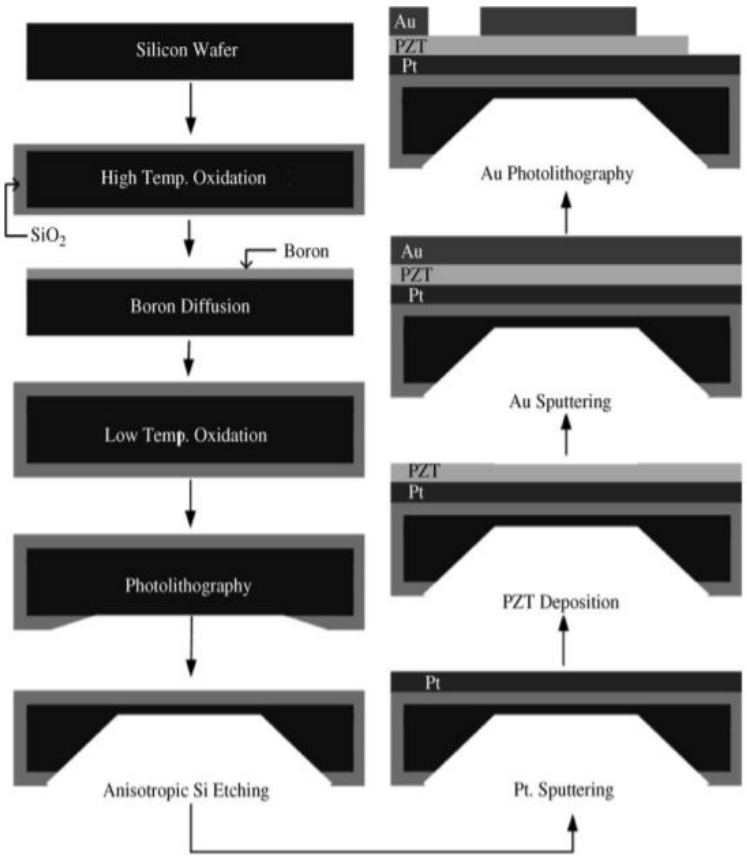

Figure 2.9: *Work flow of the back etching process [15]*

.

2.2.3 Applications and characterising features

The last subsection of this chapter is devoted to an overview of the possible applications and in relations to these what properties must be guaranteed. As already introduced in the previous part of this thesis, the PMUTs' applications are extremely varied and they can range from consumers usage such as rangefinder (exploiting Time of Flight), gesture recognition, presence detection, fingerprinting scanner to medical application as in case of medical imaging, pregnancy monitoring, dental cleaning, neuro-functional imaging and flow meter (Fig. 2.10).

Each of this application could be obtained by changing the PMUTs parameters (geometry, materials and single membrane or array/matrix) in order to modify the three main specific properties of these device: resonance frequency, Q factor and possibility of performing steering of the ultrasound waves (beam forming). As seen before, the resonance frequency is strictly related to the geometry of the PMUTs (mainly the diameter), and in general its value is determined and conceived depending on the applications and on the medium through which the ultrasounds wave have to propagate. Considering the impedance mismatch between the membrane and the medium, in order to maximize the transmitted wave and avoiding a decay along the distance it is advisable to use a frequency around hundreds of kHz for air and tens of MHz for water and

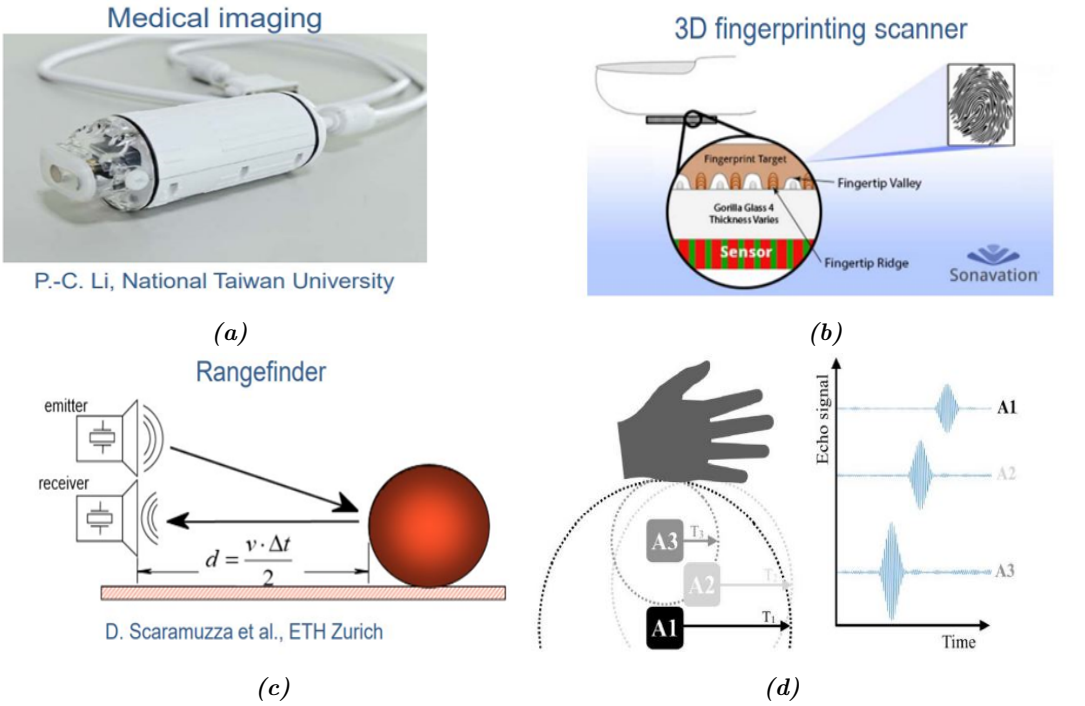

Figure 2.10: *Some examples of PMUTs applications: a) medical imaging b) fingerprinting scanner c) range finder and d) gesture detection.[16]*

human tissue applications.

Regarding the second characterizing property of the PMUTs, the Q factor, it is the inverse of the damping and it is strictly related to the bandwidth of the signal: the more dampened is the oscillations of the membrane and the wider will be the bandwidth and in turn the smaller will be the Q factor. Analytically, it can be measured as the ratio between the resonance frequency and the frequency range at -3 dB of the resonance frequency's amplitude. Its values is not an intrinsic characteristic of the device since it can change significantly by modifying the environmental pressure and so the damping contributions coming from the fluid (Fig. 2.11). In addition to the fluid damping, the Q factor also depends on the solid damping contributions such as:

1) Thermoelasticity related to the velocity of deformation and to the irreversible heat transfer due to cooling of the parts subjects to dilation and heating of parts subjects to compression. In case of thermoelasticity, in the elastic equation must be added the thermal dependent terms.

2) Anchor losses: due to this phenomena part of the vibrational energy of the membrane is transmitted to the substrate. This damping component becomes important when the substrate is not perfectly elastic and the fluid and thermoelasticity damping has already reduced as much as possible.

In relation to the application, the desired Q factor value can change: a low value implies a strong damping effect on the vibration of the membrane while a high value of Q factor determines a low damping and so the membrane continues to oscillate with an higher amplitude for a larger period of time. In the former case the device could be exploited as a rangefinder where the membrane has to receive the echo of the sent wave without oscillating anymore; in the latter, a

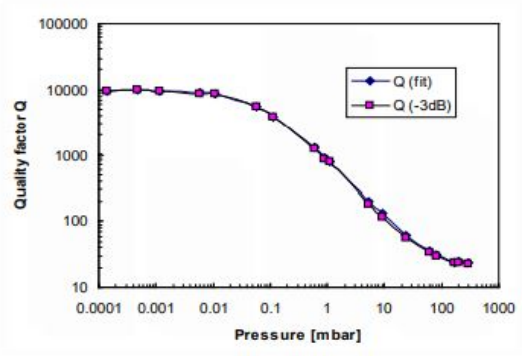

Figure 2.11: *Q factor values as a function of the pressure.*

possible application could be medical imagining because the ideal device has to oscillate as much as possible in order to send a higher acoustic intensity. Another consideration regarding the choice of the Q factor can be done taking into account the modulation of an ultrasound signal; indeed, a lower Q factor (wide bandwidth) can be exploited to carry out a frequency modulation of the signal in order to send a high amount of information [17]. The variation of the amplitude as a function of the Q factor can be observed in the Fig.2.12.

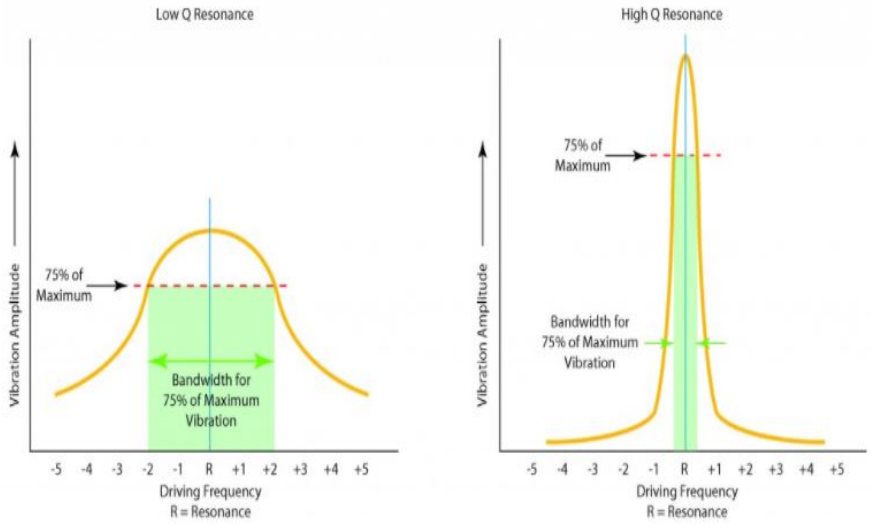

Figure 2.12: *Bandwidth amplitude depending on the values of Q factor.*

Another possibility for this device is the need to form an array. Generally, a transducer with a single element cannot fully satisfy many practical applications (i.e in medical imaging and NDT (non-destructive technique). Due to this limitation, the use of multiple transducer elements and dynamic control of each element is exploited to achieve electronic beam steering, focusing and scanning, which bring benefits in reduction of test time and better reliability and quality of measurements. The ultrasound beam is transmitted perpendicular to the element surface and if a phase delay is introduced into the signal applied to each element of the linear array, ultrasound

beam focusing and steering can be achieved by the constructive and destructive interference of acoustic waves coming from different membranes, as shown in Fig. 2.13.

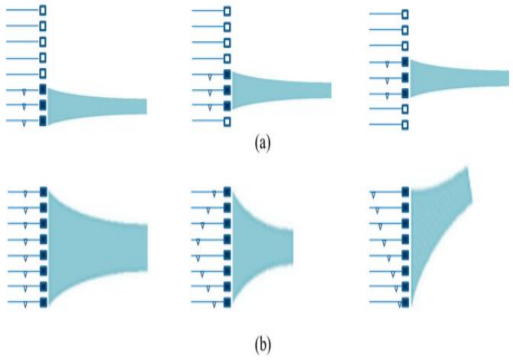

Figure 2.13: *Schematic diagrams of a) electronic scanning of 1-D linear arrays; b) electronic focusing and steering of 1-D phased linear arrays. [3]*

.

Chapter 3

Piezoelectricity

The third chapter is devoted to the piezoeletricity since the PMUTs working principle is based on this effect. It is organized in the following way: the initial section is focused on piezoelectric effects, the second one introduces the most important piezo materials and a detailed description of PZT is proposed, the third section describes the deposition methods such as sol-gel and sputtering techniques and finally a constitutive model to describe these materials and their coupled electro-mechanical behavior will be analyzed.

3.1 Piezoelectric effect

The ability of some materials to convert an electrical energy into a mechanical one and vice versa is called respectively converse and direct piezoelectric effect.

The first demonstration of the direct piezoelectric effect was in 1880 by the brothers Pierre Curie and Jacques Curie while they were studying the behavior of some materials such as crystals of tourmaline, quartz, topaz, cane sugar, and Rochelle salt: they applied some mechanical deformation while measuring the voltage difference at the boundaries of the deformed material. The Curies, however, did not predict the converse piezoelectric effect: it was firstly deduced by Lippmann one year after during his thermodynamic studies. Immediately the Curies brother confirmed the existence of the converse effect and they went on to obtain quantitative proof of the complete phenomena. For the next few decades, piezoelectricity remained under investigation and during these years more work was done to explore and define the crystal structures. This research activity culminated in 1910 with the publication of Woldemar Voigt's Lehrbuch der Kristallphysik, which for the first time described the 20 natural crystal classes capable of piezoelectricity, and rigorously defined the piezoelectric constants using tensor analysis [18][5][16]. Under an operational point of view, when a voltage difference (electric field) is applied to a piezoelectric material, inside the crystal lattice the formation and orientation of the electric dipoles occur resulting in a electric polarization and in turn in a deformation (change in volume). This effect is called converse piezoelectric effect and it is strictly related to the electric dipole formation and it can be used in actuators applications. Similarly, in the direct piezoelectric effect, a mechanical deformation causes the generation of the electric dipoles and in turn it will generate a voltage difference: this behaviour is exploited in sensor application and as the first one (converse) is related to the micro-structure of the material. In Fig. 3.1 a simplified scheme of the piezoelectric effect is proposed.

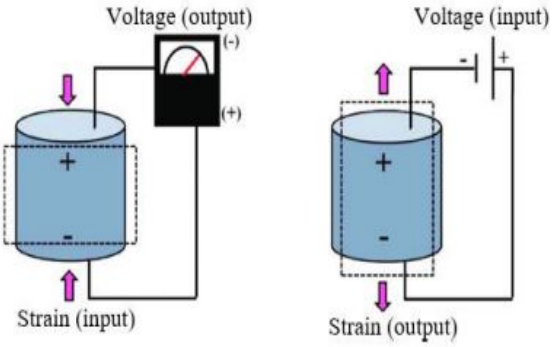

Figure 3.1: *Simplified example of the direct (left) and converse (right) piezoelectric effects.*

Since the electric dipoles are key aspects in order to understand the piezoelectric effect, a microscopic analysis of these material will be needed. All the crystalline materials are divide into 32 crystal lattices and among them only those classes without a centre of symmetry can experience the presence of an electric dipole. There are 21 out of the 32 lattice families who satisfy this requirement but out of these 21 classes, one displays no piezoelectric effect because the movement of the charges during mechanical solicitation does not induce the appearance of a dipole. Therefore only 20 classes are piezoelectric. During the application of a mechanical constraint, the crystal loses shape and the centers of gravity of positive charges separate from those of negative charges at the level of each crystal lattice: the result is the production of a electric dipole. Out of these 20 classes, 10 are pyroelectric, i.e. they have an electric polarization even in the absence of an applied electric field. The preferred direction of polarization is called the polar axis and these classes are called pyroelectric because of the variation in amplitude of the dipole moment when the temperature changes. The most famous pyroelectric materials are the AlN (Aluminium Nitride) and ZnO (Zinc Oxide) and both are characterized by a wurtzite structure. Among pyroelectric crystals, we can distinguish ferroelectric ones for which the polar axis (direction of polarization) is mobile in the crystal lattice under the influence of an external electrical field: it is possible to reverse the direction of polarization if the applied field is sufficiently strong. Materials having a perowskite structure belong to this family and an example is the PZT (Lead Zirconate Titanate) [18]. In Fig. 3.2 the classification of the 32 crystal classes according to these different denominations is summed up.

3.2 Piezoelectric material overview

As introduced before, the piezoelectric materials are divide into sub-sets depending on the crystal structure and in turn on the features of the polarization that it can be formed inside the material. Mainly, we can distinguish a wurtzite structure in case of pyroelectric material and a perowskite structure for the ferroelectric ones[18].

- **Wurtzite structure**: This structure corresponds to that of AlN and ZnO. It is characterised by an hexagonal lattice and it can be seen as a juxtaposition of two compact hexagonal structures for the two kind of ions composing the structure. The two structures are shifted following the c axis by a distance of $3/8c$. This is what explains the spontaneous

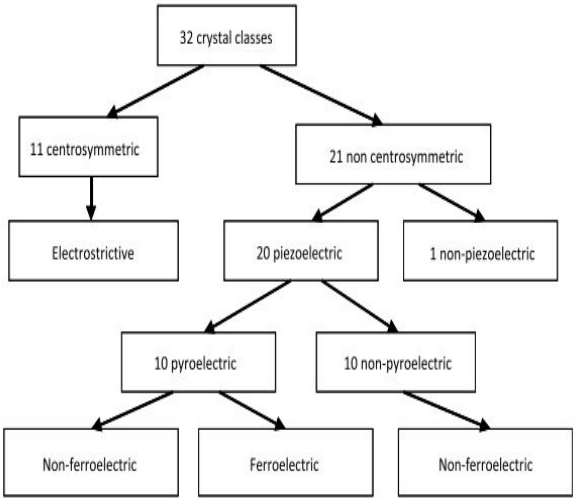

Figure 3.2: *Classification of crystal lattices according to their piezoelectric, pyroelectric, ferroelectric and electrostrictive properties [18]*

polarization for this structure, even in the absence of the electric field. Lattice parameters, by choosing a hexagonal lattice, are the following for AlN: a = 3.112 Å and c = 4.982 Å (Fig. 3.3a).

- **Perowskite structure**: Perovskite is the most well-known and studied ferroelectric structure. It is described from its simple cubic phase, which appears above its Curie temperature: it is important to remember that above this limit temperature the structure shows a center of symmetry and therefore it is not piezoeletric anymore but it allows for a simpler description. Perovskite structure has the form ABO_3 and in what follows, it will be taken $Pb(Zr, Ti)O_3$ (PZT) as example since it is the material used for PMUTs fabrication in STMicroelectronics. In Fig.3.3b it is possible to see the cubic perowskite lattice where A(Pb) is a cation with a large radius and coordinance equal to 12 and it is located on the vertices, B(Zn or Ti) is the small central cation with coordination number of 6 and lastly oxygen ions that occupies the centre of the six faces.

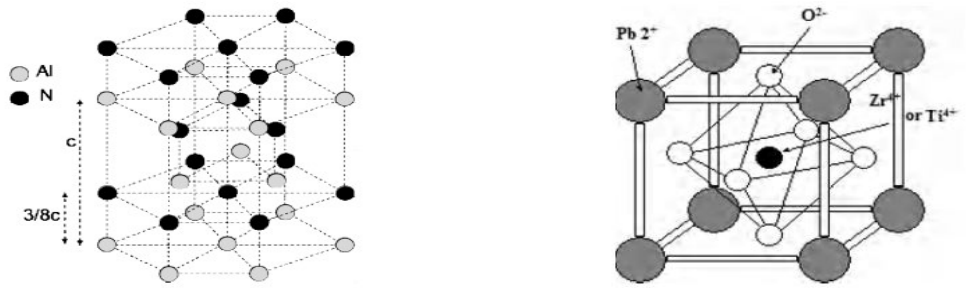

(a) ***(b)***

Figure 3.3: *a) Representation of the AlN wurtzite . b) Cubic Perovskite Lattice of PZT.*

The central positive ions are able to move within the crystal in case of an external stimulus. Therefore, when a voltage difference is applied to the material, the central cation moves along the direction of the electric field causing an expansion and at the same time a contraction in the perpendicular direction. The chemical formula of PZT is $Pb(Zr_xTi_{(1-x)})O_3$, where the number x is equal to the ratio $[Zr]/([Zr]+[Ti])$. Basically, the perovskite lattice of PZT can be of three different forms depending on the temperature and the Zr/Ti relation:

1) cubic structure when the temperature is above the Curie temperature (T_{curie}), which corresponds to the paraelectric phase that does not show an electric dipole;

2) tetragonal lattice when the temperature is below T_{curie} and $x < 0.45$ (titanium dominance). This phase shows a permanent dipole moment throughout the cubic lattice strain;

3) rhombohedral structure when the temperature is below T_{curie} and $x > 0.5$ (zirconium dominance). This phase also shows a permanent dipole moment.

It is worth to say that when x is included between approximately 0.45 and 0.5, the phase obtained is defined as morphotropic. At the beginning, it was believed that this phase was simply a mixture of the tetragonal and rhombohedral phases but then it was showed the presence of a mono-clinic structure in this area of the phase diagram (Fig. 3.4). Thanks to the presence of the monoclinic phase the PZT shows its higher values of electromechanical properties[19].

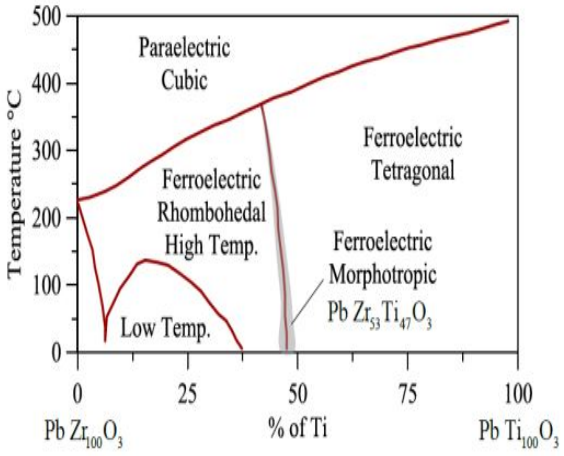

Figure 3.4: *Phase diagram of PZT.*

As we have seen, the notion of ferroelectricity is based on the fact that spontaneous polarization of the material can vary its orientation if an external electric field is applied. The direction of the pole axis can also be reversed if this field is sufficiently intense. In Fig.5.2a the state of macroscopic polarization of a ferroelectric material based on the electric field of excitation is shown and it easy to observe a hysteresis loop.

Looking at the Fig. 5.2b, a more detailed description can be done: at the beginning the application of an electric field results in linear response (polarization) of the material,

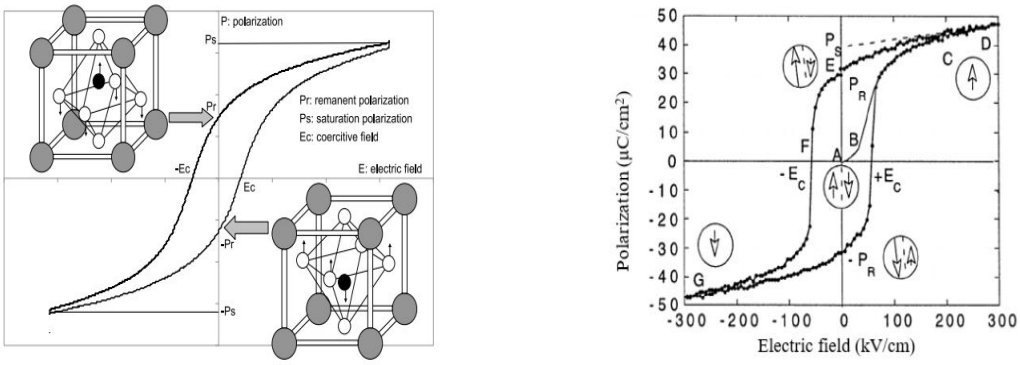

(a) *(b)*

Figure 3.5: *a) Polarization curve as a fuction of the applied electric field. Moreover, the crystal lattice in the two cases of residual polarization are shown. b) Another example of polarization curves where each characteristic segment is named with a letter [20]*

.

which is represented by the segment AB. As the applied electric field increases its intensity, the number of ferroelectric domains aligned in its direction increases and as a result the obtained polarization increases: in the segment BC the response of the material becomes strongly nonlinear. At point C, all the domains are aligned in the direction of the applied electric field and the response of the material goes back to being linear (segment CD). The intercept between the extrapolation of this segment and the polarization axis gives the saturated polarization P_s. Another two important ferroelectric properties that can be extracted from this hysteresis loop are the remnant polarization P_r and the coercive field E_c. The former parameter is located at the intercepts between the hysteresis curve and the axis y and represents the residual polarization observed with an electric field null; the latter indicates the electric field needed to undo the polarization and it can be observed at the intercepts between the curve and the axis x.

After this description of the two main families of piezoelectric material, it is useful to give some information related to their performance, pointing out their advantages and disadvantages. As a general rule, the AlN (wurtzite) has better performance in sensing with a sensitivity higher than the PZT one; on the other hand PZT is chosen for transmission applications thanks to its much higher values of displacement induced by a voltage application (higher eletromechanical coefficients). Unfortunately, the PZT shows two drawbacks on which research activity must be carry out: degradation and aging over the time and the presence of the lead in its chemical composition. In order to give an idea of the order of magnitude of the sensitivity in transmission mode, the Fig.3.6 shows the frequency response of three different PMUT membrane: PZT with a diameter of 50 um, PZT with a lower diameter (40 um) and AlN with a diameter equal to 50 um. As expected, in case of identical material membrane the lower is the diameter the higher is the frequency of oscillation; in addition, it is easy to observe as the amplitude of displacement of the AlN membrane is much lower than that of PZT and its frequency is much higher with equal diameter[21].

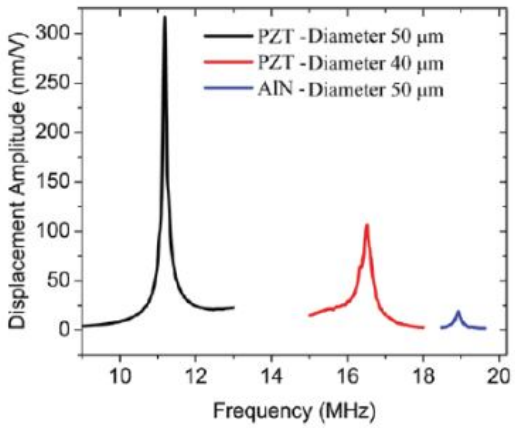

Figure 3.6: *Frequency response of three different membrane*

3.3 Deposition techniques of the piezoelectric layer

One of the major challenge in the fabrication process of Piezo MEMS concerns the deposition of the piezoelectric layer without compromising its properties. Nowadays, various methods are adopted to achieve this goal and among them there are physical technique such as ion beam sputtering, RF magnetron sputtering, pulsed laser deposition and chemical methods such as sol-gel deposition and metal-organic chemical vapor deposition. The thickness of the piezo layer is usually a few um (e.g., our device has a thickness equal to 1um) and the best methods used to deposit it are sol-gel and sputtering.

3.3.1 Sol-gel deposition method

Sol-gel technique is the most widely used and cheapest method for fabrication of thin film PZT layers mainly because this method offers four advantages [22][23]:

- **1)** the stoichiometric chemical composition of PZT thin films can be easily controlled. Since the physical properties strongly depend on the control of the chemical composition, this technique allows the deposition of several PZT ceramic layer with controllable performances.
- **2)** sol-gel processes do not produce by-product due to its complete usage of precursors (cost effectiveness). Moreover, using sol-gel method allows to directly pattern the micro structures without using conventional etching: it needs the control of the coverage step of the surface.
- **3)** the technique can be used to deposit PZT layer with different thickness and moreover the sol-gel process is compatible with microfabrication processes.
- **4)** thanks to sol-gel method it is possible to obtain a dense micro-structure and a good coverage on large-size substrates.

After the introduction of the advantageous of this deposition method the main steps of the process are resumed in Fig. 3.7 [23]:

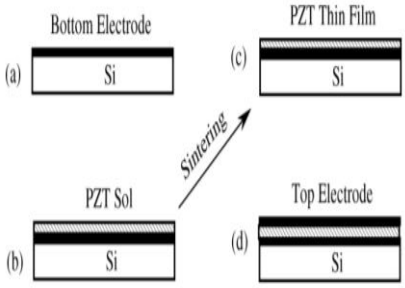

Figure 3.7: *Work flow of the sol-gel deposition method: a) deposition of the bottom electrode on the silicon substrate; b) Spin coating of the PZT solution on the bottom electrode; c) Sintering at elevated temperature (*600/700 *°C) of the stack Substrate/bottom/PZT solution; d) deposition of the top electrode*

Regarding the previous figure, it is important to add some considerations in relation to the spin coating and sintering steps (b and c). The former step is crucial to homogenize the PZT solution over the surface and guarantee a constant thickness, while the latter is carried out more than once (the repetition number depends on the desired thickness) at elevated temperature and it is aimed at increasing the density (reduction of the porosity) and to form the desired perovskite crystalline structure. The sintering step can also be divided into sub-steps where there is an initial drying step at lower temperature (130°C) followed by a calcination step at 350°C and lastly the actual cristallization at elevated temperature (600/700°C) [24].

Despite this technique of deposition shows many advantages, there are also disadvantages to be taking into account and on which some research activity has to be done. The main one is the formation of cracks and defects in the PZT layer and these imperfections can behave as a channel able to short circuit the top and bottom electrode and moreover they can speed up the process of aging and degradation. Another problem is related to the delamination at the interface between bottom electrode and PZT layer that can occurs during the heating steps of the sintering process and the following cooling one as a consequence of the mismacth between thermal expansion coefficient. Always during the sintering phase, another problem can be detect and it concerns the bottom electrode. Presently, the materials used as a electrode are metals (Pt/Ti) and at $T_{sintering} = 600 - 700$°C they become thermally unstable. This instability results in porosity inside the electrodes and in turn the presence of holes degrades the functions of electrodes because oxygen coming from the PZT films diffuses into the electrode domain resulting in dielectric loss.

As just analyzed, all the major problems are strictly related to the high temperature reached during the sintering process. Unfortunately, a higher sintering temperature will significantly improve the piezoelectric properties of the film. Indeed, a higher $T_{sintering}$ allows to obtain higher grain size in the PZT and in turn the piezoelectric behavior increases as the grain size becomes bigger. It will be key to find a balance between this opposite effects and the ideal result would be to work with high temperature and to find some alternative material for the bottom electrode and a way to avoid the formation of defects inside the piezoelectric domain [23].

3.3.2 Sputtering

Another common technique used for ferroelectric thin film deposition is the sputtering. The sputtered PZT layer has almost the same properties as the one obtained through sol-gel but it shows two main differences: a higher directionality of the polarization and a more stable piezoeletric properties along time [25]. Basically this process consists of bombarding the PZT ceramic target with energetic inert gas ions, such as argon at a pressure of 0.1-10 Pa; once the atomic species of the target are removed from it they are deposited onto the surface of the substrate. It is easy to understand how the composition of the deposit layer will be equal to that of the target and the possibility of having particles contamination depends on the vacuum level of the chamber where the gas ions are contained. The target is obtained by mixing ZrO_2, TiO_2 and PbO powders with an excess of the last one to compesate its loss during the post-growth annealing and at the end the composition has to be $Pb(Zr_{0.52}, Ti_{0.48})O_3$ in order to maximize the piezoelectric parameters [23] (phase diagram Fig. 3.4).

Although there are several advantages of the sputtering deposition of PZT thin films, as mentioned above, one of its drawbacks is the difficulty in optimizing the sputtering conditions among a variety of sputtering parameters (composition of the ions gas, vacuum level, preparation of the substrate to improve the adhesion of the sputtered layer and temperature of the substrate). One of the effective methods of stabilizing the growth conditions of PZT thin films is the insertion of seed layers at the interface of the substrates: indeed, when the PZT layer is deposit on a Pt-coated substrate (Pt is a common material used as a bottom electrode), the Zr in PZT prevents the growth of the perovskite phase owing to the formation of Zr oxide at the surface. Due to this problem, the use of seed layers on the substrate, such as $PbTiO_3$ or $SrRuO_3$, is effective for preparing a perovskite layer on substrates without the formation of a non-perovskite phase. Another important consideration has to be done in relation to the orientation of the PZT layer: it will follow the crystalline orientation of the seed layer and that in turn depends on that of the silicon substrate. Regarding the best orientation to optimize the piezoeletric effect of the PZT layer it is not clear yet and more studies are required[25].

An example of RF magnetron sputtering is shown in the Fig. 6.24b, where the motion of the atomic species removed from the target toward the Pt-coated substrate is guaranteed by the application of RF voltage.

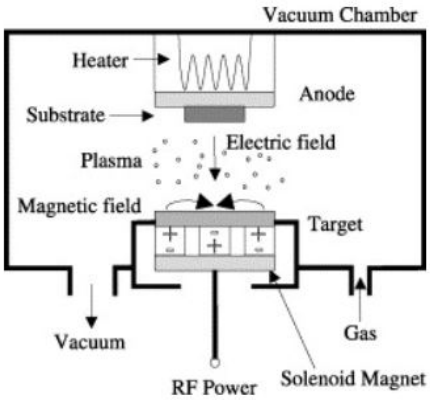

Figure 3.8: *Scheme of the RF magnetron sputtering process [26].*

3.4 Piezoelectric constitutive model

After the introduction of the main piezoeletric materials and the deposition methods adopted, the discussion moves on the modified constitutive equations characterizing their behavior. As seen previously, the piezoelectricy effect (both direct and converse) couples the elastic mechanical response of the material to the electric behavior: indeed, in a piezo material the electric and mechanical domain coincide and they are completely overlapped.

Starting from the mechanical response, the dynamic equilibrium and kinematic compatibility in the volume and over the surface govern the mechanical response. Considering a solid with volume Ω and external surface Γ subjected to volume and surface forces, F_i and f_i, under the hypothesis of small deformations and displacements, the behavior will be determined by the following equations [27]:

$$\begin{cases} T_{ij,j} + F_i = \rho_m \ddot{s}_i \text{ in } \Omega \\ T_{ij} n_j = f_i \text{ over } \Gamma \end{cases} \tag{3.1}$$

$$\begin{cases} S_{ij} = \frac{1}{2}(s_{i,j} + s_{j,i}) \text{ in } \Omega \\ s_i = \tilde{s}_i \text{ over } \Gamma \end{cases} \tag{3.2}$$

Where the system of the Eq.3.1 represents the dynamic equilibrium and the terms involved are respectively $T_{ij,j}$ stress tensor, ρ_m mass density, $\ddot{s}_i$ acceleration vector components and s_i displacements vector components; and the static boundary conditions that bind the surface forces to the the product between the stress vector and the normal unit vector $T_{ij}n_j$. The system of Eq. 3.2 shows the compatibility equation between the strain tensor S_{ij} and the symmetric part of the displacement gradient and moreover on that domain it must be valid the equality of the displacements vector imposed and experienced.

Similarly, even the only electric problem is governed by the electrostatic equilibrium and compatibility equations in the volume Ω and over the surface Γ. The equations used for the electric problem are the following ones:

$$\begin{cases} D_{i,j} - \rho_c = 0 \text{ in } \Omega \\ D_i n_i = -q_c \text{ over } \Gamma \end{cases} \tag{3.3}$$

$$\begin{cases} E_i = -\Phi_i \text{ in } \Omega \\ \Phi = \tilde{\Phi} \text{ over } \Gamma \end{cases} \tag{3.4}$$

The first system of Eq.3.3 can be considered as the electric analogous of the dynamic equilibrium and it states the equality between the variation of the electric displacement vector components and the electric charge density. As before, even the boundary conditions have to be guaranteed.

Instead, the system Eq.3.4 is the correspondent of mechanical compatibility, where in the upper equation the electric field is equal to the gradient of the scalar electric potential and in the bottom equation the potential is imposed equal to the applied voltage.

Once the dynamic and compatibility equation are defined, both for the elastic mechanical problem (Hooke's law) and the electrostatic one the constitutive equations can be introduced[5]:

$$S = cT, \tag{3.5}$$

$$D = \epsilon E, \tag{3.6}$$

where the terms in Eq. 3.5 and 3.6 are respectively: S strain vector, c compliance tensor, T stress vector, D electric displacement vector, ϵ electrical permettivity (matrix) and E electric field (vector).

Since in the piezoelectric materials the elastic and electric behavior are coupled, stresses depend not only on strains but also on the electric field, and in addition the electric displacement depends not only on the electric field but also on strains. By combining the two previous equation into the so-called coupled equations, the piezoelectric constitutive laws are obtained:

$$T = c^E S + e^T E, \tag{3.7}$$

$$D = eS + \epsilon^S E, \tag{3.8}$$

The Eq. 3.9 and 3.10 represent the so-called e-form of the piezoelectric constitutive relations, in which the strain and the electric field are used as coupling variables and where the electro-mechanical coupling matrix e appears. In this form of the coupled equation the term e is defined with units of newtons per volt metre [N/Vm], the superscript E to c denotes that the compliance tensor must be evaluated at constant electric field, the superscript S to ϵ indicated that the permittivity must be computed at constant strain and the superscript T to e simply represent the transposed matrix of the coupling coefficient.

Another notation used to define the piezoelectric constitutive law is the so-called d-form, in which stresses instead of strains are used as coupling variables; in this case, the matrix of coupling coefficients e is replaced with the matrix d having units of metres per volt [m/V]:

$$S = a^E T + d^T E, \tag{3.9}$$

$$D = dT + \epsilon^T E, \tag{3.10}$$

where the term a is defined as the ratio between d (piezoelectric charge matrix) and e, $a = \frac{d}{e}$, and the superscript T to the d denotes that the term is evaluated at constant stresses (the superscript T to d simply stands for the transposition of the matrix).

As demonstrated, the piezoelectric constitutive laws are the combination of the Hooke's law and the electric constitutive law where the coupling terms are represented by e and d. Considering a ceramic material such as the PZT the Eq. 3.9 and 3.10 in the complete matrix notation assume the following form (some terms in the coupling matrix are zero)[16]:

$$\begin{bmatrix} S_1 \\ S_2 \\ S_3 \\ S_4 \\ S_5 \\ S_6 \end{bmatrix} = \begin{bmatrix} s_{11}^E & s_{12}^E & s_{13}^E & 0 & 0 & 0 \\ s_{21}^E & s_{22}^E & s_{23}^E & 0 & 0 & 0 \\ s_{31}^E & s_{32}^E & s_{33}^E & 0 & 0 & 0 \\ 0 & 0 & 0 & s_{44}^E & 0 & 0 \\ 0 & 0 & 0 & 0 & s_{55}^E & 0 \\ 0 & 0 & 0 & 0 & 0 & s_{66}^E \end{bmatrix} \begin{bmatrix} T_1 \\ T_2 \\ T_3 \\ T_4 \\ T_5 \\ T_6 \end{bmatrix} + \begin{bmatrix} 0 & 0 & d_{31} \\ 0 & 0 & d_{32} \\ 0 & 0 & d_{33} \\ 0 & d_{24} & 0 \\ d_{15} & 0 & 0 \\ 0 & 0 & 0 \end{bmatrix} \begin{bmatrix} E_1 \\ E_2 \\ E_3 \end{bmatrix} \tag{3.11}$$

$$\begin{bmatrix} D_1 \\ D_2 \\ D_3 \end{bmatrix} = \begin{bmatrix} 0 & 0 & 0 & 0 & d_{15} & 0 \\ 0 & 0 & 0 & d_{24} & 0 & 0 \\ d_{31} & d_{32} & d_{33} & 0 & 0 & 0 \end{bmatrix} \begin{bmatrix} T_1 \\ T_2 \\ T_3 \\ T_4 \\ T_5 \\ T_6 \end{bmatrix} + \begin{bmatrix} \epsilon_{11} & 0 & 0 \\ 0 & \epsilon_{22} & 0 \\ 0 & 0 & \epsilon_{33} \end{bmatrix} \begin{bmatrix} E_1 \\ E_2 \\ E_3 \end{bmatrix} \tag{3.12}$$

where the first equation represents the relationship for the converse piezoelectric effect and the latter for the direct effect.

Generally, as a standard assumption, the direction 3 is considered as the polarization direction and therefore it is possible to distinguish three different behavior as resumed in Fig 3.9:

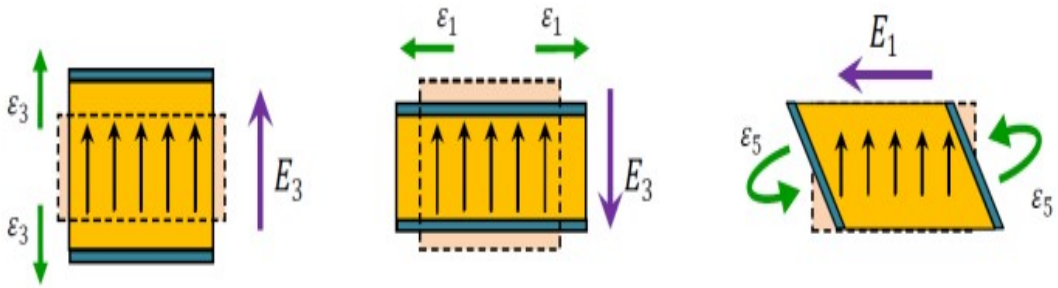

Figure 3.9: *Examples of piezoelectric behavior with a polarization in direction 3 [28]: from left to right there are the '33' effect, '31' and '15'.*

Analyzing in more detail the three modes of the previous figure, they can be described as follows[5]:

- **33 mode**: by applying a electric field in the same direction of the polarization, the piezoelectric material can shrinks or stretches in the same direction.
- **31 mode**: when applying a electric field along the polarization direction, the piezoelectric material can shrinks or stretches along the orthogonal direction.
- **15 mode or shear mode**: the piezoeletric material can suffer shear when a electric field is applied perpendicularly to the polarization direction.

In relation to the PMUT device studied during the thesis, the electric field was applied in direction 3 through the application of a voltage difference between top and bottom electrodes and the mode 31 was exploited in order to put in oscillation the membrane. For the sake of clarity, it must be pointed out that the sandwich stack (bottom-PZT-top) is the easiest one to obtain under a process point of view and for that the applied electric field will almost always be along direction 3.

As a last information of this chapter, it is useful to give some values of the coupling coefficients of the main piezoelectric materials. In the following Table 3.1 the coefficents in e-form are provided when a electric field is applied along polarization direction:

Material	$e_{33}[\frac{N}{mV}]$	$e_{31}[\frac{N}{mV}]$
Lead Zirconate Titanate	18/25	-8/-18
Aluminium Nitride	1.8/2.4	-0.8/-2
Zinc Oxide	1.2/1.5	-0.6/-1

Table 3.1: *Coupling coefficient values for the most common piezoeletric materials.*

Chapter 4

Acoustics

In this chapter the basic notions of the acoustic phenomena are presented. Starting from a brief introduction, the discussion will move toward the linear mathematical model used to describe their propagation in a medium because these equations will be involved in the Comsol model. Finally, in the last subsection of the chapter, the sound pressure level (SPL) and the intensity level (IL) will be described since they are the main parameters to quantify an acoustic field.

4.1 Introduction

Acoustic waves constitute one kind of pressure fluctuation that can exist in a compressible fluid. They can be related to mechanical vibrations or oscillations of a solid in contact with a fluid domain as shown in the Fig.4.1.

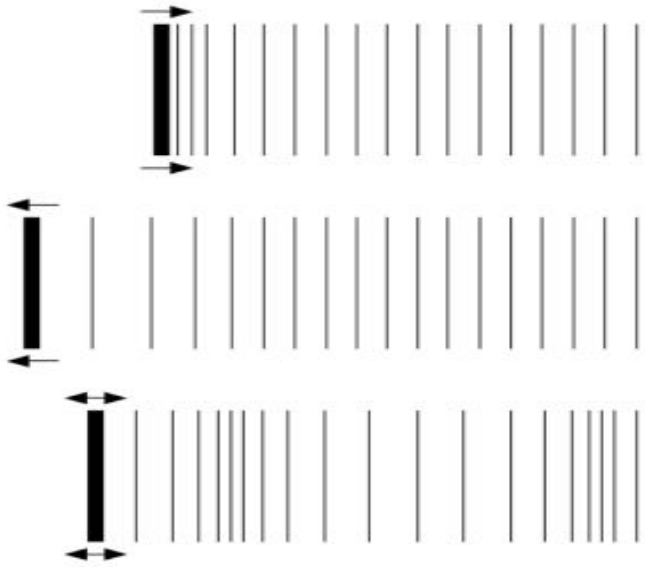

Figure 4.1: *Propagation of acoustic wave as a consequence of solid vibration. The vibration of the solid can be considered as piston-like movement.[29]*

As can be observed in the previous figure, the oscillation of the solid causes a variation in the density of the fluid: alternatively compression and rarefaction. At the beginning, the changes of density regard the portion of fluid close to the object only, but if the solid continues to oscillate the density variation will propagate along the space. This variation of density inside the compressible fluid can then be associated to a variation of pressure by means the state equation of the fluid. Therefore, starting from a solid vibration the so called pressure wave/acoustic wave is generated. Already at this point of the discussion, a key aspect related to the acoustic appears evident: in order to have an acoustic wave a necessary condition is the presence of a fluid through which travelling. In vacuum it is impossible to have the generation and propagation of acoustic waves and this evidence will be exploited in the cross-talk analysis of the following chapter.

The acoustic audible waves we are used to listen in our daily life are a low intensity pressure field with a frequency included in the range (20,20000) Hz. Additionally to these kind of acoustic waves, there are also ultrasonic and infrasonic waves whose frequencies lie beyond the limit of hearing (respectively over the 20 kHz and below the 20 Hz): the PMUTs object of this master thesis are able to send and receive ultrasound waves with a frequency value equal to 130 kHz. Moreover, the velocity of propagation of the acoustic wave results finite due to the necessity of time to transfers the density variation in the fluid: its values is equal to the sound velocity 343 m/s. As for other kinds of waves, even the acoustic perturbation is subjected to phenomena such as transmission, reflection, absorption, dispersion and diffraction.

In the following subsection, the mathematical formulation of the acoustic problem for the pressure field is proposed together with the multi-physic acoustic-structure interaction conditions used in the PMUT numerical modelling.

4.2 Linear Acoustic Mathematical Model

Here we are interested in the simplest acoustics situation: linear acoustics (which describes low energy phenomena only) of a perfect no-dissipative simple fluid in an initial stationary homogeneous equilibrium, i.e. subjected to zero body forces and heat sources. Taking into account a no-dissipative fluid domain Ω moving with velocity $\boldsymbol{\nu}$ and with volumetric density equal to ρ, the following conservation laws of mass,linear momentum and energy hold within the volume (Eq.4.1, 5.1, 4.3) [30][31]:

$$\frac{\partial \rho}{\partial t} + \nabla(\rho \boldsymbol{\nu}) = 0 \tag{4.1}$$

$$\rho \left(\frac{\partial \boldsymbol{\nu}}{\partial t} + \boldsymbol{\nu} \cdot \nabla(\boldsymbol{\nu}) \right) + \nabla p = 0 \tag{4.2}$$

$$T\rho \left(\frac{\partial s}{\partial t} + \boldsymbol{\nu} \cdot \nabla(s) \right) = 0 \tag{4.3}$$

where t is the time, p is acoustic pressure, T the temperature and s the specific entropy of the system.

In case of homogeneous reference configuration at the steady state, the following equalities hold:

$$\rho^0 = const; \boldsymbol{\nu^0} = \mathbf{0}; p^0 = const; T^0 = 0; s^0 = const \tag{4.4}$$

Let the first order variations of the reference configuration of the acoustic quantities be:

$$\rho^1; \boldsymbol{\nu}^{\mathbf{1}}; p^1; T^1; s^1 \tag{4.5}$$

Such that the acoustic parameters can be evaluated in the following way:

$$\rho = \rho + \rho^1; \boldsymbol{\nu} = \boldsymbol{\nu}^{\mathbf{0}} + \boldsymbol{\nu}^{\mathbf{1}}; p = p^0 + p^1; T = T^0 + T^1; s = s^0 + s^1 \tag{4.6}$$

where the higher order terms are omitted for the sake of semplicity.

By developing Eq.4.1, 5.1 and 4.3 and stopping the expansion to the first order, the linear acoustics conservation equations in the volume Ω are derived as follow:

$$\frac{\partial \rho^1}{\partial t} + \rho^0 \nabla \boldsymbol{\nu}^1 = 0 \tag{4.7}$$

$$\rho^0 \frac{\partial \boldsymbol{\nu}^1}{\partial t} + \nabla p^1 = 0 \tag{4.8}$$

$$T^0 \rho^0 \frac{\partial s^1}{\partial t} = 0 \tag{4.9}$$

In the Eq.4.9, the isoentropic fundamental property of an acoustic perturbation in a simple non-dissipative fluid appears and it means that $s^1 = const\ \forall t$.

Moreover, the thermodynamic state equations are reported:

$$\rho^1 = \chi_s^0 \rho^0 p^1 \tag{4.10}$$

$$T^1 = \frac{\alpha_p^0 T^0}{C_p^0 \rho^0} p^1 \tag{4.11}$$

where C_p^0 is the specific heat, α_p^0 is the thermal expansion coefficient at constant pressure and $\chi_s^0 = \frac{1}{\kappa_s^0}$ is the compressible modulus (the inverse of the bulk modulus at constant specific entropy) computed at the reference state. Hereinafter, for sake of brevity, in the wave equations for the acoustic quantities the superscript 1 indicating the first variation, is omitted everywhere. Looking at the Eq.4.10 and 4.11, it is easy to understand how the density and temperature variations are linearly proportional to the pressure variation which represents the main source of the acoustic perturbation. At this point, starting from the equations 4.7 and 4.8 the wave equation for the acoustic pressure is obtained. By applying the following mathematical operation $-\frac{\partial}{\partial t}$ Eq.4.7 + $\nabla\cdot$ Eq.4.8 we derive the following formula:

$$-\frac{1}{c^2}\frac{\partial^2 p}{\partial t^2} + \nabla^2 p = 0 \tag{4.12}$$

where the parameter c represents the sound velocity and the following relation holds:

$$c = \sqrt{\frac{\kappa_s^0}{\rho^0}} \tag{4.13}$$

Additionally, after further mathematical steps that will be omitted for the sake of simplicity, also the wave equation for the acoustic velocity perturbation is derived for the volume Ω:

$$-\frac{1}{c^2}\frac{\partial^2 \boldsymbol{\nu}}{\partial t^2} + \nabla^2 \boldsymbol{\nu} = 0 \tag{4.14}$$

Lastly, also the wave propagation equations as a function of the variation of density ρ and temperature T can be computed by manipulating thermodynamic equations (Eq. 4.10 and 4.11):

$$-\frac{1}{c^2}\frac{\partial^2 T}{\partial t^2}+\nabla^2 T=0 \tag{4.15}$$

$$-\frac{1}{c^2}\frac{\partial^2 \rho}{\partial t^2}+\nabla^2 \rho=0 \tag{4.16}$$

After the discussion and the introduction of the main equations governing the acoustic propagation in a ideal fluid, the attention moves toward the study of the Acoustic-Structure Interaction (ASI) at the boundary. The coupling between the two mediums is guaranteed by continuity of the normal stress and acceleration on the interaction surface S_p, having the outward normal vector $\boldsymbol{n}$ toward the fluid domain. Therefore, the described condition is obtained by means of the following Eq.4.17 and 4.18 onto the surface S_p:

$$\nabla p \cdot \boldsymbol{n} = -\rho^0 \ddot{\boldsymbol{u}} \cdot \boldsymbol{n} \tag{4.17}$$

$$-\boldsymbol{T}\boldsymbol{n} = p\boldsymbol{n} \tag{4.18}$$

where $\boldsymbol{T}$ and $\boldsymbol{u}$ are respectively the stress tensor and the displacement of the moving interacting structure.

Moreover, in this last part the boundaries condition of the fluid domain will be described. Mainly, the two situations implemented in the Comsol model are the rigid acoustic boundary (HW: hard wall) and the perfectly match layer (PML). The former behaves like a hard wall condition while the latter absorbs the acoustic perturbation avoiding any possible reflection phenomena. The relation governing the hard wall condition is quite straighforward to obtain it is shown in the Eq.4.20:

$$\nabla p \cdot \boldsymbol{n} = 0 \tag{4.19}$$

On the other hand, the acoustic propagation into an infinite fluid medium is simulated enforcing the first order absorbing boundary condition (PML) onto the surface S_{PML}:

$$\nabla p \cdot \boldsymbol{n} = -\frac{1}{c}\frac{\partial p}{\partial t} \cdot \boldsymbol{n} \tag{4.20}$$

As will be showed in the next chapter, this condition applied into the model guarantees no reflected wave arises and the incident waves are absorbed. All the main equations introduced in this section will be exploited in the COMSOL numerical models.

4.3 Sound Pressure Level and Intensity Level

In the acoustic application, it is customary to describe the acoustic pressure and the intensity of the perturbation using logarithmic scales, the so called sound levels. One of the main reason for this choice is the very wide range of sound pressure and intensity in the acoustic environment. For example audible intensity range from approximately 10^{-12} to 10 $\frac{\mathrm{W}}{\mathrm{m}^2}$ and the logarithmic scale allows to compresses this wide interval of values [31][30].

The most generally used logarithmic scale for describing sound levels is the decibel (dB) scale. By using this scale the Intensity Level (IL) can be defined, i.e. the IL of a sound wave of intensity I is given by the following Eq.4.21:

$$IL = 10 \log \left(\frac{I}{I_{ref}} \right) \tag{4.21}$$

where I_{ref} represents the reference intensity and in case of air its value is equal to $10^{-12} \frac{\mathrm{W}}{\mathrm{m}^2}$. At this point, starting from the previous Eq.4.21 and relation between the sound pressure and intensity $I = P^2/\rho_0 c$, the equation of the sound pressure level (SPL) can be defined:

$$SPL = 20 \log \left(\frac{P}{P_{ref}} \right) \tag{4.22}$$

where P_{ref} is the reference pressure and for waves travelling in air its value is 20.4 μPa. This values of acoustic pressure coincides with the minimum audible limit for human beings. In case of spherical and plane waves the values of SPL and IL match over long distances but nevertheless in some cases this coincidence disappears and consequently only the value of IL is taken into account as reference value.

Chapter 5

Experimental characterization and Modelling

The fifth and the sixth chapters of this master thesis are focused on the experimental and modelling activities. In the former chapter the PMUT device studied, the experimental campaign performed and the modelling simulations are introduced. The several investigations carried out will be analyzed by describing the experimental set-up and numerical models. The sixth chapter will show the results obtained and a critical analysis of these will be provided. I tried to point out the analysis where a match between simulated and experimental results is obtained and those in which a mismatch is observed. For the latter case, some hypothesis are proposed in order to interpret the differences and have a better comprehension.

The initial part of this chapter is devoted to the description of PMUT device and the experimental equipment I used in the STMicroelectronics' laboratory. Even if I have had the possibility to get in touch and familiarize with the use of many electronic devices such as oscilloscopes, multimeter, amplifiers and wave form generators, the attention is mainly focused on the Polytec MSA500 and on its different modes of operation. Similarly, the discussion continues with the introduction of the finite element (FE) software COMSOL Multi-physics 5.6 used to perform the numerical simulations. Its main characteristics and advantages in relation to other FE software will be explained together with the several possible studies it is able to perform.

After the experimental equipment and simulation software's introduction, the focus is given to the actual investigations I made. Starting from the mechanical characterization, the experimental mode and set up conditions to analyse the static deformation of the membrane and the whole die are proposed. Alongside, the models built to simulate the static deformed shape will be presented: in particular the 2D axi-symmetric model of a single membrane, the 3D model of a single membrane and the 3D model of a single membrane and of the whole device will be shown. After the analysis of the static configuration obtained due to the presence of the residual stresses, the second investigation performed concerns the resonance frequencies of the device. Both the experimental characterization mode and the simulation models to study this key parameter will be presented. As last mechanical study, the ring down oscillation is analyzed in terms of amplitude of displacement and Q factor. This investigation is performed numerically and experimentally both in air and in vacuum: a description of the simulation studies and of the experimental set-up is proposed. After this studies, the discussion moves toward the evaluation

and quantification of the cross-talk phenomena. Indeed, the membranes within the same die can interact each other and this can affect their behavior. Also this phenomena is studied both in vacuum and air to split the acoustic contribution from the mechanical one. It is worth to say that this topic has been studied only under an experimental point of view.

Once the cross-talk evaluation is completed, the next step is the acoustic characterization. In this subsection the experimental equipment will be introduced in parallel to the models built to evaluate the emitted acoustic waves.

As introduced previously, all the results will appear in the following chapter.

5.1 PMUT description

After the introduction of the working principle and all the equations governing their behaviour, the description of the PMUT device characterized during the thesis activity is proposed. For the sake of clarity, some pictures and simulation images will be used to give an idea of the geometry and dimensions involved.

The whole die is a parallelepiped with dimensions 6950 µm x 6950 µm and thickness equal to 400 µm and it contains sixteen membranes with diameter of the cavity equal to 860 µm. This last geometric parameter is key in order to compute the resonance frequency as seen in section 2.2.1 and the design reference value for our device is 140 kHz. Due to the uncertainty of the fabrication process, the value of the diameter can change of +/- 10 µm and so in turn the frequency of oscillation has a variable value around the reference one. The die can be observed in Fig. 5.1.

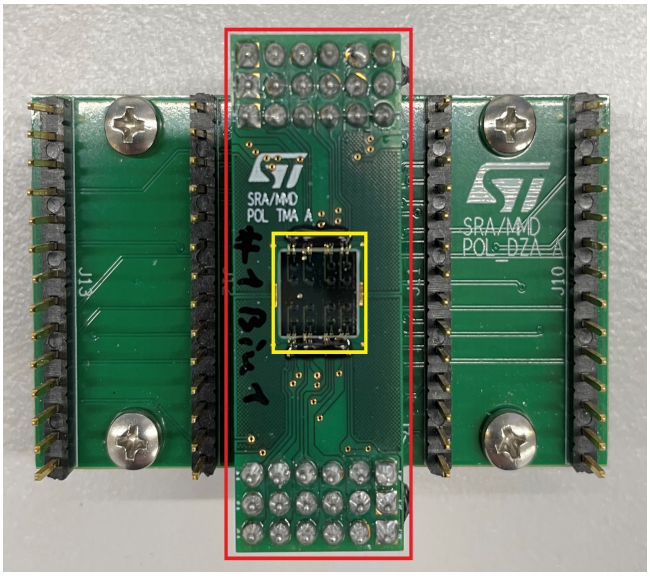

Figure 5.1: *Picture of the device connected to the printed circuit board (PCB). In the yellow square is pointed out the actual device with the 16 membranes while the red square highlights the TMA board which is connected to the expansion board.*

The TMA and expansion boards are used to make easier the characterization of the device. The expansion board contains 16 couples of pins to apply respectively an electric voltage to every

top electrode and ground to the bottom ones for each membrane. An important detail to stress is how the PMUT device is connected to the TMA board. The board has a square hole on which the whole die is attached by applying an epoxy glue to the four edges and below the board the cavity remains open. In Fig.5.16 can be seen the configuration previously described.

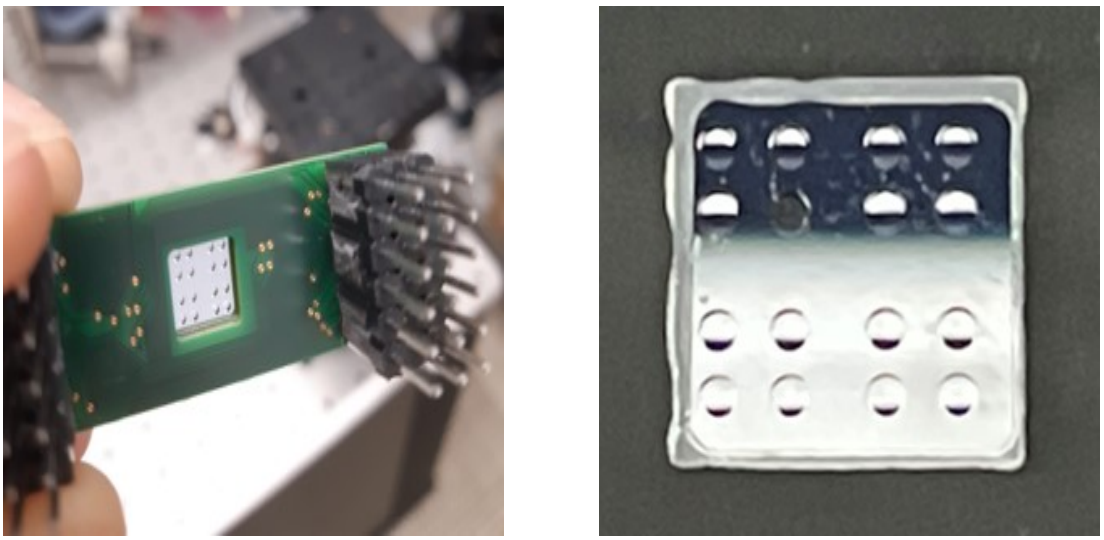

(a) *(b)*

Figure 5.2: *a) Picture from behind of the PMUT device attached to the TMA board. It can be easily observed that the cavity is open. b) Image of the PMUT device with the epoxy glue on the four edges. It looks like that on the left and top edge a higher amount of glue is used but only because the glue is remained on the TMA board for the other two edges.*

This way adopted to connect the device to the TMA board causes the deformation of the whole device itself. Indeed, the Silicon of the PMUT substrate, the epoxy glue and the material constituting the board have three different values of thermal expansion coefficients and so during the vulcanization of the glue they will experience different expansion. The mismatch in the expansion (during heating steps) and shrinkage (during cooling phases) will create residual stresses within the material domains and in turn they will strain to accommodate this differences (similarly to what happens in the stack membrane). The result will be a no flat shape of the device and the deformation will be studied throughout the thesis.

In order to have a better comprehension of the geometry of the die and its main design characteristics some images of the whole simulated geometry are shown in Fig.5.3. In these figures the position of the sixteen membranes within the die can be observed: it is important to say that unfortunately the membranes' arrangement do not respect many symmetries and this aspect has complicated the simulation (i.e. the symmetries approximation can not be exploited).

By looking at the Fig.5.3a, it is possible to see a red line. Its aim is to indicate the position where a cross-section will be taken. In such a way the main features of the design can be studied and moreover the stack materials that make up the membrane will be observed in more details. The cross-section appears in the Fig.5.4.

The main geometric characteristics of the device are indicated by the two black squares. The one on the right (Fig. 5.5a) represents the layered stack over the cavity while the second one on

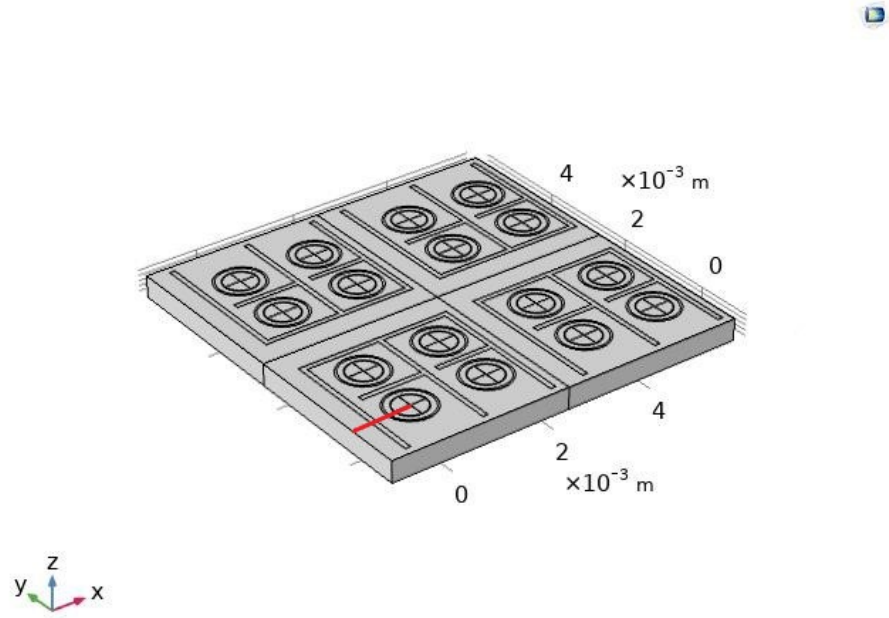

(a)

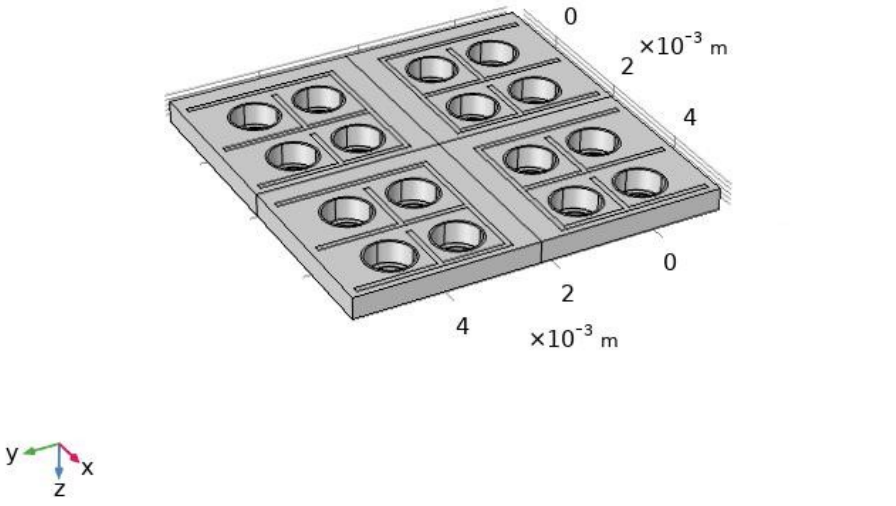

(b)

Figure 5.3: *Top(a) and back(b) view of the die: in the up figure appears a red line and in correspondence of that a cross-section will be taken. Looking at the figure on the bottom the cavities can be distinguished: their diameter is equal to 860* μm.

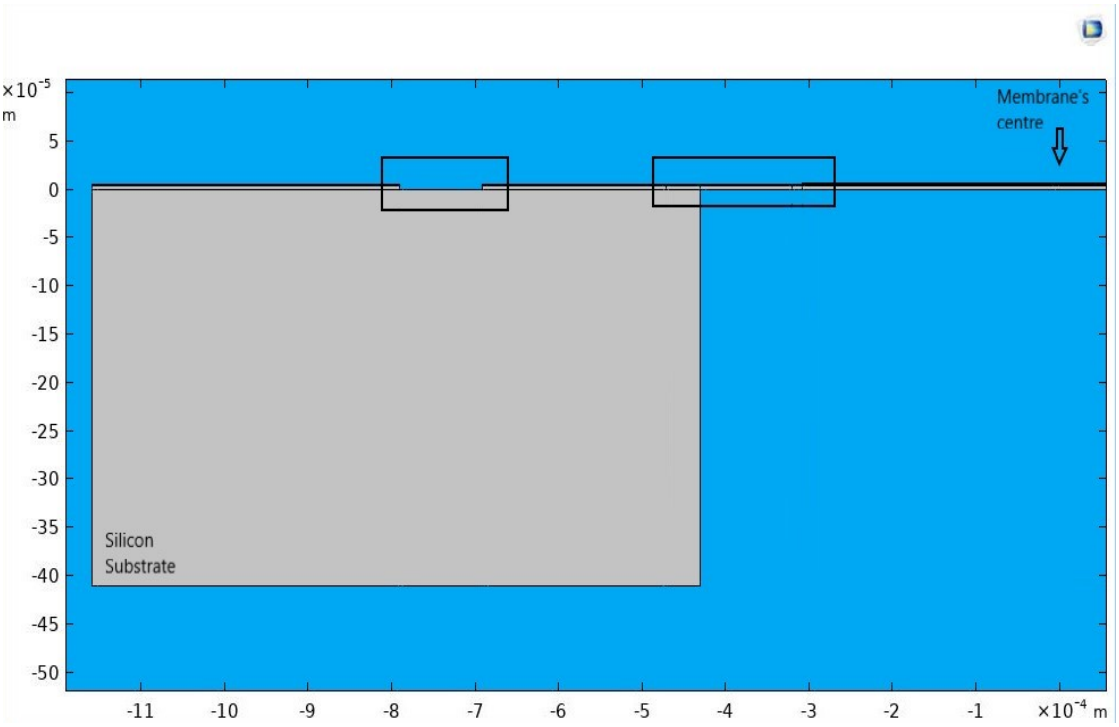

Figure 5.4: *Cross-section in correspondence of the red line in Fig.5.3a. The solid domain are represented in gray while in sky-blue the surrounding air is defined.*

the left (Fig.5.5b) shows a particular design feature. For both cases different colours indicate a particular material. A summary table of the material layers is proposed Table 5.1:

Material
Silicon Oxide
Polycristalline Silicon
Undoped Silicon Glass
Aluminum Nitride
Top electrode (TiW)
Bottom electrode (Pt)
PZT
Silicon substrate

Table 5.1: *Materials' stack composition of the layered membrane.*

As it can be observed in the detail in Fig.5.5a, the layered structure is interrupted moving toward the left (away from the centre of the membrane) where there is the poly Silicon layer only. This design detail is called removal of passivization layers and it is mandatory to avoid and prevent instability phenomena such as buckling [12][5]. In the second detail (Fig.5.5b), it can be observed the so called trench that consists in the removal of the passivisation layers and of the poly crystalline Silicon layer as well. Its aim is to reduce as much as possible the interaction

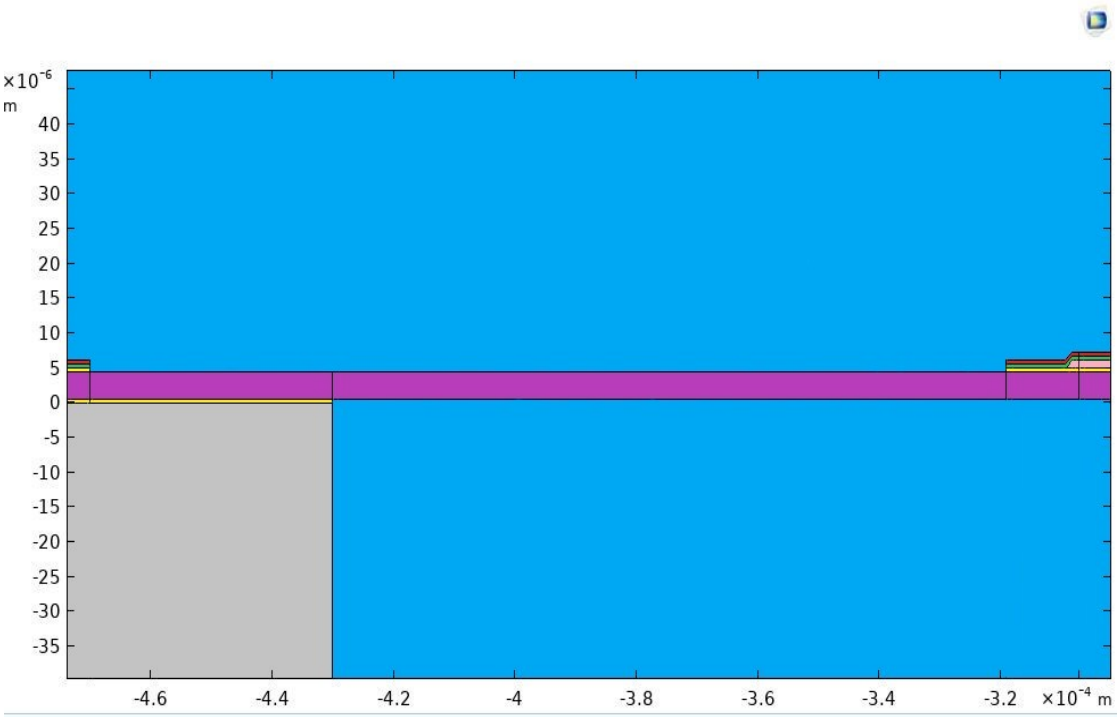

(a)

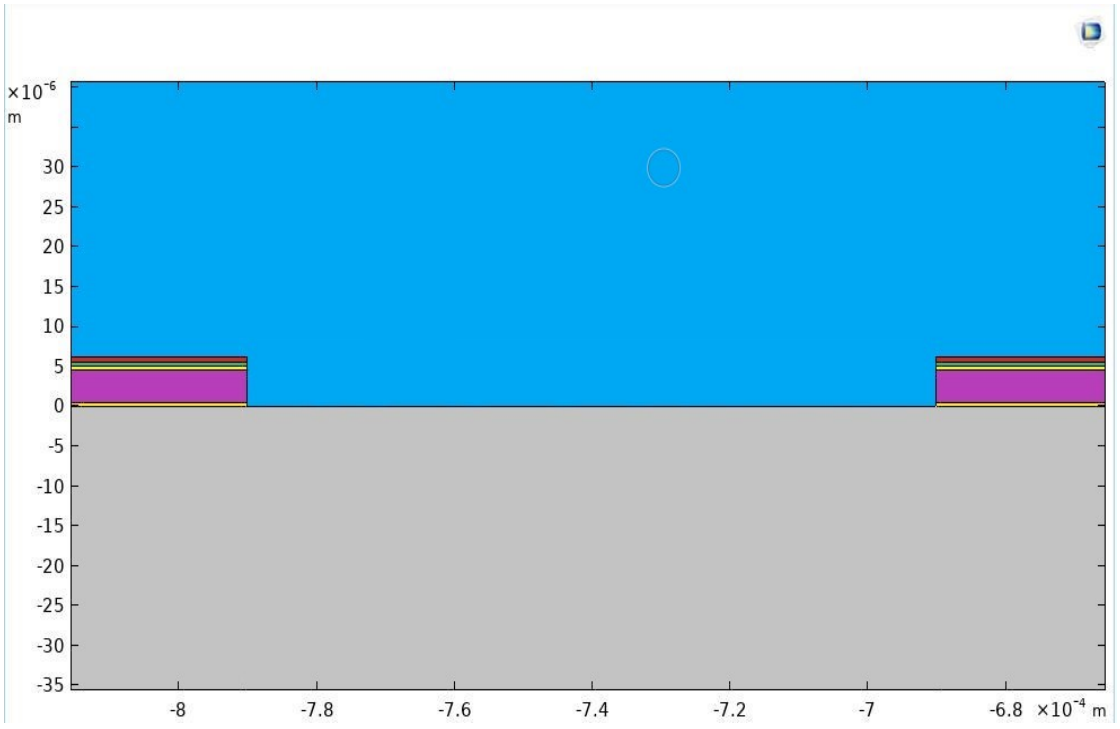

(b)

Figure 5.5: *a) Detail of the design characteristic over the cavity. b) Detail of the trench. In both pictures the colours selected represent a specific material: violet is Poly crystalline Silicon, yellow is Silicon Oxide, pink is the PZT layer, green is the Undoped Silicon Glass (USG), red is the Aluminuim Nitride (AlN) and the brown represents the Silicon substrate.*

between membranes within the whole device.

Even if the previous zoomed details clarify the design features of the PMUT, another image is shown in order to better visualize the materials layers that make up the layered membrane (Fig.5.6).

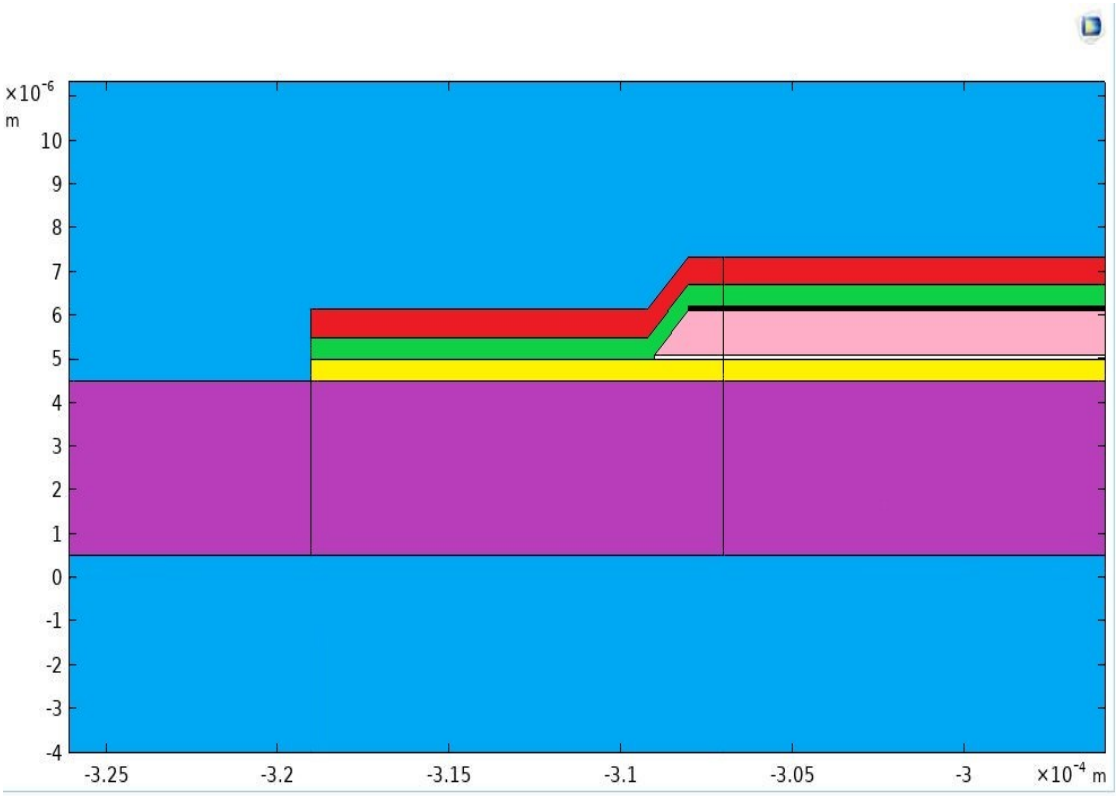

Figure 5.6: *The colours used identify the same material as the previous figure. In addition in this one the top electrode over the PZT and bottom electrode below the piezoelectric layer can be distinguish (respectively in black and white).*

5.2 Experimental equipment and Finite element software

In this section the Polytec MSA500 and the software Comsol Multi-physics 5.6 will be introduced. The aim is to describe the several operating modes and the working principle.

5.2.1 Polytec MSA500

The MSA-500 Micro System Analyzer is a measurement instrument for the analysis and visualization of structural vibrations and surface topography in micro structures such as MEMS (Micro-Electro-Mechanical Systems) devices. The system can work in three different operational modes: Laser Doppler Vibrometer (LDV), white light interferometer (profilometer) and a stroboscopic microscope. Throughout the master thesis only the first two modes have been exploited and now a description of their working principle is proposed.

- **Laser Doppler Vibrometer**: this operation mode is frequently used in the design and testing of products and microstructures such as MEMS. It is an accurate test based on laser interferometry that can measure high spatial resolution vibration without touching the sample under observation. In particular this tool is a fully integrated optical measurement workstation for characterizing out-of-plane vibrations and for computing the velocity and displacement of every points on the sample. The instrument is capable of evaluating deformation and vibration modes, with sub-picometer amplitude resolutions and at frequencies up to 20MHz and to investigate non linear systems. In addition, starting from the measurement of the dynamic deformation in different points of the device, the LDV is able to reconstruct a 3D map of the vibration of the structure. A scheme of the working principle is shown in Fig.5.7

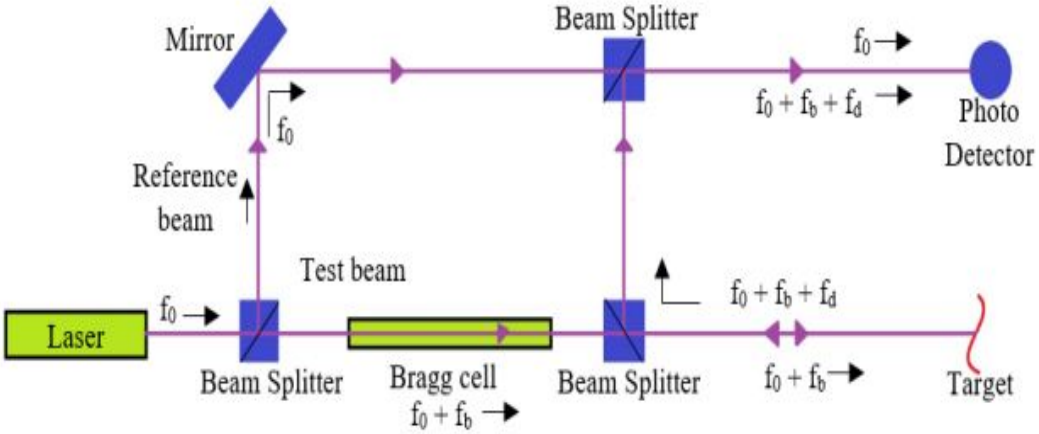

Figure 5.7: *Schematic representation of Laser Dopple Vibrometer working principle.*

The operational mode is based on the interference between a reference beam and the test one reflected by the sample. Looking at the Fig.5.7 a deeper explanation can be given. The test starts with a laser that send a laser beam with frequency f_0 and then it is divided by a beam splitter into the reference beam and test one. The second pass through a Bragg cell which adds a frequency shift equal to f_b. Once passed the cell, the test beam hits the target sample and its frequency changes by a value equal to the the doppler shift f_d. Then the test beam is brought back to combine with that of reference by means of a beam splitter and their interference is analyzed by a photodetector.

By studying the combined laser beam, the tool gives back as a output the frequency modulated signal: through a demodulation it is possible to obtain the velocity of the oscillating object as a function of time. Once the velocity is computed, the software within the equipment is able to measure the actual displacement and reconstruct the 3D video of the movement.

- **White Light Interferometer**: The profile of 3D structure or the roughness on a surface can be measured with vertically scanning white-light interferometer. This tool is included in the Polytec MSA500 functionality and it is a non-contact optical method for 3D profile

measurements of objects with dimensions between several centimeters and a few micrometers. Unlike the other technique such as field of view sampling, triangulation and shearing interferometer, the uncertainty of the topography measurements is quite low and does not depend on optical parameters. Moreover, the white light interferometry does not need any phase unwrapping as is required with method including phase shift. A schematic figure of the tool is shown in Fig.5.8.

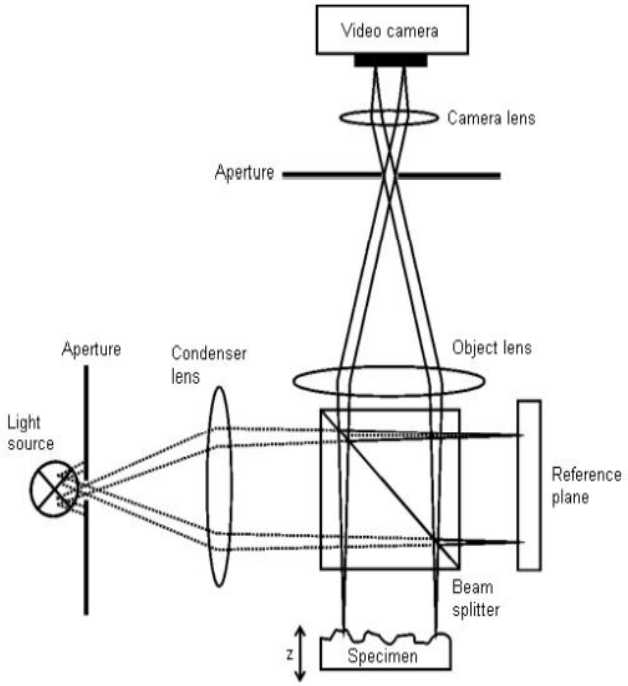

Figure 5.8: *Schematic representation of white light interferometer working principle.*

The system shown in the previous figure can be set up as follows: a condenser lens collimate the light coming from a broadband light source. Then a beam splitter splits the light into the reference beam and the test beam (toward the sample). The former beam is reflected from the reference mirror while the latter is reflected or scattered from the surface of the device under investigation. The returning beams (both reference and test ones) are trasmitted from the beam splitter to the video camera and, depending on the position of the object, create an interference signal for every individual pixel. The video camera used is usually charge coupled devide (CCD) image sensor.

Each pixel of the CCD camera corresponds to a point of the sample's surface. For each pixel, the z value of the target point is defined as the maximum of the modulation of the interference signal. The interference between test beam and reference one can occur only if the optical path lengths of the reference and measurement beam differ less than half the coherence length of the light source (matched path lengths of the two beams). By changing the path length of the reference or the test beam, a interference signal, the so called correlogram, is detected. The key aspect is to find the correlogram with the maximun width because it will correspond to the z value of that pixel and that usually occurs when

the path lenght are exactly the same. An example of correlogram formed in white light interferometer is shown in Fig.5.9.

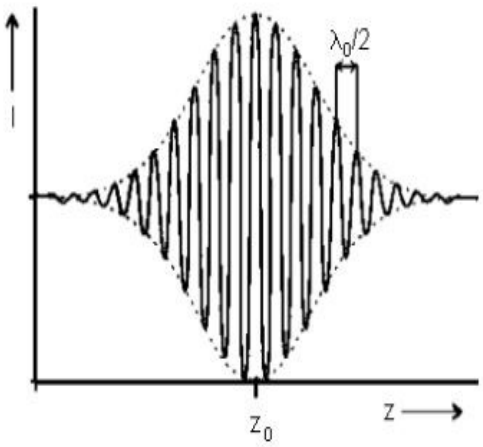

Figure 5.9: *Example of the correlogram obtained from the interference signal. The intensity of the modulation is shown as a function of the vertical position z.*

5.2.2 COMSOL Multiphysics 5.6

The modelling and design of PMUTs is a crucial step in order to predict the mechanical behavior of the device, innovate the products and conceive new geometries to improve their performances. All simulations done during my activity are realized using the software COMSOL Multiphysics 5.6. This program is a computer-aided engineering tool that allows to solve physics numerical problems by subdividing the geometrical domain into smaller parts that are called finite elements (meshing). After that the software computes the partial differential equations associated to the physics involved. Usually typical problem areas of interest include the traditional fields of structural analysis, heat transfer, fluid flow and electromagnetic potential. Moreover, among the different finite element (FE) software available, it has been chosen precisely COMSOL for its reliability to compute Multiphysics mathematical problems. Since in operation conditions the PMUT involves coupled equations between electrostatic-structural mechanics (piezo-electricity) and structural mechanics-acoustic to send the ultrasounds waves, a multiphysical approach is needed.

The several simulations performed try to analyse in detail some peculiar aspects of the device. Among them, the initial static deformation of the membrane and the whole device are carried out through some stationary simulations. The resonance frequencies of the first six vibration modes are computed through frequency study and lastly the ring down of the vibration is analyzed with time dependent models. The latter is performed by changing the environmental fluid (Q factor): air and vacuum.

5.3 Static deformation of the membrane

The first investigation performed concerns the deformed configuration of the membrane. Initially, the experimental campaign to analyze this phenomena is described and then the simulation models will be introduced.

5.3.1 Experimental measurements

The experimental characterization of the static configuration of the membranes is performed by using the Polytec MSA500 in the white light interferometer operational mode. By doing so, it has been possible to obtain the profile in the z direction and evaluate the deformed shape. Once the deformation at 0V is computed, the next step has been to measure the displacement of the membrane as a function of the DC voltage applied.

The equipment used is shown in the Fig.5.10.

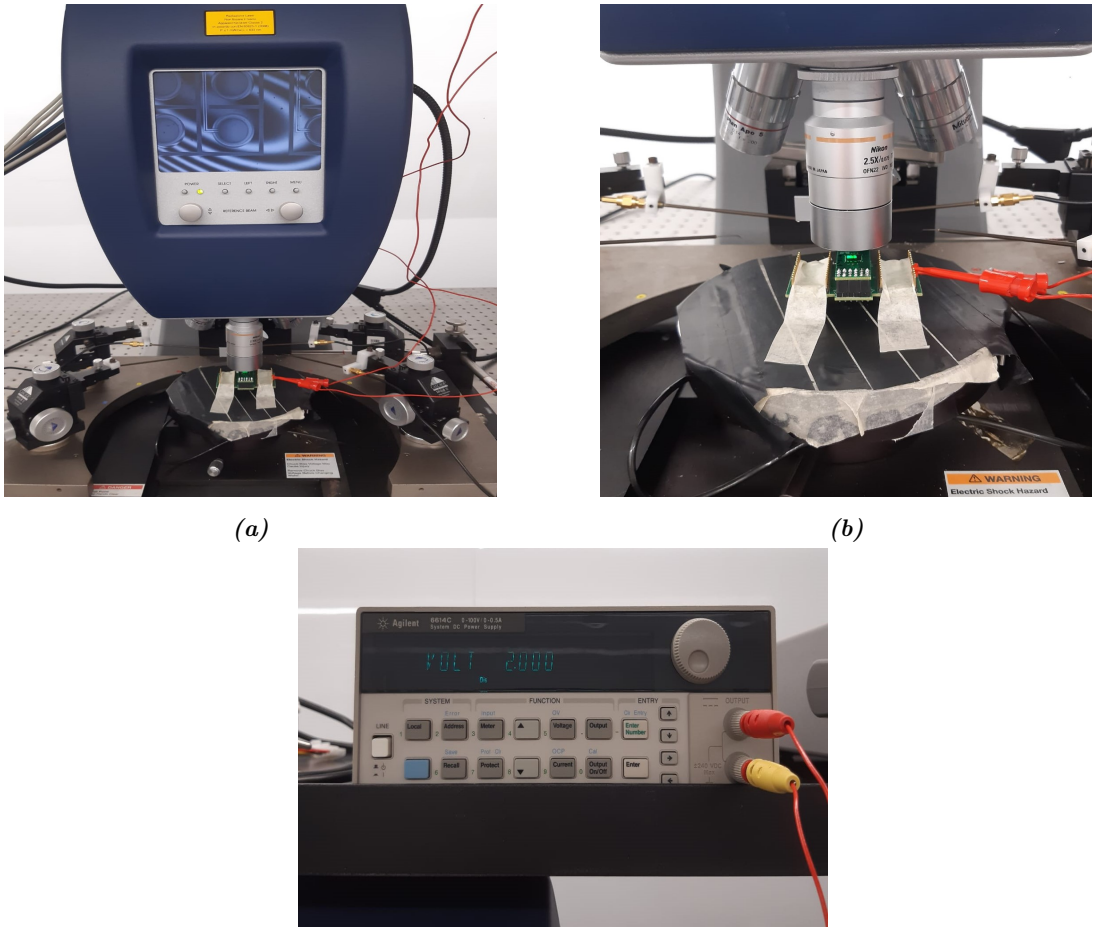

(a) *(b)*

(c)

Figure 5.10: *Pictures of the equipment used. a) shows the scanning head of the Polytec MSA500; in the screen it is possible to see the membranes and optical fringes. b)the sample under investigation where can be distinguished the laser beam and the connection pins. c) DC power supply Agilent 6614C used to apply a DC voltage.*

In order to carry out the topography of the PMUT's membranes in static regime, the sample has to be located below the laser beam and the top electrode must be forced to 0V bias by a voltage generator. The second necessity is mandatory to avoid completely any possible residual polarization that could affect the configuration, i.e. the starting deformation of the membrane. The Polytec scanning head is equipped with a 2.5X photographic objective and it guarantees to cover a quarter of the device. The key aspect to be adjusted to do the analysis in a good way is the alignment between the objective and the surface of the sample. An indicator of this is given by the optical fringes: an example of good alignment is visible in the Fig. 5.11.

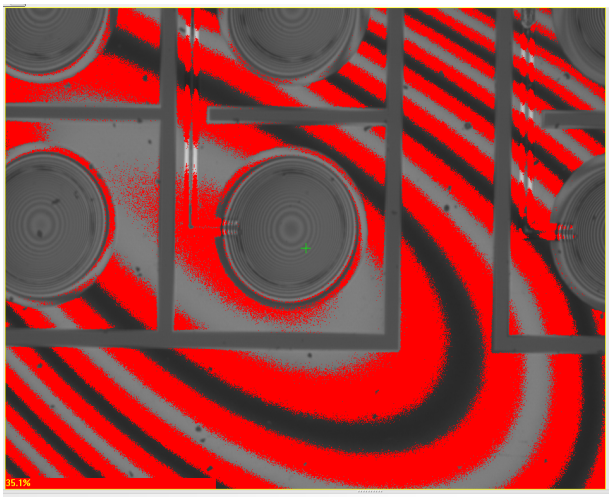

Figure 5.11: *Optical fringes centered around the membrane under investigation.*

They must be clearly visible and the centre has to be aligned with the membrane under investigation: calibration shall be repeated each time a membrane is changed. Some characteristic of the fringes must be clarified in order to make easier the comprehension: a flat surface shows few and big circle, more circles mean a higher curvature and finally a distorted shape is synonym of a stress state (usually torsional one). It is interesting to stress the optical fringes are not completely circular and it is due to a non flat configuration of the die's surface. Also this evidence will be analyzed in more detail throughout the thesis. Once the physical set-up is ready, the following step is to set the proper parameters of the software included in the Polytec. In order to improve the quality of the measurements as much as possible, the sensitivity, exposure time and roughness conditions can be modified. Their tuning has to be repeated at each analysis because some external conditions such as ambient light and vibrations could affect the results.

After the analysis of the static deformation, the next study is focused on the variation of the deformed shape as a function of the DC voltage. The set-up is exactly the same, but in this case a DC Voltage equal to 5, 10,15 and 20 V will be applied to the top electrode by means of the voltage generator. In all the experimental characterization, the bottom electrode is always grounded while the voltage is applied to the top one. This choice has been done because this actuation mode guarantees a longer stability of the piezoelectric layer and it delays the aging phenomena.

The topographic measurements is repeated for the sixteen membranes within a die and the experimental results will be shown in the following chapter.

5.3.2 Simulation modelling

The investigation of the deformed configuration of the membranes is also carried out by means of the Comsol models. In this subsection, the 2D axisymmetric model and the 3D model of a single membrane will be described.

- **2D axysimmetric model**: As initial model, the easiest case of a 2D axisymmetric model of a single PMUT membrane is considered. In this kind of model, the geometry of the device can be modelled in the 2D meridian plane $(r^+ - z)$ and subsequently the whole 3D representation of the model can be obtained by exploiting the symmetries around the z axis at $r = 0$. Therefore, the first step of the creation of the model is the design of the device's geometry. In Fig.5.12 the entire geometry of the single PMUT membrane with open cavity is represented and the blue line highlights the clamped boundary condition at the bottom of the Silicon domain.

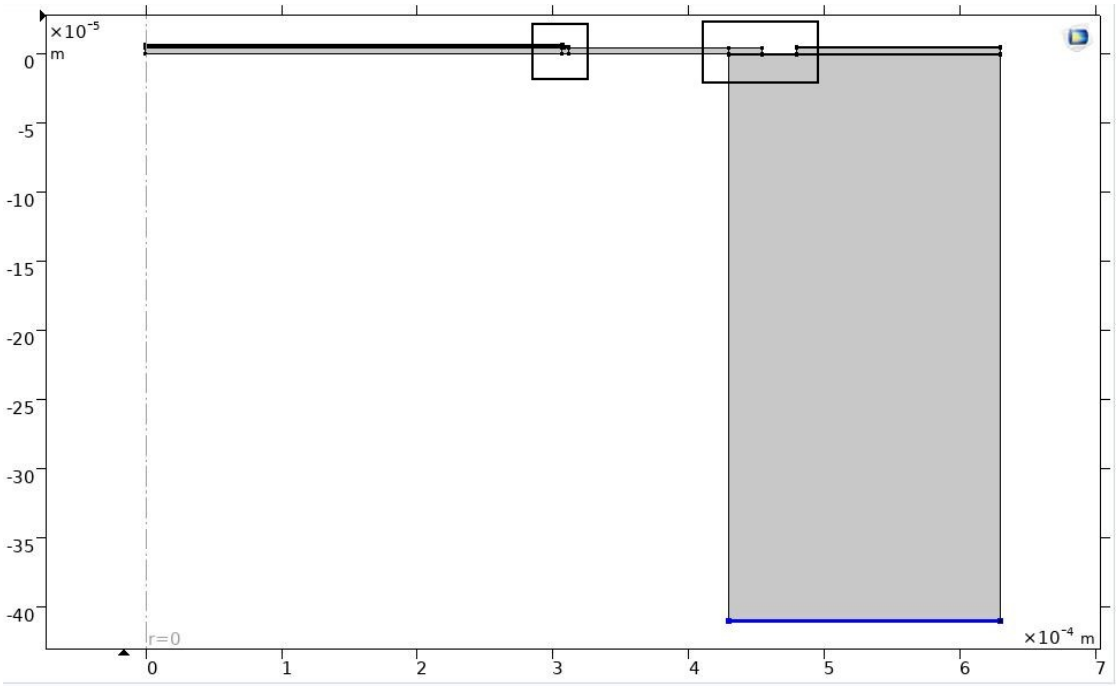

Figure 5.12: *2D axisymmetric single PMUT geometry. In the black squares appear the two design characteristics explained in the section 5.1 respectively the removal of passivation and the trench. Regarding the second detail, it is important to say that in this model where only a single membrane is represented there is not possibility of interaction but anyway it can affects the deformed configuration.*

Once the geometry is defined, the second step is the assignment of the mechanical parameters corresponding to each material: Young's Module, Poisson's ratio, density and residual stresses coming from the fabrication process. All these parameters are confidential information provided by STMicroelectronics and for that it has been decided not to report the numerical values.

At this point of the discussion, it is useful to clarify the physics involved in the model and the

studies performed. Starting from the physics used, the model includes the solid mechanics and the electrostatic modules. In the first one, all the structural parts are considered and essentially this interface is based on solving the equations of motion together with a constitutive model for different solid materials. Results such as displacements, stresses, and strains are computed. Inside this node it is possible to add the boundaries conditions, the residual stresses and the kind of materials to be studied. In my model, it is necessary to add the linear elastic material node and the piezoelectric material one (specifically for the PZT layer) where the last one defines the piezoelectric material properties in stress-charge form using the elasticity matrix and the coupling matrix. It is normally used together with a piezoelectric effect multi-physics coupling node and a corresponding charge conservation such as the piezoelectric node in the electrostatics interface. Indeed, in order to couple the mechanical and the electric behavior of the PZT, the electrostatic node is introduced. Regarding the studies performed using this model, the stationary study to measure the initial static deformed shape is carried out. This takes into account the solid mechanic, electrostatic and piezoelectricity nodes and compute the stress state within the membrane. As a result, the solver will give back the deformed shape: the simulation is run for values of DC voltage equal to 0, 5, 10, 15 and 20V.

The last step of modelling concerns the creation of the mesh. The solid domain (Fig.6.24b) is discretized by using mostly square finite elements with four nodes. In the region close to the inclined of the PZT and in the Silicon substrate domain, the triangular elements are selected to better suit the geometry. All the elements used belong to the quadratic serendipity family [32]. The size of the elements is selected by means an iterative approach: starting from an extremely fine mesh, the size is made coarser until the results remain in accordance with those of the initial meshing. In this way a good balance between accuracy and computation time is achieved. Images of the final selected mesh are shown in Fig.5.25a and 5.25b.

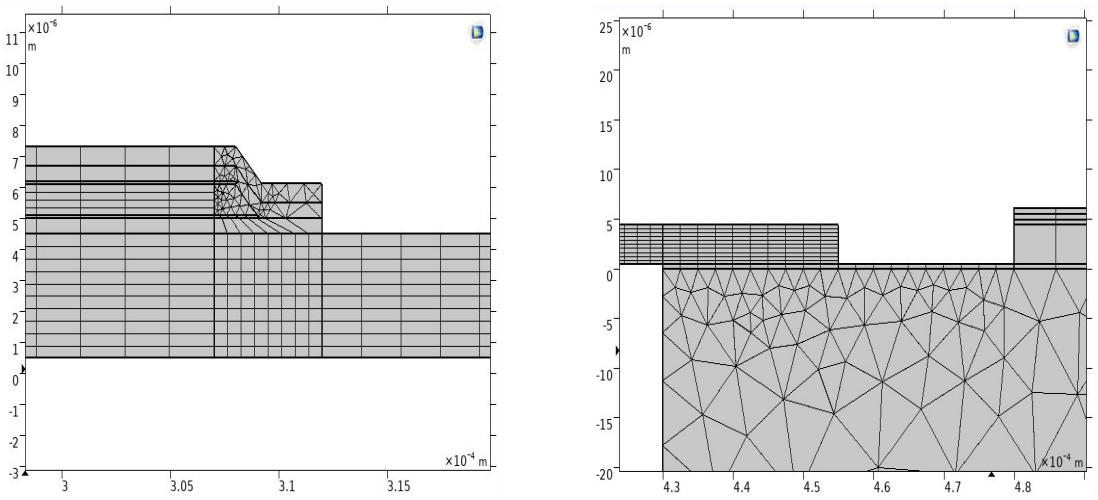

(a) *(b)*

Figure 5.13: *Meshing of the solid domain. a) and b) show the mesh in the characteristic details.*

- **3D model**: At this point the 3D model, an upgrade of the previous 2D axisymmetric model, is described. The design of the device, material layers, physics involded and the study performed (stationary) are equal to those of the model of the previous subsection. Instead of modelling in a 2D environment and then obtaining the 3D through a rotation, in this case the model is built directly in a 3D space. Essentially the main difficult has been the more complex CAD (Computer Aided Design) required abilities. In Fig.5.14 are reported some pictures of the 3D design of a single membrane.

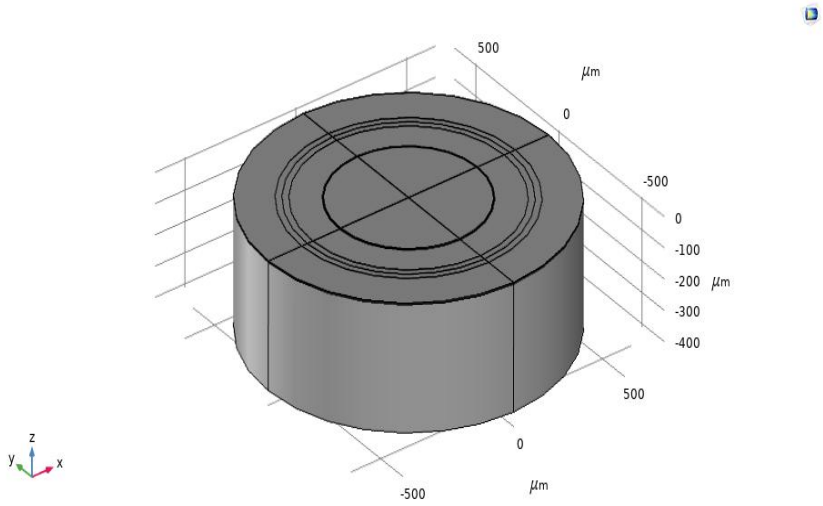

(a)

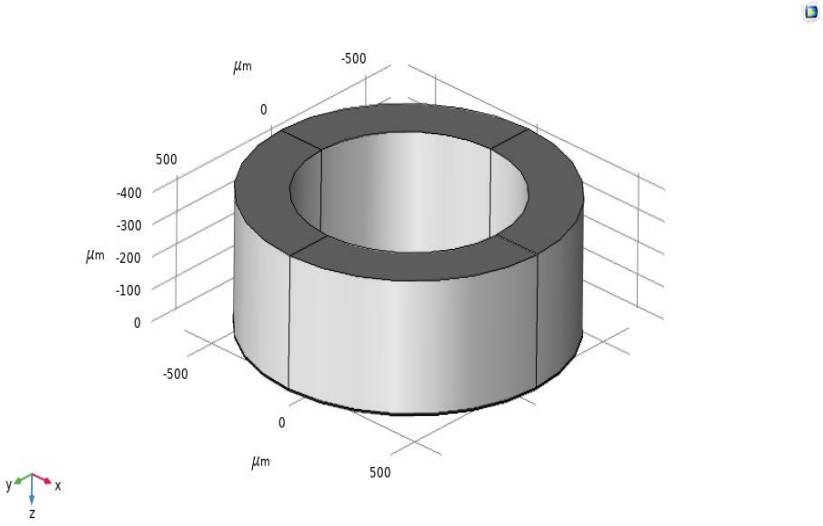

(b)

Figure 5.14: *Geometry of the 3D single membrane. a) Top view. b) Back view where the cavity can be seen.*

Once the geometry is built and the mechanical parameters are assigned to each materials, the next step is the creation of the mesh. Also in this model the approach selected has been an iterative one: start with a extremely fine mesh and then make it coarser until a good

compromise between accuracy and computational time is achieved. Unlike the previous model, the meshing step requires greater attention and cunning. In order to obtain a convergence in the simulation and a compatibility among the finite elements, the mesh has to be created taking into account the way through which the geometry had been built. The meshing process is characterized by the creation of a 2D mesh on a surface to which is added the third dimension through rotation sweeps and extrusions. The more the meshing steps follow the way through which the geometry was built, the easier is the convergence. Also in this model the elements used belong to the family quadratic serendipity[32]. The final mesh adopted in the 3D single membrane model is shown in Fig.5.15.

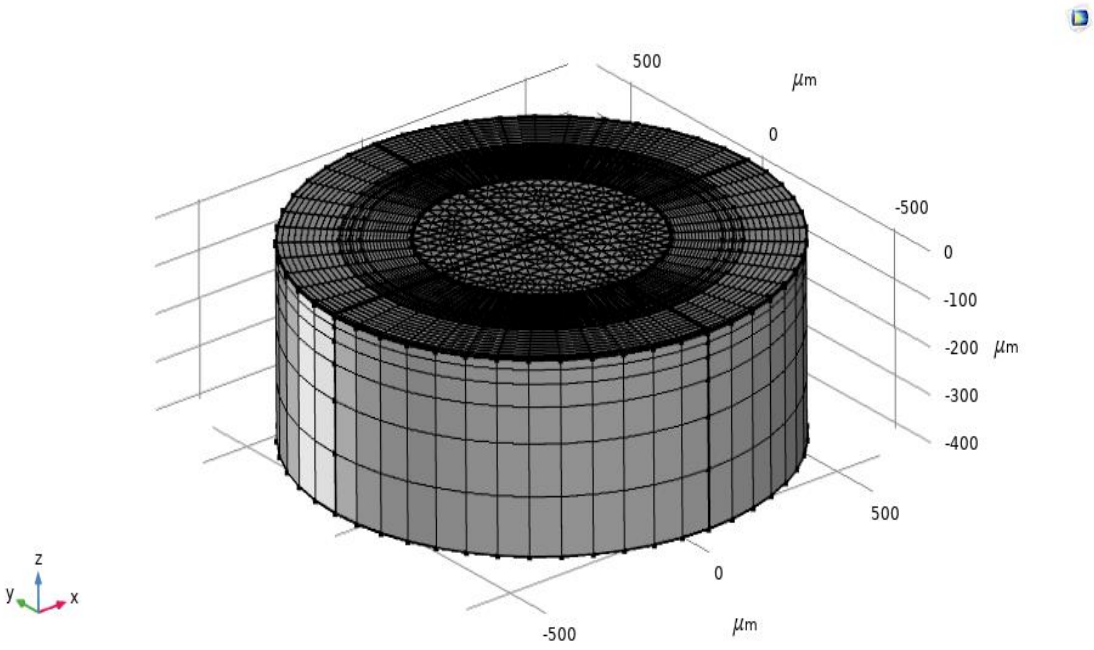

Figure 5.15: *Mesh of the 3D model. As can be observed, a key aspect to be considered is to use smaller size elements for the movable parts and coarser ones for the fixed portions. In this way a good balance between accuracy and computational time is guaranteed.*

5.4 Static deformation of the whole die

In this section the experimental and modelling activity aimed at measuring the static deformation of the entire die is described. The main parameters measured have been the ratios of curvature (ROC) along the y and x axis, the Δz between the centre of the die and the vertices and the Δz between the centre and the centres of the edges. Looking at the Fig.5.16a can clarify the parameter just explained: the point 1 represents the vertices, 2 the centre and 3 the centre of the edge.

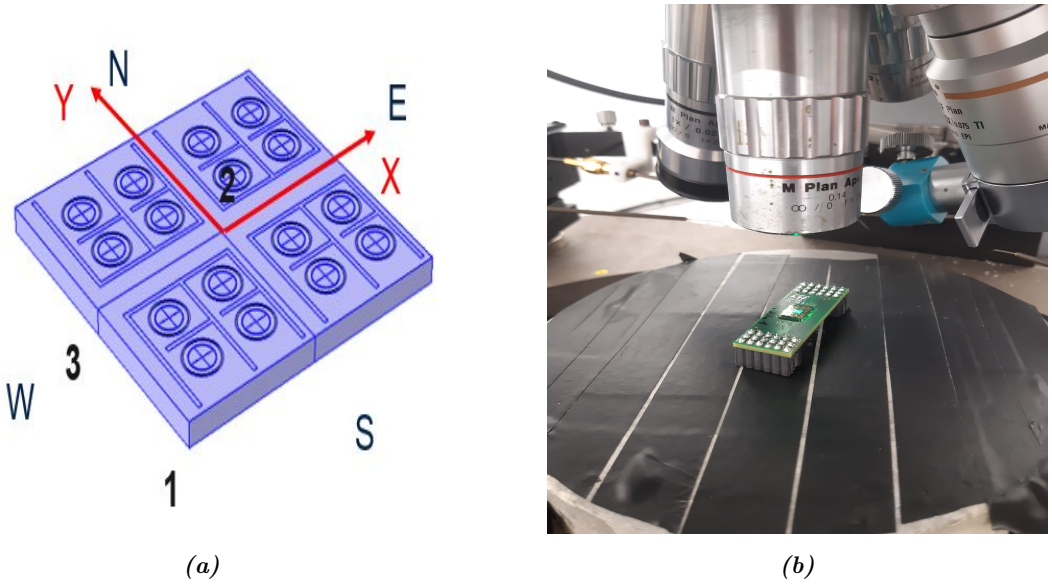

(a) *(b)*

Figure 5.16: *a) Schematic representation of the die in which the axis and critical points appear. b) Physical experimental set up condition.*

5.4.1 Experimental characterization

This experimental analysis is done using the Polytec in topography mode without the necessity of the DC power supply.

Unlike the equipment, the experimental physical set up must change: the TMA board, on which the device is attached, can not be connected to the expansion board (see Fig.5.1). This is mandatory because the connection causes additional stresses in the die structure and in turn the deformation state is altered. Theoretically, the ideal set up would be investigating the bare device because even the bonding between the die on the TMA board causes a change in the configuration. Indeed, as shown in the section 5.1, the application of the epoxy glue on the four edges and the subsequent curing process causes a state stress variation. it is due to the mismatch of the thermal expansion coefficient between glue, silicon and TMA. The deformation introduced by the connection on the expansion board is much higher than that of the bonding through epoxy glue. Therefore, the measurements of the ROC and the different Δz of dice are performed on die only attached to the TMA as shown in Fig.5.16b

An indicator of the flatness of the die are the optical fringes and in Fig.5.17 their shape are shown in order to point out the differences just explained.

In Fig.5.17, it is clear how the deformation state changes upon the connection to the expansion board and how this altered configuration is still present even after removal.

Due to this problematic and in order to guarantee a good reliability, the experimental campaign is performed on 21 device never placed on the expansion board. The results of the experimental ROC and the different Δz will be shown in the following chapter and a comparison with the simulation will be proposed.

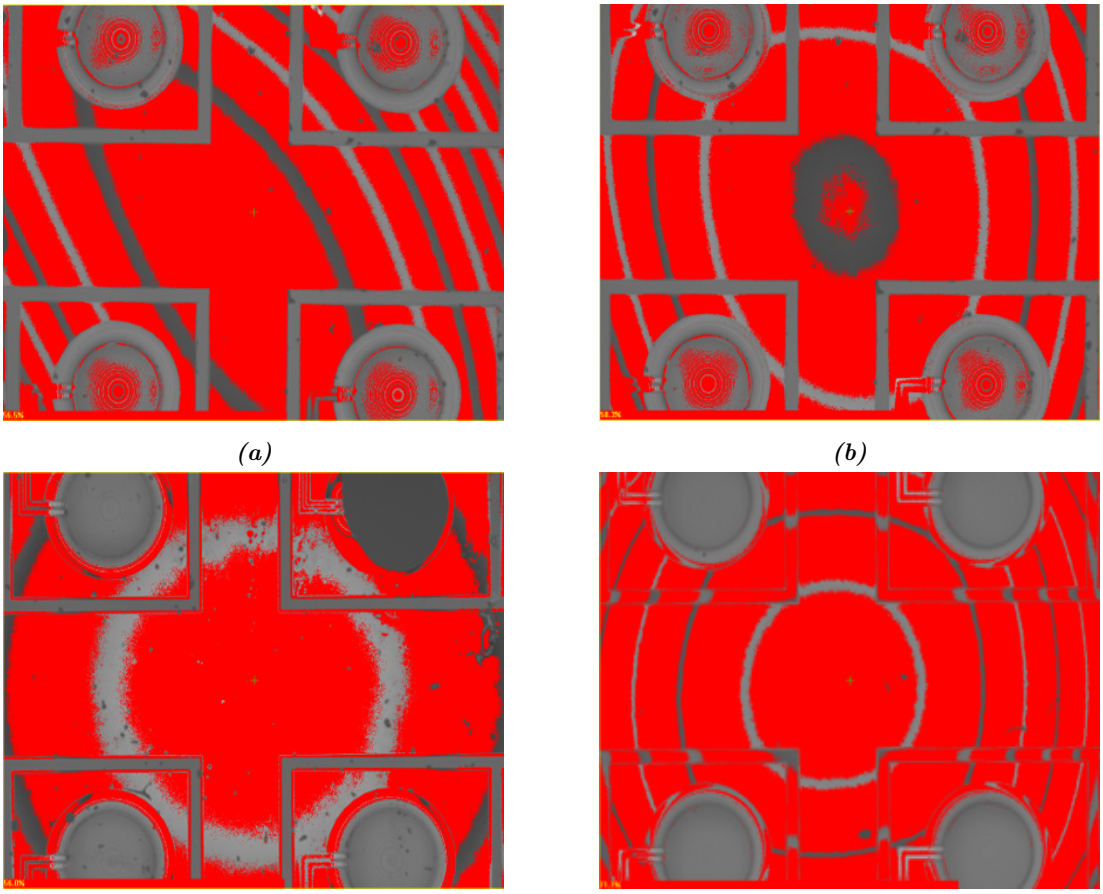

Figure 5.17: *Optical fringes. a) Die placed on TMA and expansion boards; b) Device placed on TMA after a period connected to the expansion board; c) Bare device; d) Device on TMA never placed on expansion board: the shape of the fringes is almost circular.*

5.4.2 Simulation modelling

In order to simulate the deformed static configuration it is needed to construct a model of the whole device and run a stationary simulation. Also in this case the main difficulties concerns the creation of the geometry and meshing: higher CAD skills than the previous cases are required. Due to the symmetry limitation, at least half die must be designed and only then a symmetry condition can be exploited to obtain the entire one.

The geometry of the entire device has been already shown in previous section 5.1. In this section the focus is given to the boundaries condition applied to obtain the right configuration and the meshing. Respectively, it is necessary to clamp the four vertices in all direction, apply a Winkler's bed of spring on the four edges and then apply a distributed force toward the positive direction of z axis over the bottom surface of the device. The numerical values of the springs' stiffness and the magnitude of the superficial force are obtained by exploiting an iterative approach up to fit properly the experimental evidences.

After that, the meshing step is performed by using quadratic serendipity finite elements. It

is important to stress that in this case the number of degrees of freedom to solve by the software is quite high and it is necessary an elevated computational power. In Fig.5.18 the boundaries condition and the meshing are shown.

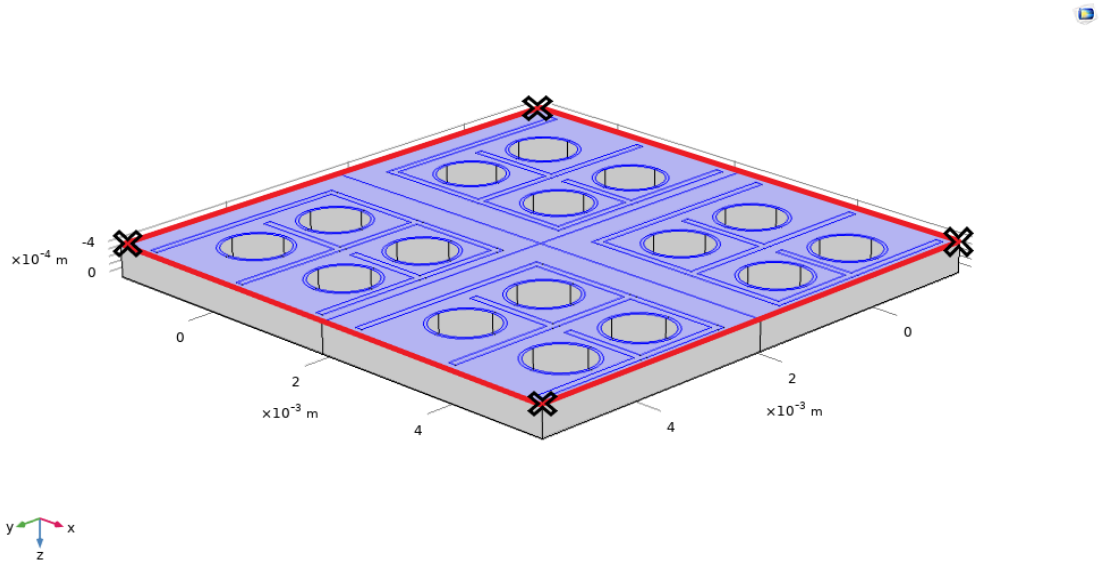

(a)

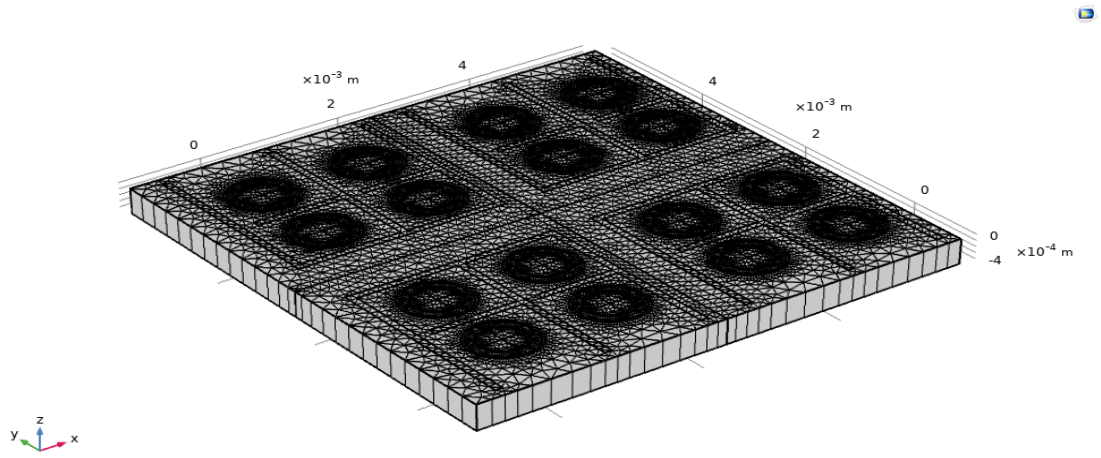

(b)

Figure 5.18: *Design of the whole device. a) Back view of the die. On the blue surface is applied the boundary load toward z^+, the red lines represent the Winkler springs and the X the clamped vertices. b) Meshing of the array.*

In the following chapter the results will be shown.

5.5 Resonance frequencies of the membrane.

In this section of the thesis the resonance frequencies of the membranes are investigated. Of course, the frequency of the first mode (piston-like) is the most important since it is the vibration mode used in application; Nevertheless, the activity covers the frequency of the first six modes to have a better characterization of the device properties.

5.5.1 Experimental characterization

In order to measure the several resonance frequencies of the membrane the instrumentation used is the Polytec MSA500 in laser dopple vibrometer configuration whose working principle is explained in the section 5.2.1. The test consists in a small signal characterization where the membrane under investigation is actuated through an AC signal with frequency ranging from 100 kHz to 450 kHz and amplitude equal to 0.1 V. In this kind of analysis a signal called Chirp is sent and it is based on the frequency sweep. In addition, during the experimental investigation the attention is focused on the variation of the frequencies as a function of the DC voltage applied: the chirp is performed in parallel to a DC voltage application ranging from 0 up to 20 V.

The Polytec includes all the instrumentation needed to carry out the frequency sweep and chirp analysis. Indeed, the wave form generator creates the AC voltage function to apply to the membranes, the scanning head receives the reflected laser beam from the sample and the vibrometer controller postprocesses the results. See Fig.5.19.

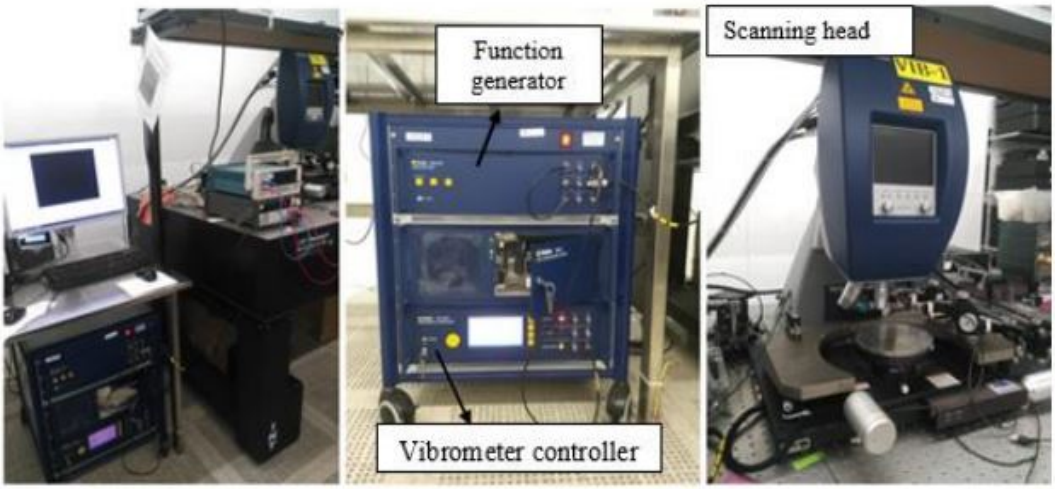

Figure 5.19: *Polytec MSA500 entire set up.*

Theoretically, the equipment would also be able to apply the DC voltage but only up to values equal to 10 V. Due to this limitation, the continuous DC voltage is introduced by means of an external generator equal to that used in the previous section (Agilet 6614C Fig.5.10c). A decoupling between the AC and DC voltage is possible by applying a suitable decoupling net on the pin to be actuated. In this investigation, the scanning head of the Polytec is equipped with an microscopic 5x objective to better focusing on a single membrane only. Once the sample membrane is placed below the laser beam, it must be guaranteed a good parallelism between the

sample surface and the charge coupled device (CCD) image sensor to be sure that the reflected laser will be at its maximum. The following step is the creation of the mesh of the scanning point on which the frequency sweep must be performed. The more scanning points and the better the result obtained. Basically the Polytec acquires the displacement out-of-plane of the points caused by the wave function application for all the frequency belonging to the bandwidth selected. As a results the test gives back a frequency spectrum where each peak corresponds to a resonance frequency and a 3D image simulating the displacements for each frequency value within the bandwidth selected.

In the Fig5.20, the mesh of the scanning points is shown together with some examples of the 3D reconstruction of the displacement out-of-plane.

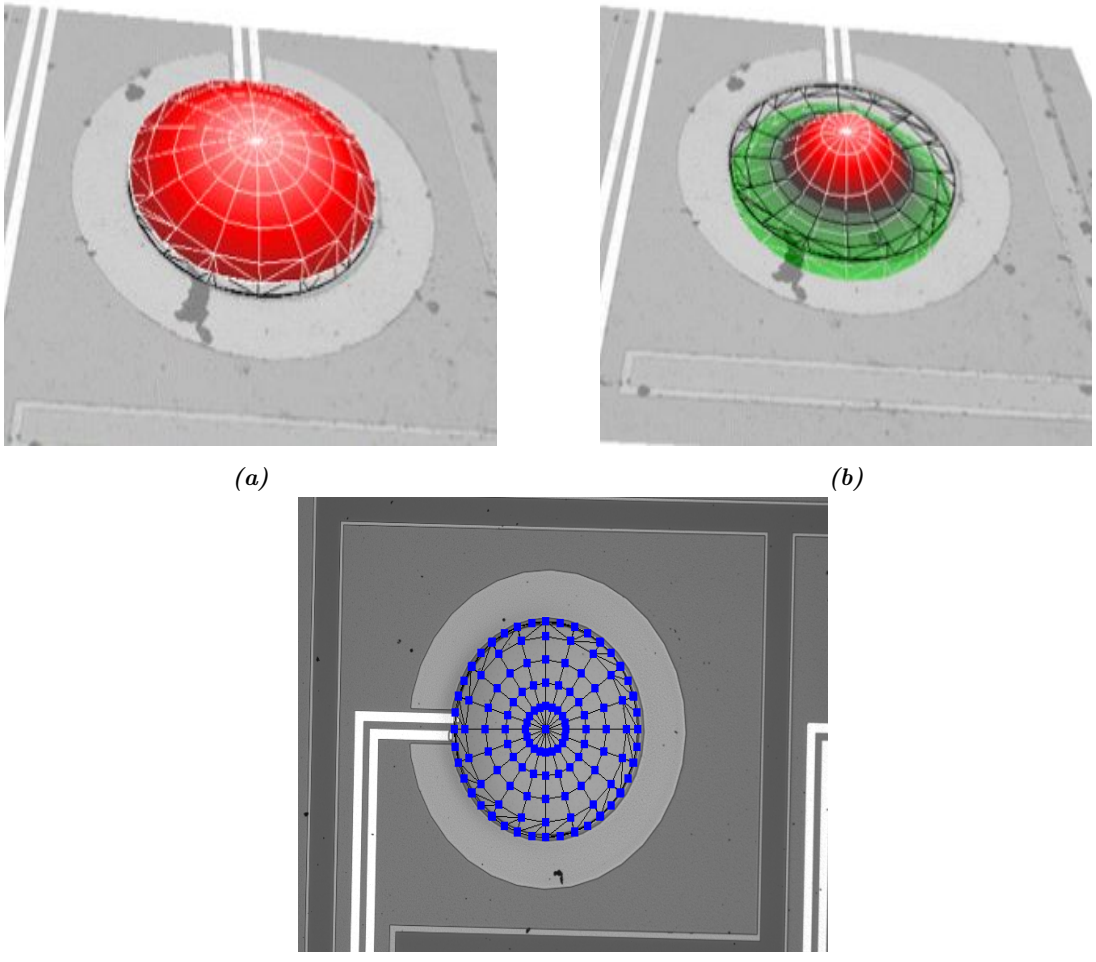

(a) *(b)*

(c)

Figure 5.20: *a) 3D reconstructed image of the first vibration mode out-of-plane. b) 3D reconstructed image of the sixth mode out-of-plane. c) Mesh of the scanning points.*

The frequency spectrum obtained and the values of the resonance frequencies will appear in the following chapter in parallelism with the simulation evidences.

5.5.2 Simulation modelling

The models used to perform the frequency analysis are equal to those described in subsection 5.3.2 in terms of geometry, mesh and physics involved (structural mechanic, electrostatic and piezoelectricity). The main differences concern the studies selected and the application of an harmonic potential in addition to the DC one. The second characteristic is added in the electrostatic node and in order to be as coherent as possible the same value used in the experimental characterization is chosen: AC voltage equal to 0.1V. Both in the 2D axisymmetric model and the 3D model single membrane, the studies performed are prestressed eigenfrequency and prestressed frequency analysis. The former computes the deformed configuration and subsequently solves the eigenvalues problem to measure the eigenfrequency of the first six modes. On the other hand the latter works in the following way: once defined the stationary configuration, computes the frequency spectrum similarly to the experimental chirp (by applying a frequency sweep). Also in this case the bandwidth investigated is equal to that of the experimental campaign (100 kHz, 450 kHz). It is useful to anticipate that the 2D model is able to measure and detect only the vibration modes with symmetry to the centre. This limit is intrinsically bonded to the 2D space where the model is built. Conversely, the 3D one can also compute the other modes.

5.6 Oscillation Ring down

The last investigation concerning the mechanical characterization is related to the ring down of the oscillation over time. It is computed for the first vibration mode and thanks to this analysis it is possible to estimate the damping of the membranes and to calculate the Q factor parameter. As introduced in section 2.2.3, it is a key quantity to characterize the device and define its applications. The measurement is performed in two different medium, air and vacuum (-10^5 Pa, the vacuum level achievable by means of our vacuum pump) respectively, to estimate the damping change by varying the fluid component.

5.6.1 Experimental characterization

This experimental analysis is carried out using an external waveform generator Agilent 33521A and the Polytec MSA500 in LDV mode. The first instrument sends the actuation voltage function to the device and the trigger time for acquisition to the Polytec while the second receives the laser wave reflected from the sample surface and subsequently processes the results. In Fig. 5.21a and 5.21c the wave form generator with its output signal cables is shown.

Before performing the test, the parameters defining the voltage function must be defined. They are the signal frequency, DC voltage, AC voltage, number of sinusoidal pulses and trigger time. Every membrane has to be actuated at the own resonance frequency of the first vibration mode (the like-piston one, see Fig.5.20b) and so the frequency results obtained in the frequency analysis are selected. As regard the voltage values, it has been decided to select the following set up: 4V DC and a variable AC voltage with an amplitude ranging from 0.1V to 4V. The choice has been taken in relation to the voltages usually used in application and because it guarantees to apply a uni-polar potential to the thin film piezoelectric layer avoiding aging problems. Lastly, it is chosen to send a single pulse signal and the trigger time is defined. The second parameter provides the acquisition time to the Polytec and it must be higher to the time needed to damp completely the membrane oscillation. As introduced before the analysis are performed with two

different surroundings fluids: air and vacuum.

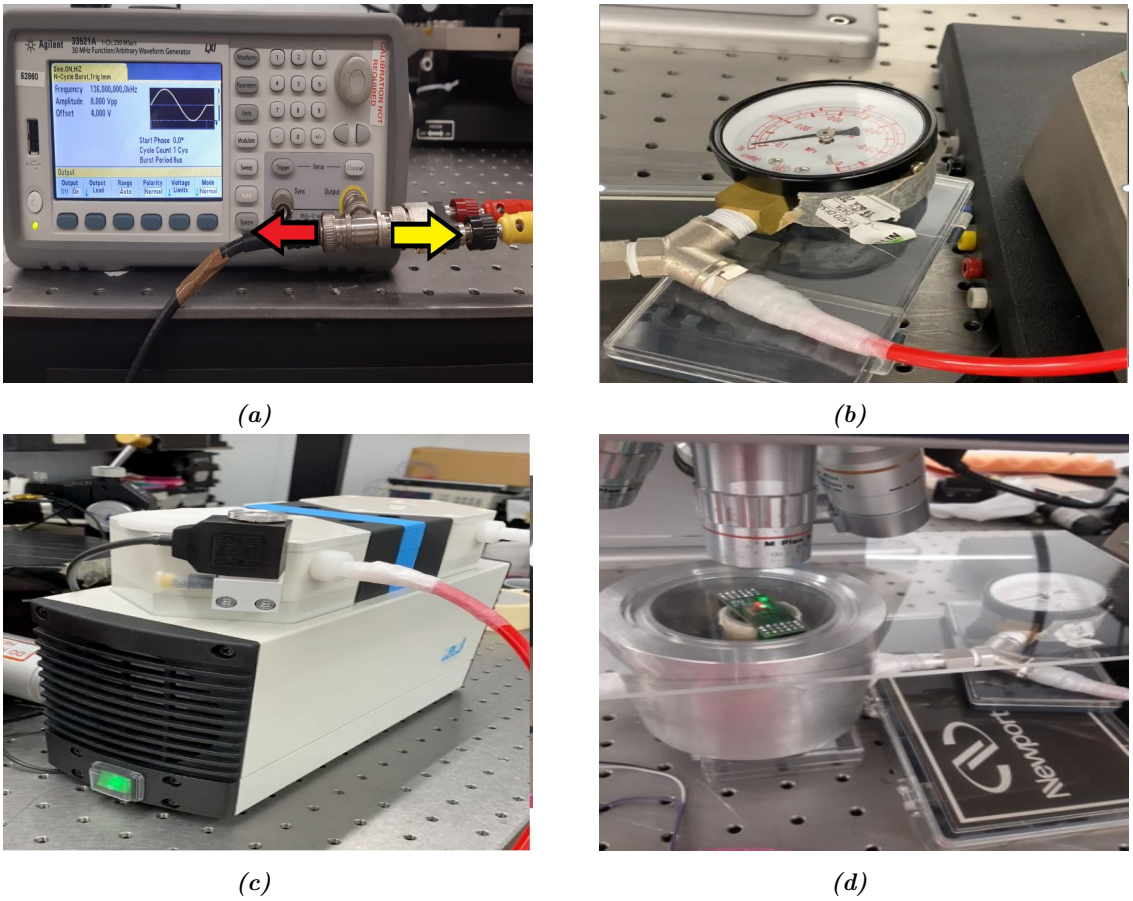

Figure 5.21: *a) Wave form generator Agilent 33521A. The arrows show the output signal: the trigger time (yellow arrow) toward the Polytec while the voltage function/ground (red) toward the Top/Bottom electrode. b) Barometer to measure the vacuum level. The value shown in the picture is equal to* -10^5Pa. *c) Mechanical vacuum pump. d) Physical set up for vacuum measurements. The transparent cover is made of plexiglass (PMMA) and it allows to seal the cage.*

The desired vacuum level is created inside a hermetic cage through a mechanical pump (see Fig.5.21c). Unfortunately, the available cage is too smaller to contain the die on the expansion board and so the actuation signal is send directly to the TMA pins. The physical set up containing the PMUT sample and the vacuum pump barometer are shown in Fig.5.21d and 5.21b. As regard the frequency with which to activate the oscillation in case of vacuum it is important to do a specification. Indeed, if in first approximation the PMUT membrane is considered as an oscillator with a degree of freedom, a lower component of fluid damping would shift the resonance peak toward a little higher values [5]. Therefore, its evaluation has to be repeated by means a chirp analysis. All the sixteen membranes within a die has been analyzed and the results obtained will be analyzed in the next chapter.

5.6.2 Simulation modelling

In order to simulate and modelling the oscillation ring down, it is necessary to use a model of the whole die. Indeed, it is not possible to perform the simulation with 2D/3D single membrane models because their boundaries conditions do not suit the real configuration of the device and an altered damping would be detected. In addition to the solid domain representing the device, whose model has been already described in section 5.4.2, it is necessary to add the fluid domain. In this way it is possible to simulate the presence of a fluid and partially its damping contributions. For this purpose, it is chosen to add a semi-spherical domain with radius equal to 2 cm over the device and fill the cavities of the membranes. About this domain some important details must be taken into account regarding the meshing, the condition onto the external surface and physics involved.

- **Meshing**: The mesh is realized by using free tetrahedral finite element belonging to the quadratic serendipity family. The size of these elements must be selected in relation to the wavelength of the ultrasound radiation. In order to have a good discretization of the fluid domain, it is necessary to have as a maximum dimension a value equal to $\lambda/6$. By knowing the relation between the wavelength λ, frequency f and sound velocity c, the previous relation becomes equal to:

$$\frac{c}{6 \cdot f} = \frac{343 \frac{\mathrm{m}}{\mathrm{s}}}{135\mathrm{kHz} \cdot 6} = 4.23 \cdot 10^{-4}\mathrm{m} \tag{5.1}$$

  In Fig. 5.22 and 5.23 two different views of the fluid domain are shown.

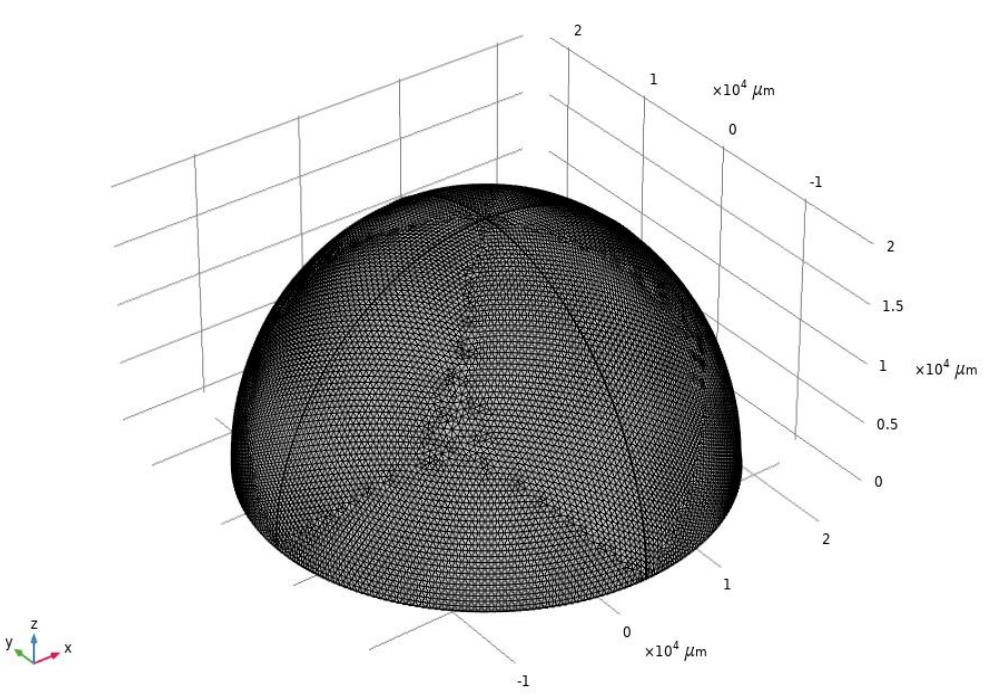

Figure 5.22: *View of the fluid domain's mesh.*

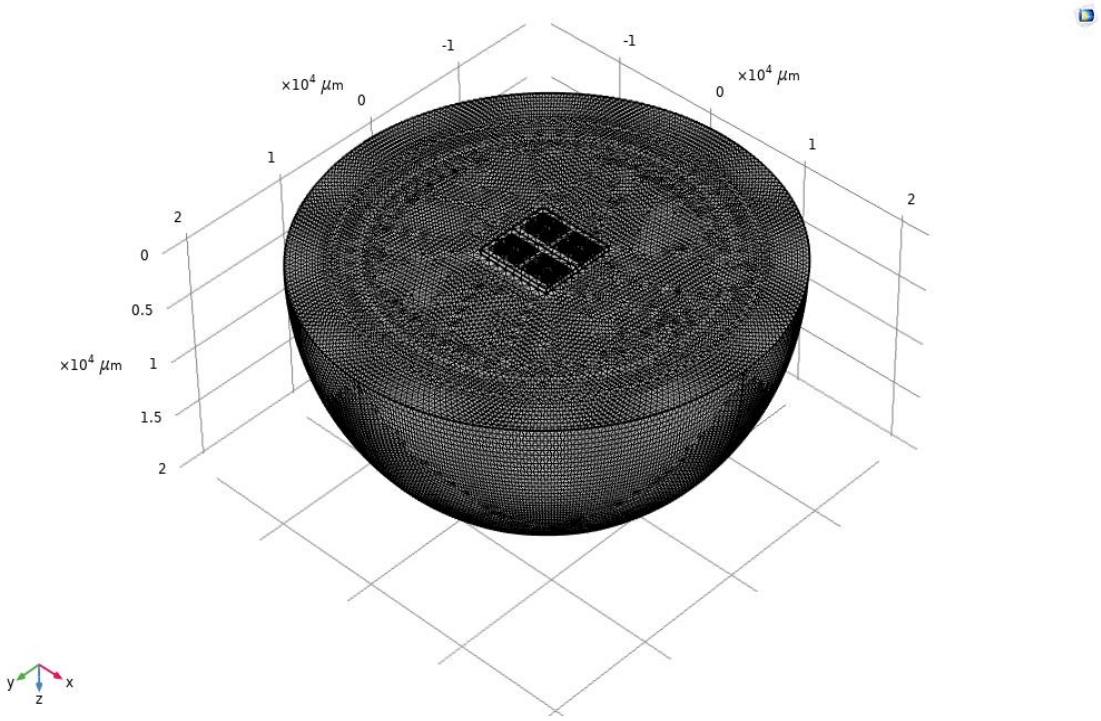

Figure 5.23: *View of the fluid domain and device's mesh.*

- **Spherical wave radiation**: An important characteristic of the fluid domain concerns the boundary conditions onto the external surface. If the acoustic waves were reflected from the surfaces and returned back to the device, the normal oscillation would be compromised. In order to avoid this scenario, it is mandatory to add a condition of spherical wave radiation. In such a way, the domain is considered as a infinite and the acoustic field is completely transmitted without any reflections. Another option could be the use of a Perfectly Match Layer (PML), which, however, would have involved the addition of an further domain and thus lengthened the computational times.

- **Pressure acoustic node**: In order to take into account the presence of a fluid, another physics must be included in the model. Indeed, the fluid domain is added into a pressure acoustic module where the differential equations introduced in chapter 4 are solved.

After the explanation of the fluid domain, the discussion of the modelling design moves on the introduction of the study, voltage signal and the damping coefficients. The study performed is a time dependent one due to the necessity of studying the vibration over time. Unlike the previous cases, in order to make possible the convergence of the software and not affect the acoustic field, there is a key condition to respect regarding the residual stresses. They must be introduced in a nearly stationary way and so the deformed configuration is obtained after a time interval. To do that the absolute value is multiplied for a previously defined function. Similarly, also the DC voltage application must be introduced in a stationary wave. Once again, the values chosen to perform the simulation both in air and vacuum are equal to those used in the experimental characterization. An example of the function to apply the DC and AC voltage

is shown in Fig.5.24.

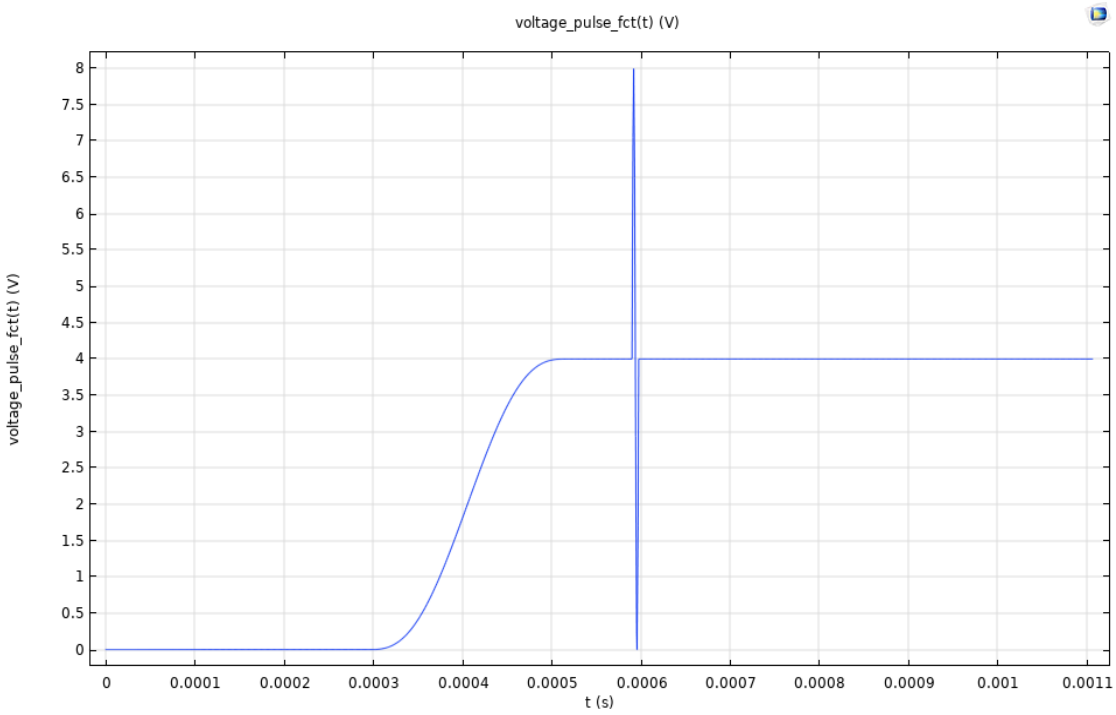

Figure 5.24: *Voltage function applied to the top electrode. As can be observed, the function has a initial ramp to apply the 4* V *DC voltage followed by a single sinusoidal pulse having frequency equal to the resonance one and amplitude to 4 V.*

Finally, some considerations concerning the damping coefficients must be done. In order to fit properly the vibration ring down and simulate the presence of the air or vacuum in the model, the viscosity coefficients have been added to each material layer constituting the device. These are computed by using the loss factor coefficient of each material layer provided by the company STMicroelectronics. Moreover, in case of air a thin-film damping condition is introduced at the interface between solid and fluid domain.

The results obtained for air and vacuum and their comparison with the experimental ones are shown in the following chapter.

5.7 Cross-talk experimental analysis

In this section an introduction to the Cross-talk phenomena and to the experimental campaign aimed at measuring its intensity is proposed. The device is composed from 16 membranes and their behaviour may change due to mutual interactions. In particular, the presence of this unwanted interaction shows its evidence in two way: the first one concerns the displacement and the second the frequency of oscillation. As will be shown throughout the thesis, when a membrane is activated by means of a voltage application also their first neighbors experience a small vibration. The second evidence of the cross-talk's presence is visible in the frequency response of the membrane. It must be said that the 16 membranes within the die are not

completely equal to each others: due to the variability in the fabrication process they can differ in term of geometry (i.e. diameter of the cavity and thickness of each layer) and so in turn they have a slightly different resonance frequency. These differences in frequency can cause a distortion in the frequency peak in correspondence of the first vibration mode. Basically, instead of seeing a single peak at the own resonance frequency of the membrane under investigation, other secondary peaks appear at values of frequency corresponding to the resonance frequency of the closest membranes.

Starting from the investigation of the displacement of the membranes close to the activated one, the analysis is performed with the following approach. The device can be divided into four quadrant and each of these contains 4 membranes (Fig.**??**). It has been chosen to activate the central membrane and measure the displacement of the all four membrane belonging to the quadrant by using Polytec in LDV mode (same set up of the previour section 5.6.1). Each central membrane is activated individually and the investigation of the quadrant is carried out. Once a complete quadrant is measured, the analysis moves on to the next. It is important to stress that the 4 central membranes are not activated at the same time.

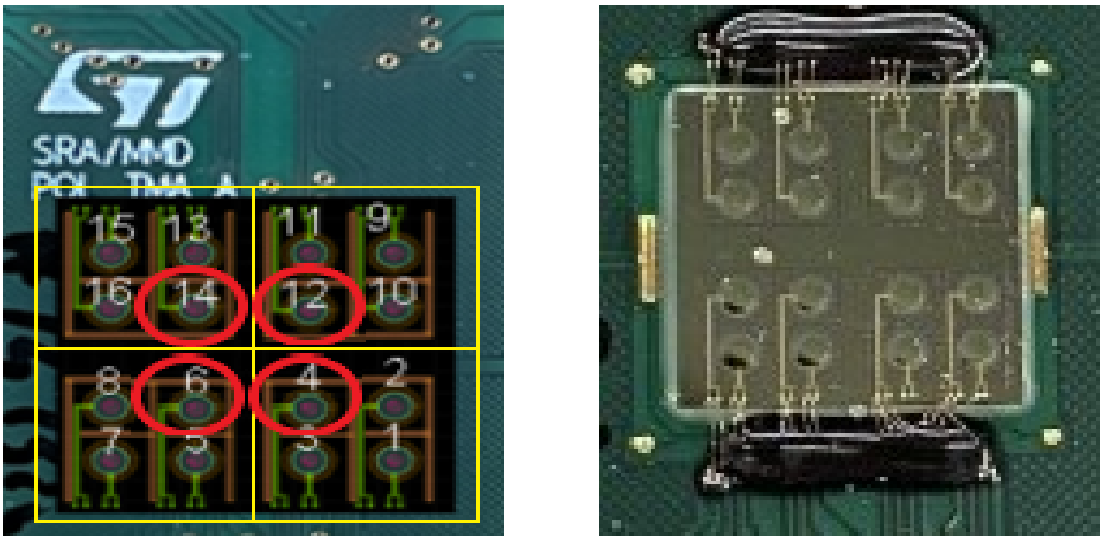

(a) *(b)*

Figure 5.25: *a) Graphic database System (GDS) of the device. In the figure it is possible to observe the numbering of the membranes, the division into quadrant (yellow squares) and the activated central membranes (red circle). b) Photograph of the die*

The measurements are performed on 2 complete die and so on a total of 8 quadrants. Moreover, in order to split the acoustic and mechanical damping contribution and investigate their intensity and influence, the analysis is carried out both in air and in vacuum (-10^5Pa).

As regard the distortion of the frequency peak due to the cross-talk presence, the chirp analysis (see section 5.5.1) is performed in the frequency interval (110,180) kHz including the value corresponding to the first vibration mode. Also in this case the measurements is performed both in air and in vacuum.

All the experimental results obtained and their critical interpretation will be proposed in the next chapter.

5.8 Radiation pattern of the acoustic field and sound pressure

The last investigation of this master thesis is related to the acoustic characterization. The main aims of this analysis are to investigate and compute the intensity of the ultrasound perturbation and its directionality. The intensity value can be computed by measuring the pressure values over time in a point within the fluid domain at a fixed distance from the device. On the other hand, the directions of propagation are investigated by means of the radiation pattern: for a fixed plane it is possible to evaluate the intensity corresponding to each angle and so determine the preferential directions. Similarly to all thesis activity, a comparison between experimental evidences and simulation results will be proposed and so the the variables involved must be as consistent as possible.

5.8.1 Experimental characterization

The experimental characterization of the acoustic field emitted by the membrane oscillation is performed by using a customized automated set-up. It is composed from a microphone Xarion ETA450 Ultra, a 4 degree of freedom (3 axis and 1 rotation) automated set-up on which the device is attached, an oscilloscope Tektronix MSO44 to read the output signal coming from the microphone and apply the desired driving voltage to the membrane. In Fig. 5.26, the equipment just introduced is shown.

The first measurement performed uses a driving voltage characterized by a 4V DC and a single sinusoidal pulse at the resonance frequency having amplitude equal to 4V. Once the pilot voltage is defined, it is worth to point out where the acoustic measurements are done. In this analysis, it is chosen to measure the sound pressure over time in correspondence of the activated membrane's centre at $z = 2$cm. Basically the procedure is the following one: the z-axis arm places the device at 2cm from the microphone and subsequently a series of measurement in plane x-y are carried out to find the right alignment with the membrane. The perfect alignment between activated membrane's centre and microphone corresponds with the maximum pressure intensity. For the sake of clarity, it is key to previously verify the parallelism between the device and microphone surface.

The second experimental campaign is aimed at computing the radiation pattern. Unlike the previous case, in this test the voltage, through which the membrane is activated, is a serie of sinusoidal pulses centered in 4V with amplitude equal to 4V. The measurement is performed both on top the membrane and below the cavity at distances equal to 6cm. Once the membrane under investigation and the microphone are positioned in front of each other at the desired distance, the rotation arm is exploited to rotate -90°/+90°. The microphone acquires the sound pressure for some angles within the interval (the higher is the number, the better is the resolution) and then a customized software gives as a result the pattern of the radiation.

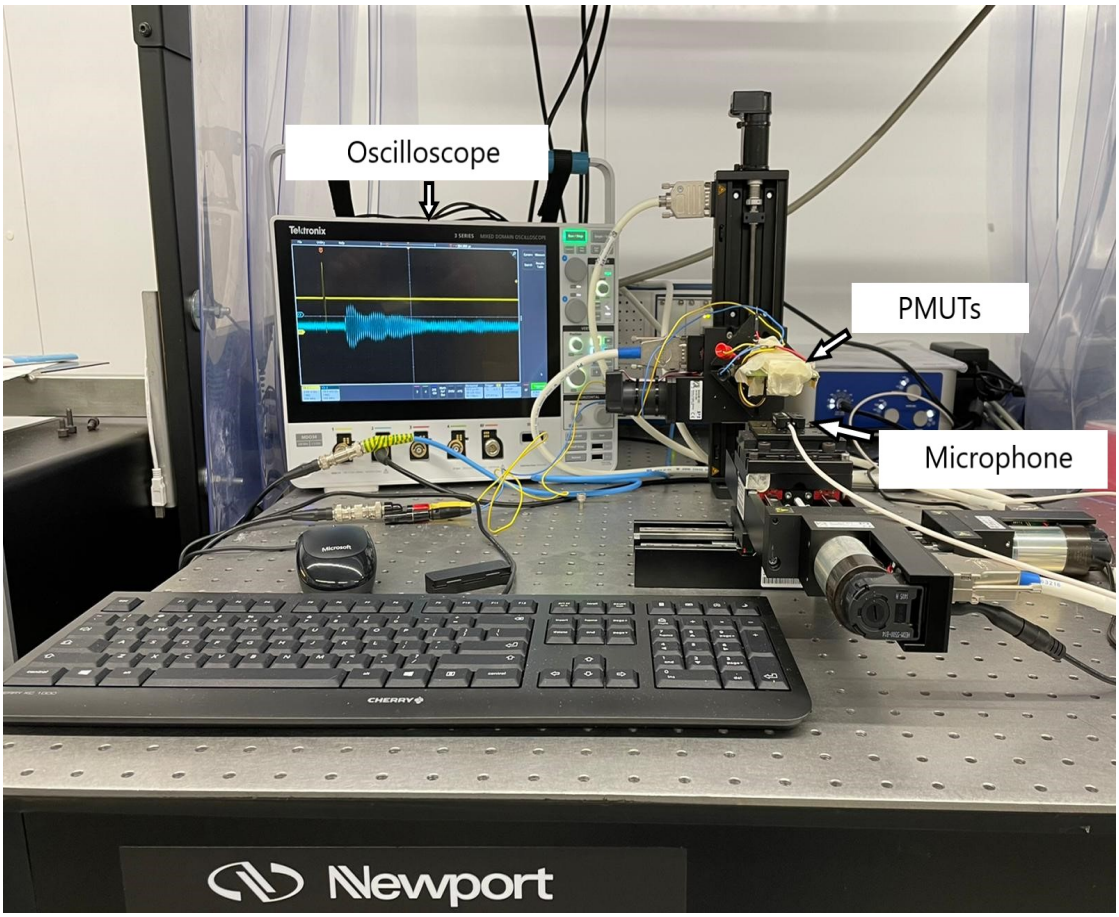

Figure 5.26: *Schematic representation of the physical set-up to perform the acoustic characterization.*

5.8.2 Simulation modelling

The modelling of the acoustic field is performed by using two different models: the 3D model whole device already introduced in Section 5.6.2 and a 2D axisymmetric model single membrane. In the first case, the results obtained in the previous study with a driving voltage single pulse equal to 4DC and 4AC are taken into account. Instead of analysing the vibration of the membrane, the attention is paid to the acoustic domain: by positioning in a point of the fluid domain or by defining a meridian plane is possible to measure the variation of pressure over the time. It is worth to remember that in this model a time dependent study was performed. In Fig.5.27 the selected point at which the sound pressure will be calculated is shown.

In order to obtain the radiation pattern and information related to the direction of propagation a 2D asisymmetric model is used. It is quite similar to that described in section (5.3.2). Unlike to the previous, this one contains a spherical fluid domain all around the solid domain having radius equal to 24cm (being a 2D model it is not a problem use a bigger domain). As usual in acoustic domain, the meshing and in particular the maximum size is determined by considering the wavelength of the ultrasound perturbation: it is equal to the $\frac{\lambda}{6}$.

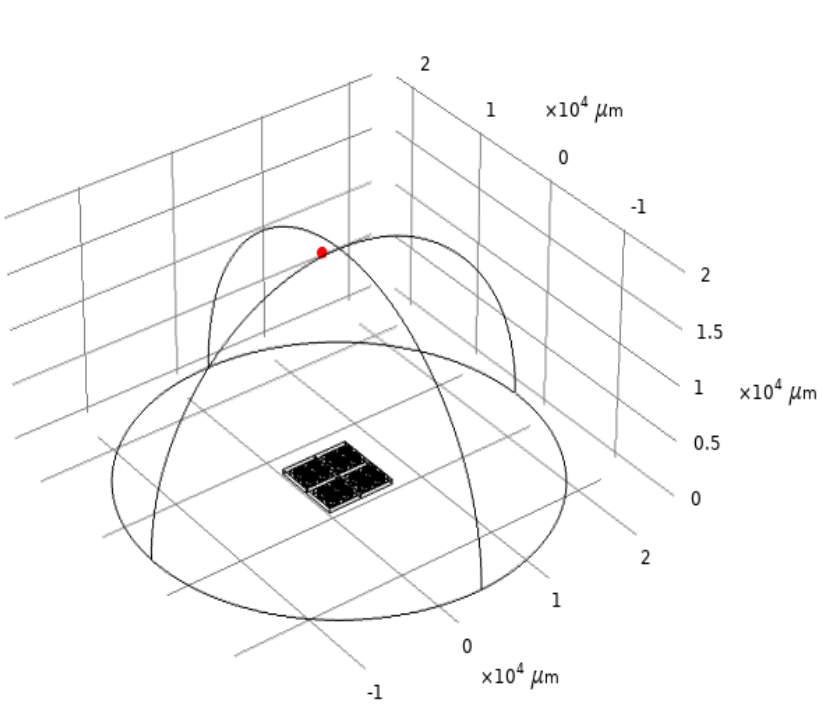

Figure 5.27: *Representation of the point at which the pressure will be measured. The point is placed at* $z = 2$cm *over the activated membrane.*

Moreover, another difference with respect to the previous model concerns the boundary condition of the external surface. In this one, it is chosen not to apply the spherical wave radiation onto the external surface but to add a Perfectly Match Layer (PML). This is preferred because the addition of a further domain does not affect too negatively the computational time (2D model necessities much lower than 3D ones). Even changing the conditions the result remains exactly the same: no acoustic waves will be reflected. The fluid domain, PML and their mesh are shown in Fig.5.28. Concerning the actuation, the driving voltage applied to the electrode is the following: 4V DC voltage and an continuous harmonic perturbation with amplitude equal to 4V.

The last comment to this model concerns the study performed. It is chosen to carry out a pre-stressed frequency analysis in the interval ranging from 120kHz to 160kHz with step equal to 250 Hz.

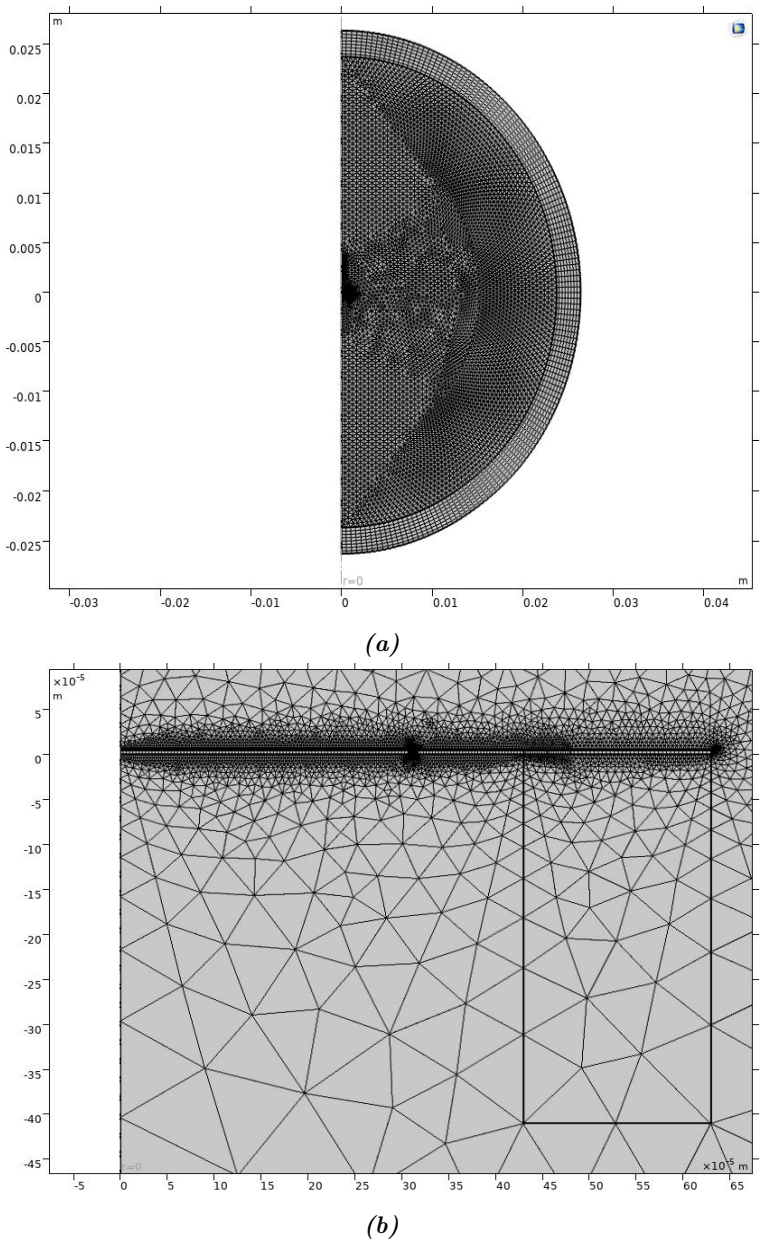

Figure 5.28: *Geometry and meshing of the 2D axysimmetric model with the fluid domain. a) Complete view of the model. The external layer of the fluid domain is the so called PML. The best way to mesh it is to use a mapped quadratic shape. b) Detail of the solid domain within the fluid.*

Chapter 6

Results

This chapter is aimed at showing all the obtained results. For each investigations a comparison between the experimental and simulation results is proposed and a critical discussion is done. In such a way it is possible to get closer as much as possible to the reality and point out where to improve and plan future developments.

6.1 Static deformation of the membrane

The first analysis concerns the static deformation of the membrane. Starting from the experimental evidences, a typical topography measurements gives as a results an image like the one shown in Fig.6.1. By using the software integrated in Polytec, it is possible to post-process the results and obtain the desired information.

First of all, a cutting plane must be defined in the topography 3D image and then positioned in correspondence of the membrane's centre under investigation. By doing so, a profilometry of the device surface is obtained. Once the profile is defined, the reference points from which the height difference Δz will be measured shall be selected. As shown in the bottom part of the Fig.6.1, the first reference point is of course the centre of the membrane and the second is a fixed point equal for all the membranes. In this investigation a point close to the connection lines is selected. The reason is quite simple and it is related to the fixed position of the Copper lines. If the relative distance between the selected point and the conduction lines is equal for all measurements so in turn even the selected point is coherent for all the membranes.

The main objectives are to define the average displacement of the centre of the membranes in static regime (DC voltage equal to 0 V) and then compute its variation as a function of the DC voltage applied. In particular these voltage values have been chosen: 5, 10, 15 and 20 V. The measurements is performed on an entire die and so in turn a total of 16 membranes. In the following part of the section experimental and simulation results are proposed. The table 6.1 resumes the experimental static displacements of all the membranes within a die while Fig. 6.2 shows the variation as a function of the voltage applied. On the other hand, in Fig. 6.3 and 6.4 appear the results obtained with the 2D and 3D models. Lastly a summary table with all the result is shown (Table 6.2).

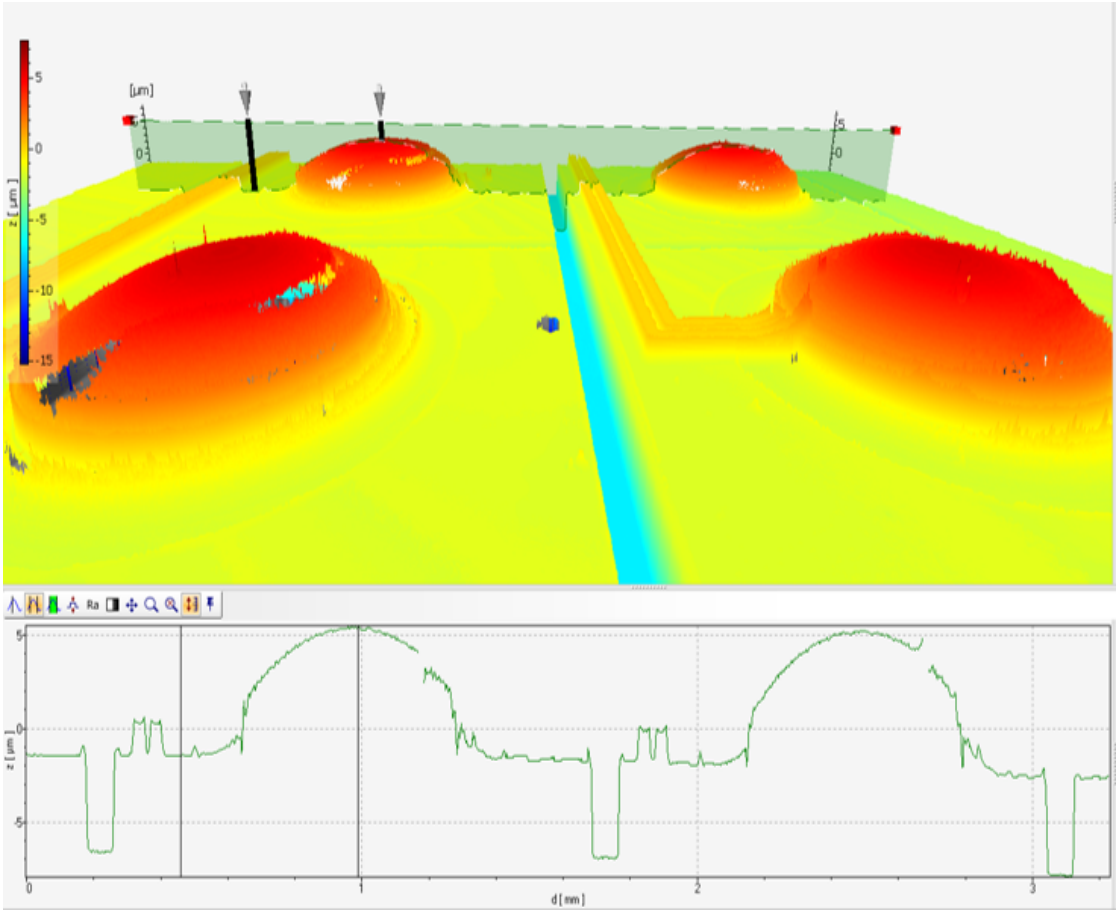

Figure 6.1: *Example of the topographic image obtained through Polytec. At the top you can observe the plane passing through the center of the membrane and at the bottom the profile obtained with the reference points.*

Membrane	**Δz [µm]**	**Membrane**	**Δz [µm]**
1	7.37	9	7.32
2	7.26	10	7.18
3	6.7	11	6.61
4	7.12	12	7.21
5	6.68	13	6.85
6	7.03	14	6.91
7	7.22	15	7.04
8	7.49	16	6.76
Average	7.04	STD	0.27

Table 6.1: *Experimental static displacement (0 DC voltage) of the centre of the 16 membranes within a die. The average value and the standard deviation are respectively equal to 7.04* µm *and 0.27.*

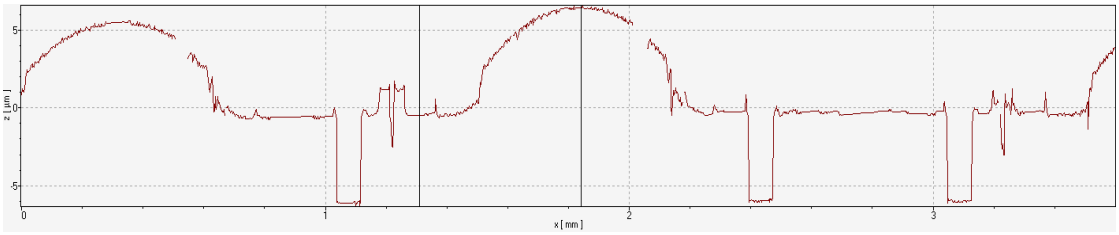

(a)

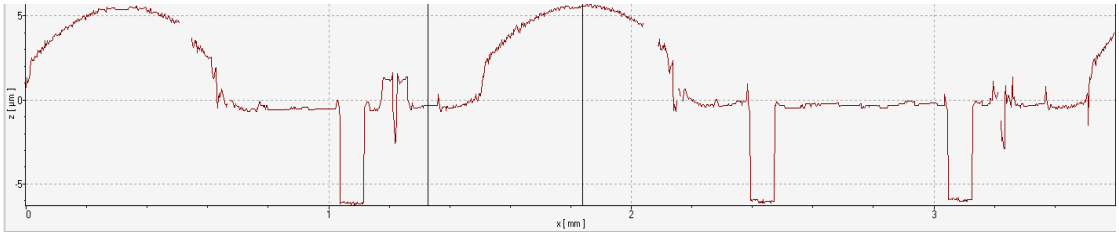

(b)

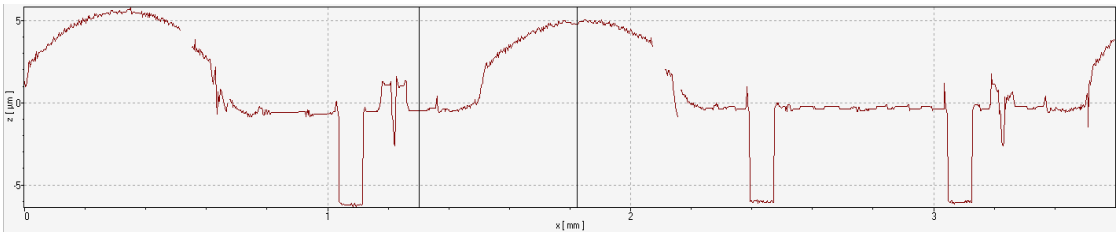

(c)

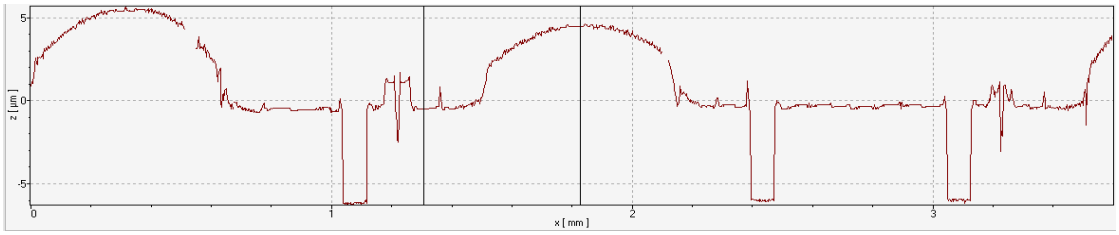

(d)

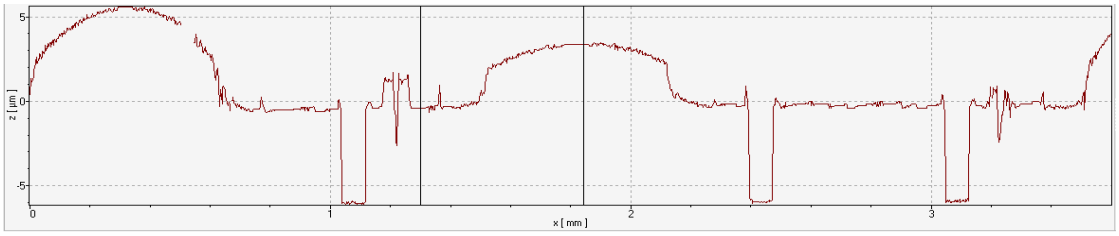

(e)

Figure 6.2: *Profile of the membrane as a function of the DC voltage applied. a) OV; b) 5V; c) 10V; d) 15V; e) 20V. It is easy to see how the centre lowers as the voltage increases and it is due to the creation of tensile stresses as a consequence of the piezoelectric effect. The average displacements are the following:* **7.04** µm *at 0V,* **5.9** µm *at 5V,* **5.15** µm *at 10V,* **4.85** µm *at 15V and* **3.77** µm *at 20V. The deviation standard is equal respectively to 0.31, 0.33, 0.27 and 0.35.*

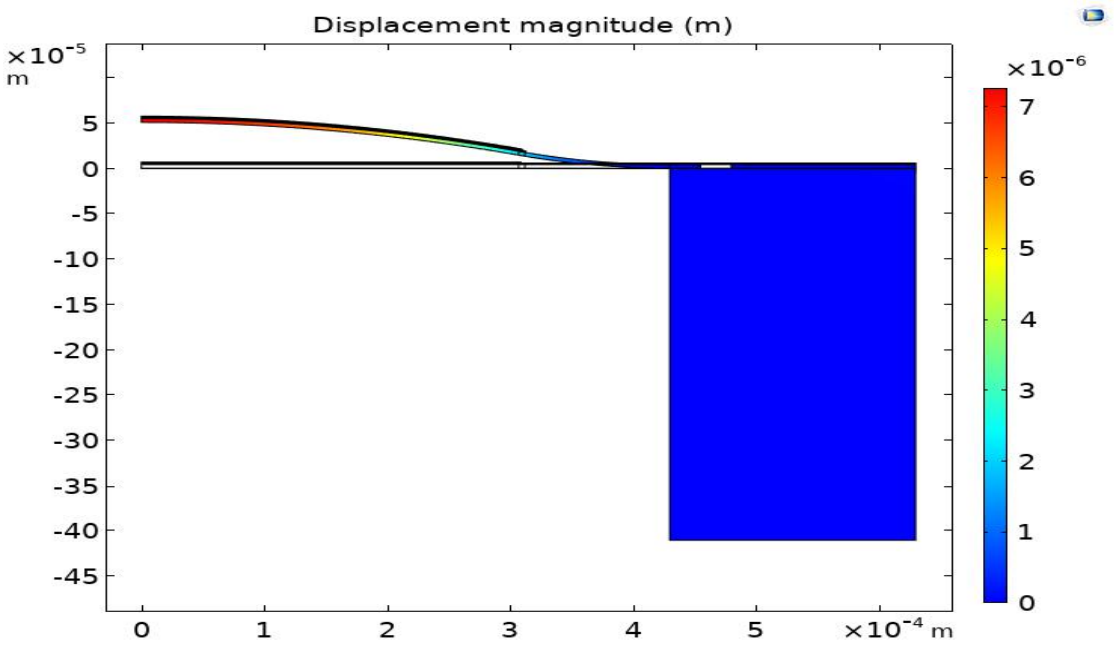

(a)

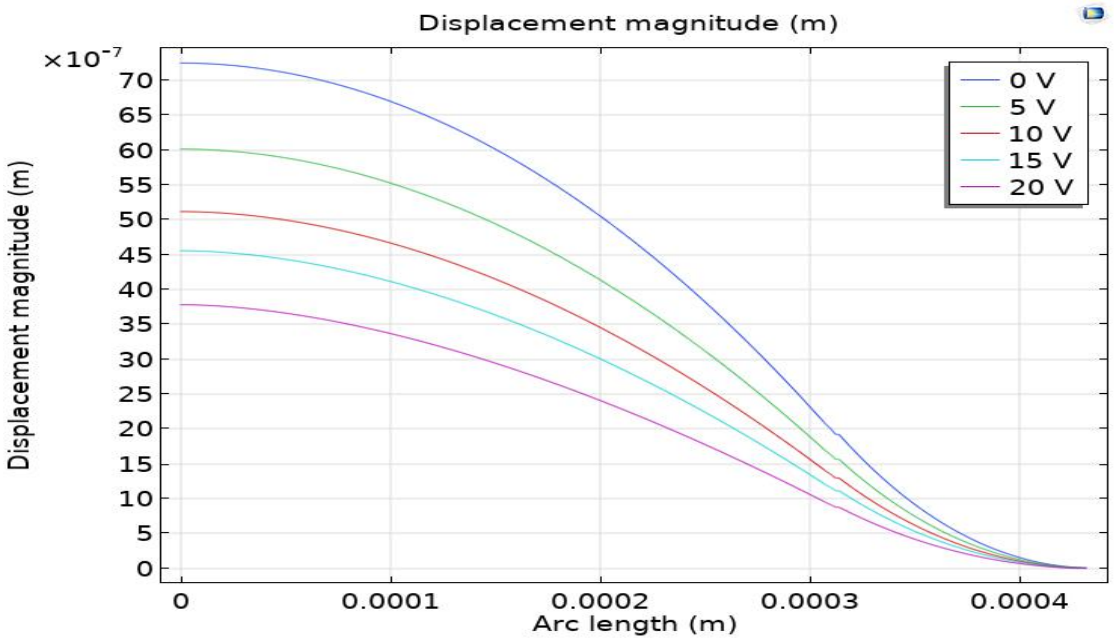

(b)

Figure 6.3: *a) Static deformation of the 2D membrane due to the residual stresses (DC voltage equal to 0V). b) Line graph of the membrane profile as a function of the DC voltage applied. The results fit properly the experimental evidences.*

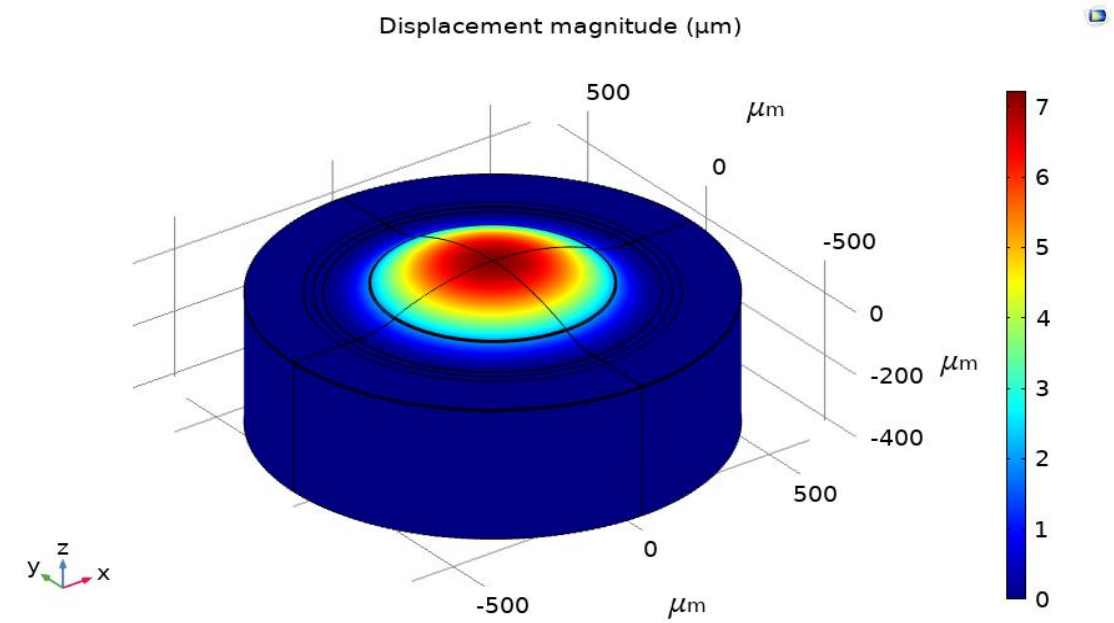

(a)

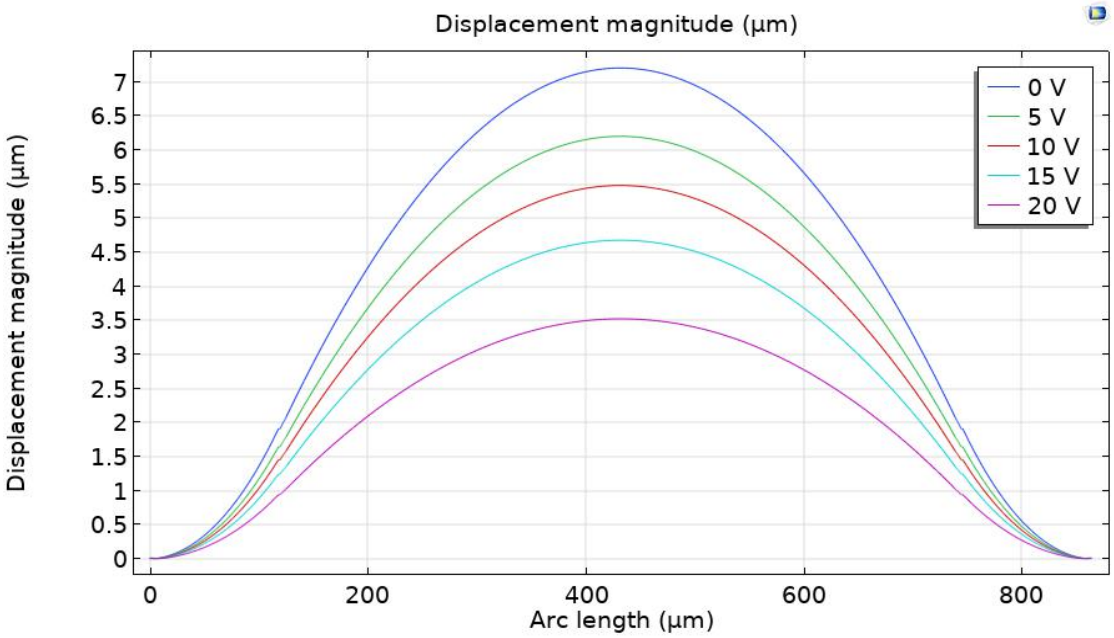

(b)

Figure 6.4: *a) Static deformation of the 3D membrane due to the residual stresses (DC voltage equal to 0V). b) Line graph of the membrane profile as a function of the DC voltage applied. Also in this case there is a good match between experimental and simulation results.*

Δz centre [µm]			
DC Voltage [V]	Experimental	Simulation 2D	Simulation 3D
0	7.04	7.25	7.21
5	5.9	6.03	6.23
10	5.15	5.17	5.5
15	4.85	4.55	4.72
20	3.77	3.75	3.54

Table 6.2: *Summary table: deformation of the membrane*

6.2 Static deformation of the whole die

In this section, the results in terms of radius of curvature (ROC) and Δz between some characteristic points of the die are shown.

Starting from the experimental ones, in Fig.6.5 an example of profilometry image to compute the ROC is proposed.

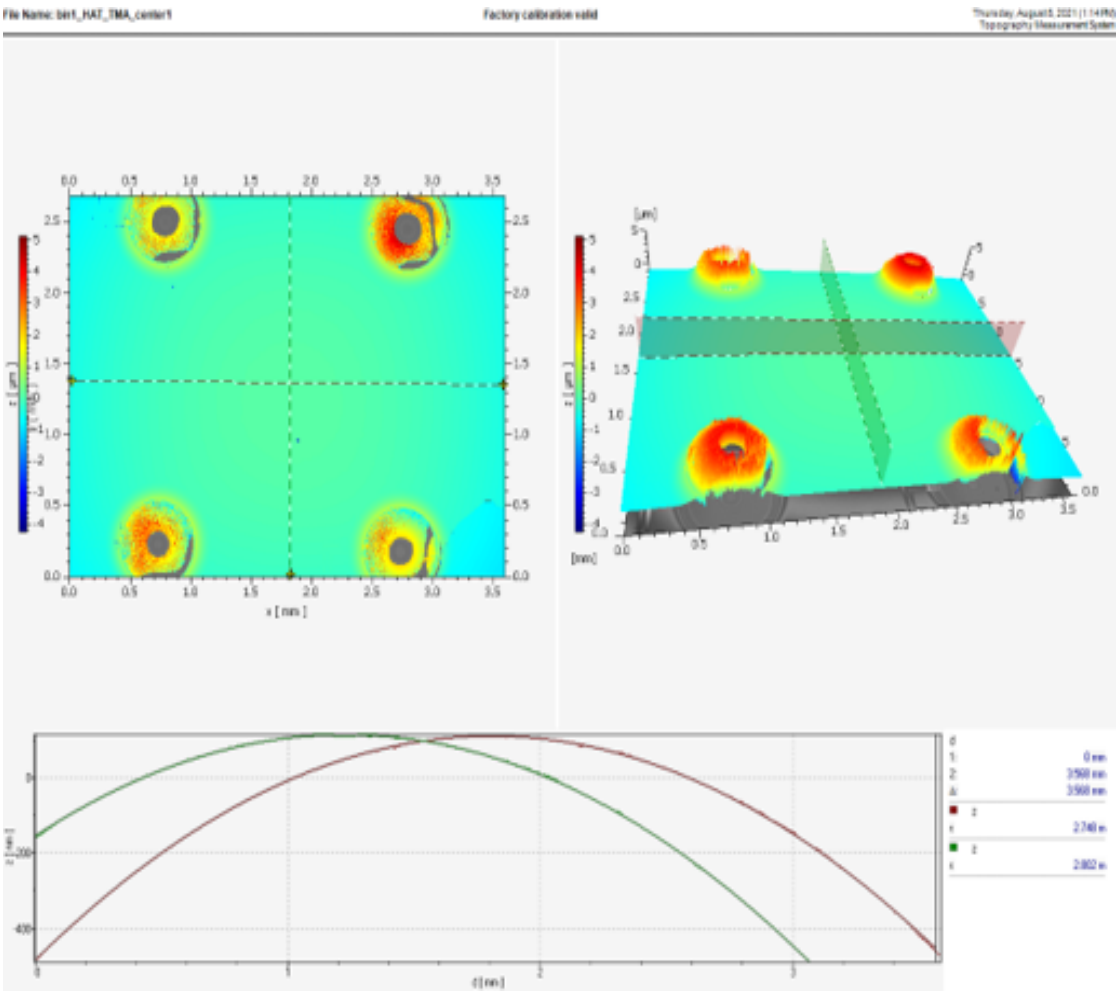

Figure 6.5: *Experimental image obtained with Polytec.*

Once the surface's topography of the die is obtained, the Polytec software allows to measure the radius of curvature by defining two planes along x and y axis. It is important to point out that these planes must intersect each other at the centre of the die.

The values of ROC are computed by the software using the following relation:

$$ROC = \frac{4 \cdot H^2 + D^2}{8 \cdot H} \tag{6.1}$$

where H is the height in z direction and D the length of the plane on which the ROC is measured.

The measurements has been performed on 15 dice and the values are resumed in Table 6.3.

DIE	ROC(x) [m]	ROC(y) [m]
1	4.4	3.7
2	3.04	2.79
3	3.11	2.79
4	3.33	3.27
5	2.89	2.07
6	3.23	2.45
7	3.30	2.83
8	3.03	2.95
9	2.76	2.33
10	3.47	2.61
11	2.96	3.01
12	2.53	1.96
13	3.51	2.03
14	2.75	2.83
15	2.48	3.12
Average	**3.11**	**2.72**
Stand. Dev.	0.47	0.49

Table 6.3: *Experimental radius of curvature along x and y axis. It is worth to point out how there is a quite high dispersion of the results; Indeed the curvature of the die is strictly related to the variability of the fabrication process and the position of the die on the wafer. Moreover, also the amount of glue used to attach the die on the TMA board can affect the result and this viarible is quite difficult to control.*

The second investigation aimed at determining the die deformed configuration is related to the Δz between some characteristic points. In Fig.6.6 a schematic image of these point is shown.

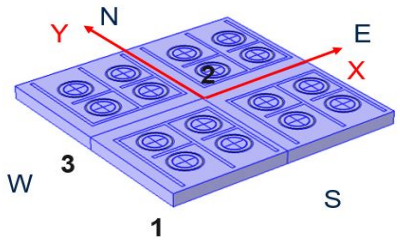

Figure 6.6: *Image of the die. The attention will be paid to the Δz between 1-2, 1-3 and 2-3.*

The experimental profilometry to investigate these characteristic points is the one shown in Fig.6.7.

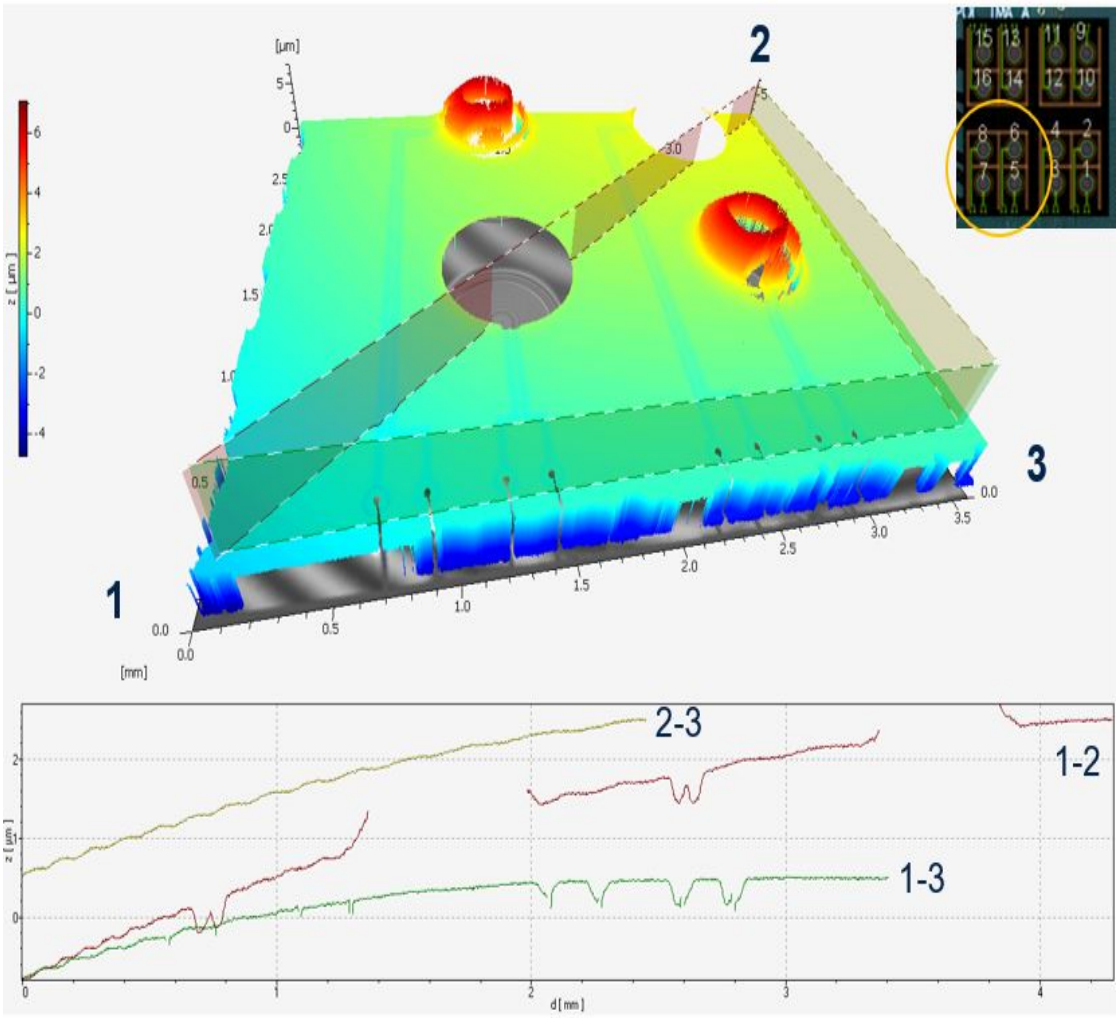

Figure 6.7: *Topography of the die's corner. The aim is to measure the difference in z between the different points.*

For the sake of clarity it is important to highlight how the analysis is performed. The three point 1, 2 and 3 are respectively the four corners, the unique centre and the four edge's centre and so for a single die it is possible to compute four Δz_{12}, four Δz_{23} and eight Δz_{13}. The measurements is done on four dice and an average value for the three parameters is proposed.

The results obtained are the following one: $\Delta z_{12} = \mathbf{3.57}$µm, $\Delta z_{13} = \mathbf{1.62}$µm and the last $\Delta z_{12} = \mathbf{2.04}$µm

Moving toward the simulation results, the height profile along x and y at the centre of the die (Fig.6.8a) and the edges' profile (Fig.6.8b) are shown.

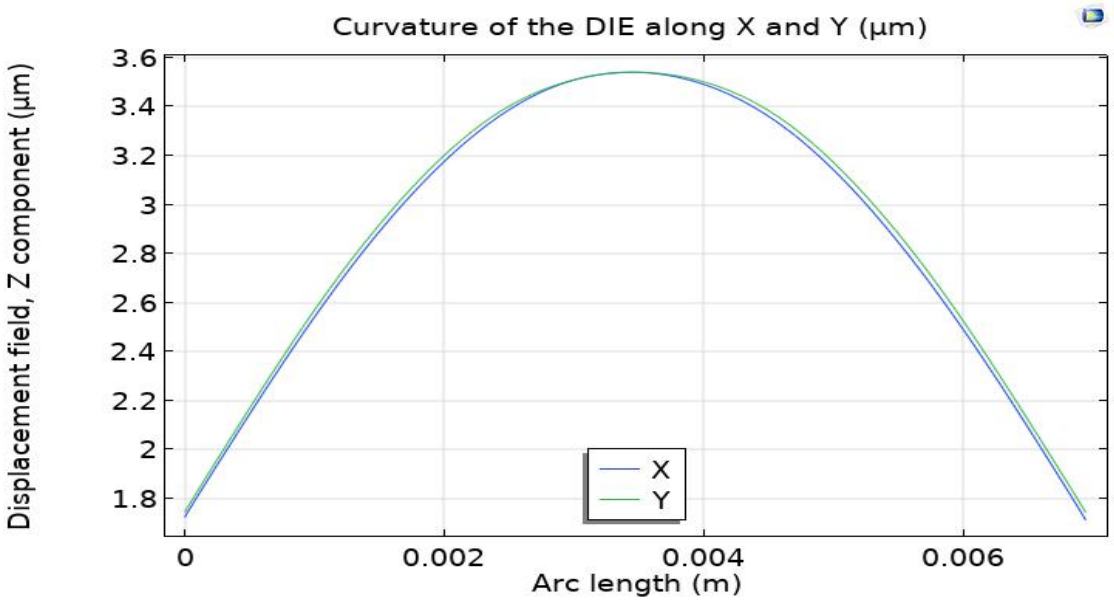

(a)

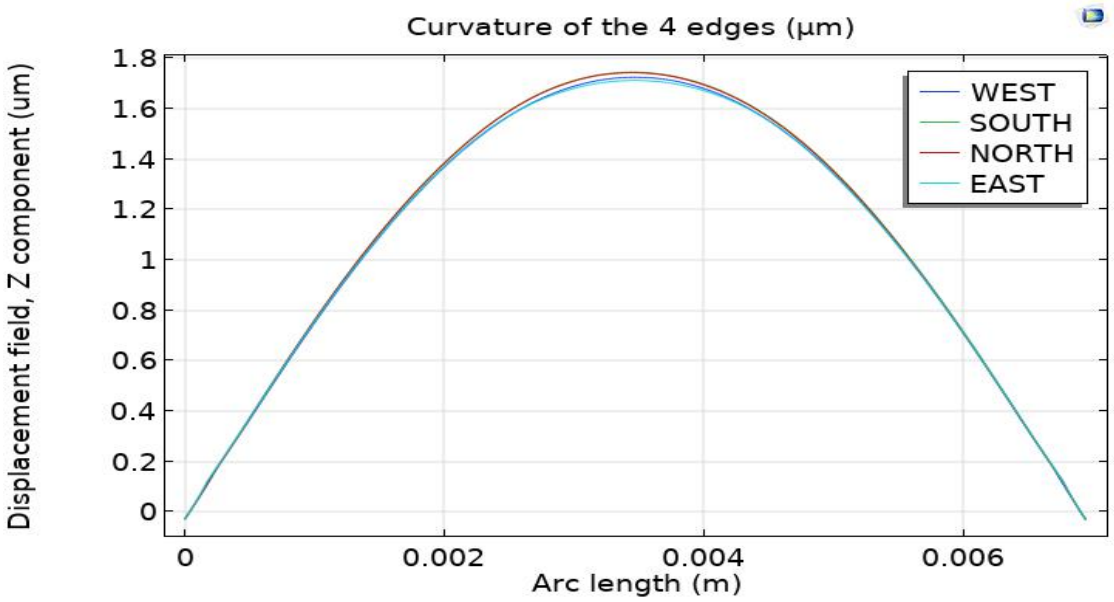

(b)

Figure 6.8: *a) Displacement profile in z direction of the x and y axis passers-by through the center. The difference between the centre at 3.5* µm *and the two extremes at 1.73* µm *represents the previous parameter* Δz_{23} *b) Displacement profile in z direction of the four edges. In this case the difference between the centre of the profile and the extremes is the paramente* Δz_{13}.

As regards the simulation results obtained, they are the following one: Δz_{12} = **3.53**µm, Δz_{13} = **1.71**µm, Δz_{12} = **1.86**µm, ROC(x) = **3***m* and ROC(y) = **3***m*. In Fig.6.9 the 3D die deformation is shown followed by a summary table 6.4.

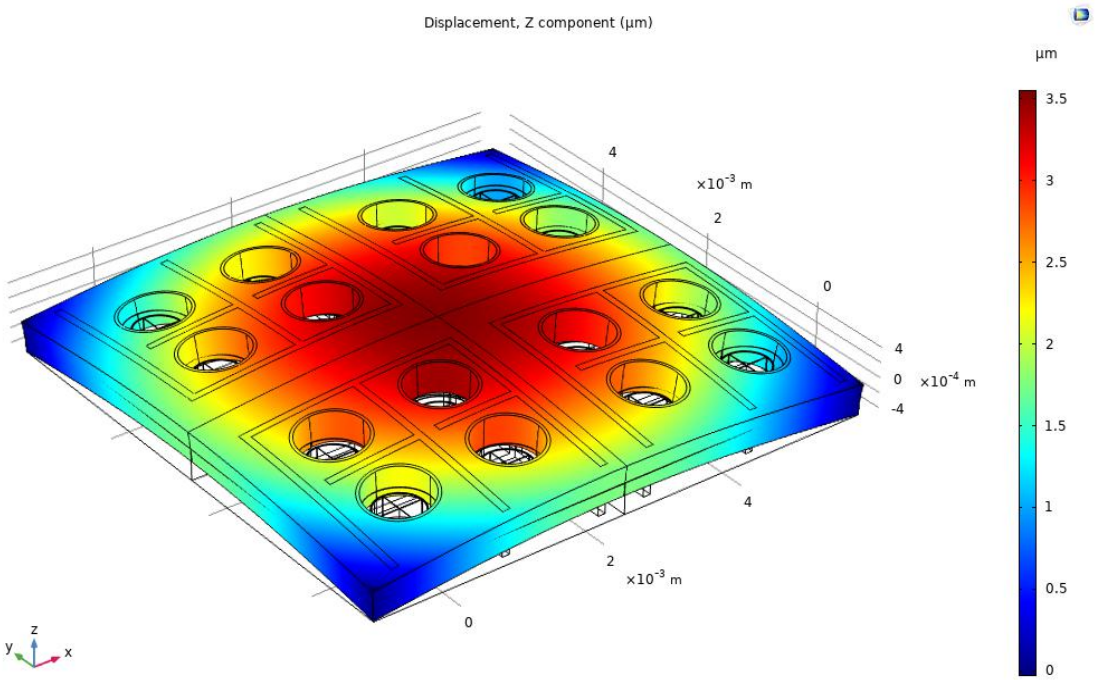

Figure 6.9: *Die deformation obtained by means of COMSOL simulation.*

	Exper.	Simul.
ROC(x) [m]	3.11	3
ROC(y) [m]	2.72	3
Δz_{12}[µm]	3.57	3.53
Δz_{13}[µm]	1.62	1.71
Δz_{23}[µm]	2.04	1.86

Table 6.4: *Summary table: die deformation.*

6.3 Resonance frequencies of the membrane

This section concerns the frequency analysis of the first six vibration modes. The resonance frequency's values and the typical vibration configurations will be shown. Moreover, the attention will be focused on the variation of the resonance frequency by changing the DC voltage applied in the interval (0,20V) with step equal to 2V. First of all, the experimental and simulation (2D and 3D) frequency spectres with DC voltage equal to 2V are shown in Fig.6.10. This graphs are obtained by means of the pre-stressed frequency analysis and the attention is placed on the frequency values at each peak and not on the displacement value.

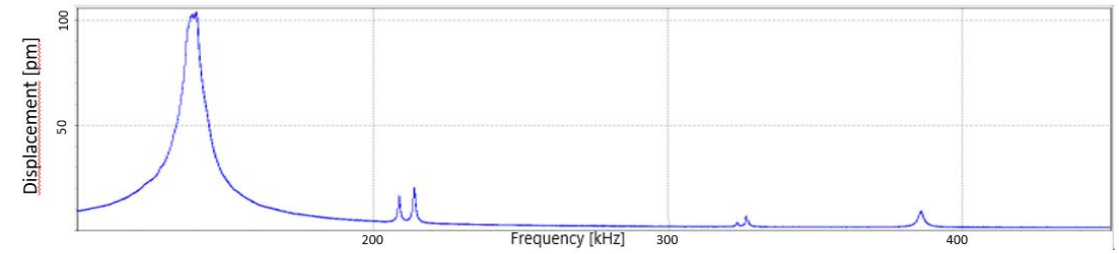

(a)

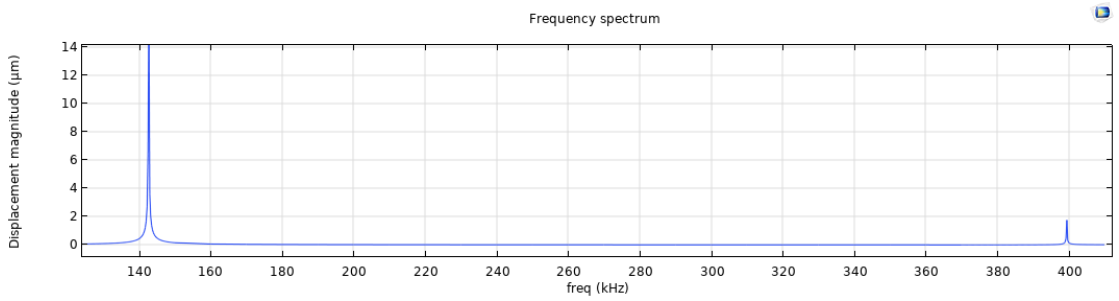

(b)

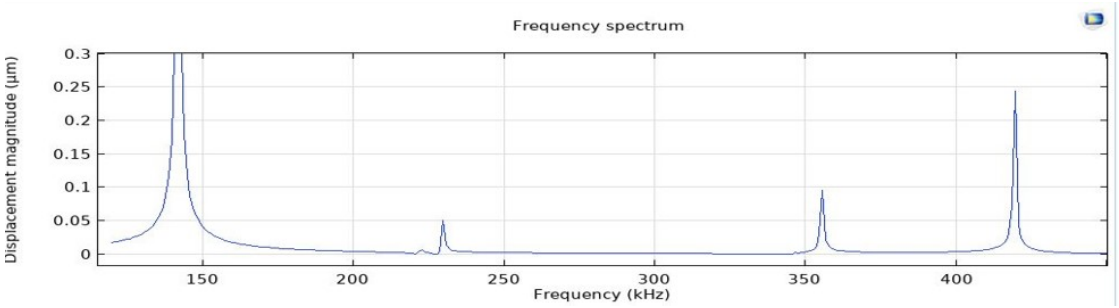

(c)

Figure 6.10: *Frequency spectrum obtained through the Chirp analysis with a DC voltage equal to 2V and harmonic perturbation with amplitude 0.1V. a) Experimental spectrum. b) Simulation spectrum obtained by using the 2D axisymmetric model. Looking at the graph, the 2d model is able to identify only the first and sixth way. It is due to intrinsic limit related to its geometry: only vibration modes with symmetry to the center can be identified. c) Simulated spectrum of the 3D model. Similarly to the experimental one, this model is able to detect all the six modes.*

Because of the limit of the 2D model, in the following part only the numerical values and

vibration mode of the 3D model will be compared to the experimental ones. Before leaving behind the 2D model, its vibration modes corresponding to the two peaks in the spectrum are shown in Fig.6.11.

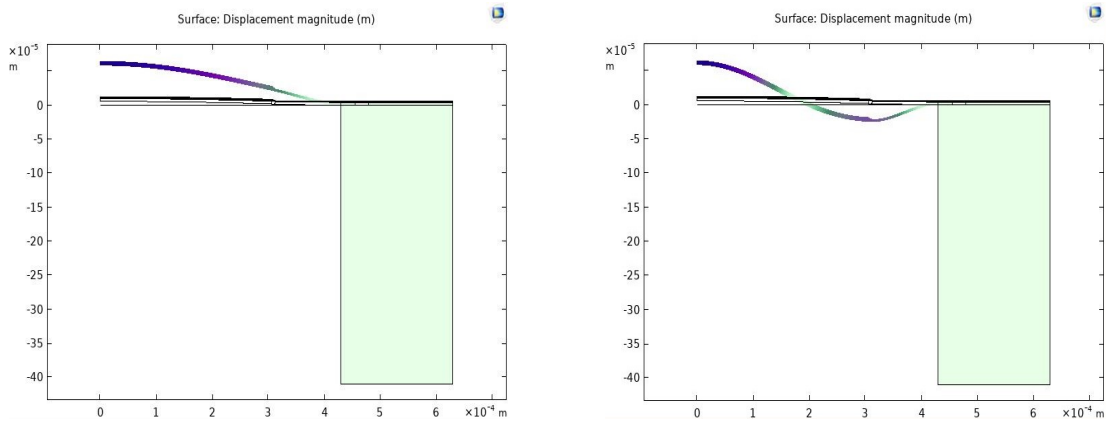

(a) ***(b)***

Figure 6.11: *Vibration mode of the 2D model. a) 1^{st} at 143* kHz*; b) 2^{nd} at 399.5* kHz*.*

Hereinafter the vibration modes are shown (Fig.6.12, 6.13) and the numerical values for each mode are resumed in graphs (Fig.6.14, 6.15, 6.16). The simulated values are the results of the pre-stressed Eigenfrequency study and the experimental ones are 5 different membranes (4,8,9,10 and 12) within the same die.

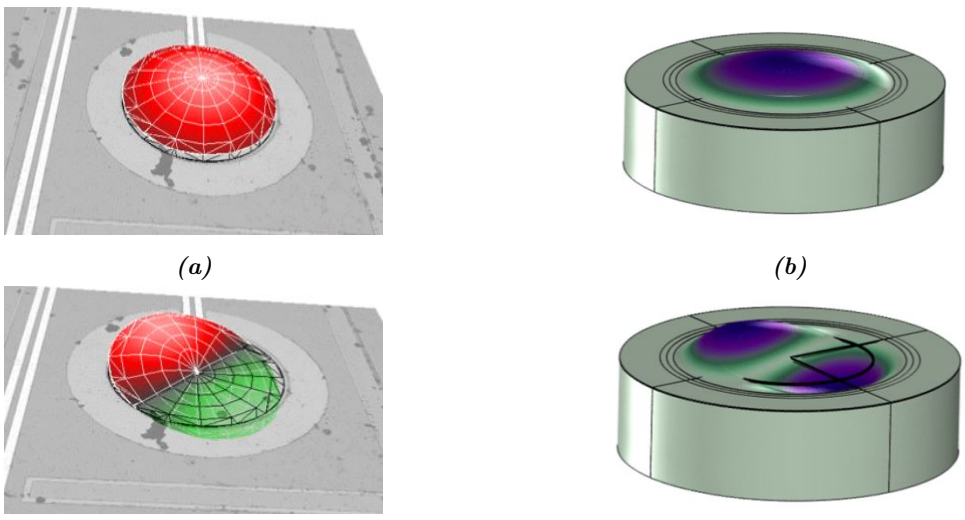

(a) ***(b)***

(c) ***(d)***

Figure 6.12: *a) Experimental 1^{st} mode. b) Simulation 1^{st} mode. c) Experimental 2^{nd} mode. d) Simulation 2^{nd} mode.*

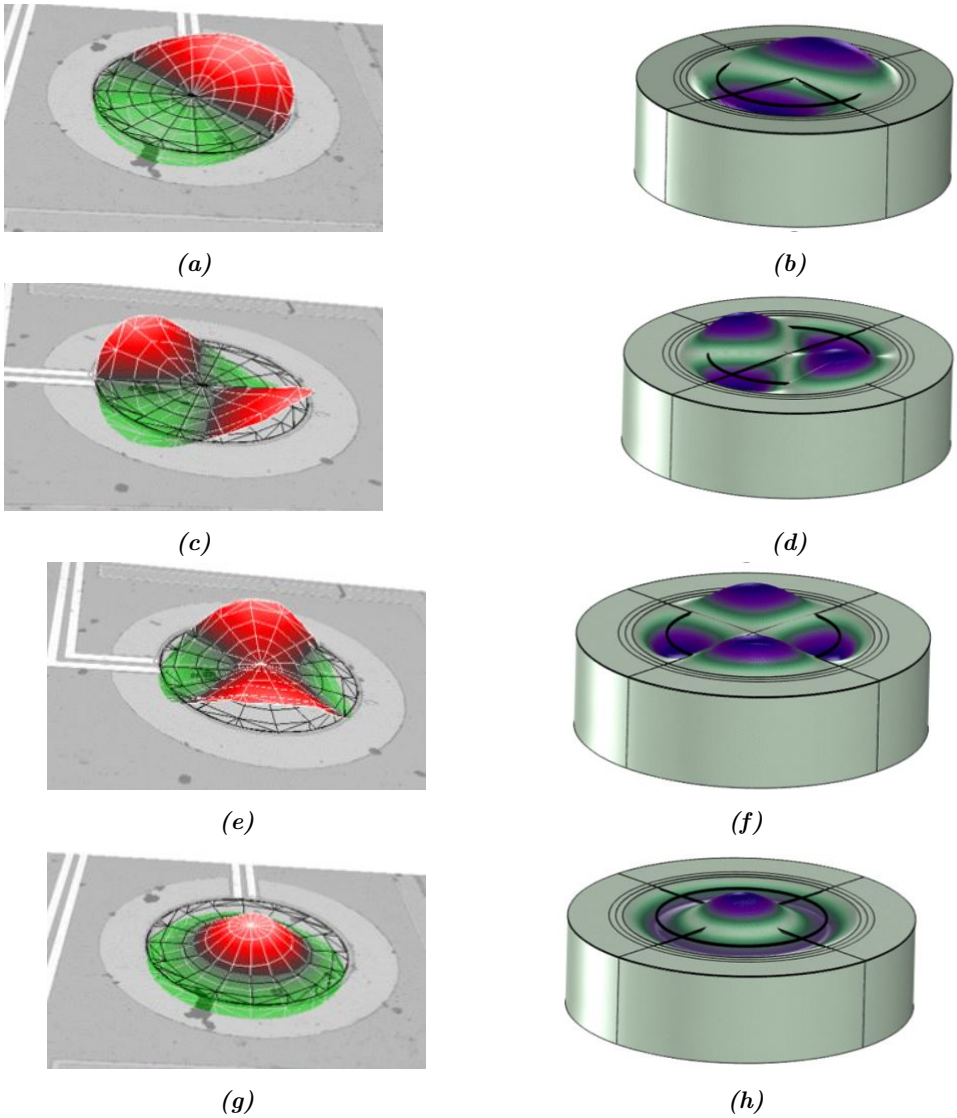

Figure 6.13: *a) Experimental 3^{rd} mode. b) Simulation 3^{rd} mode. c) Experimental 4^{th} mode. d) Simulation 4^{th} mode. e) Experimental 5^{th} mode. f) Simulation 5^{th} mode. g) Experimental 6^{th} mode. h) Simulation 6^{th} mode.*

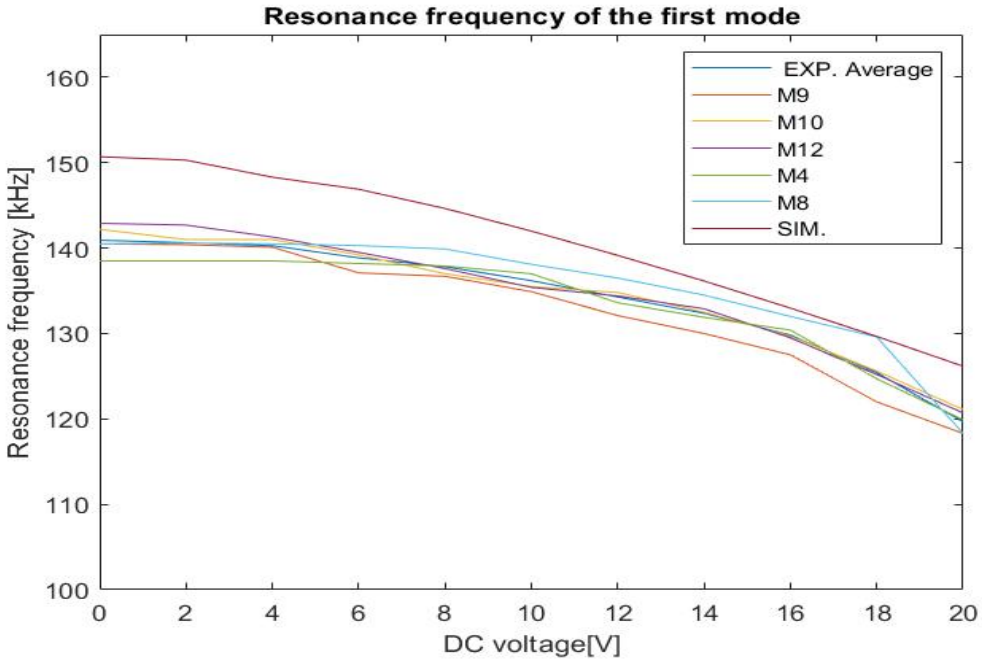

(a)

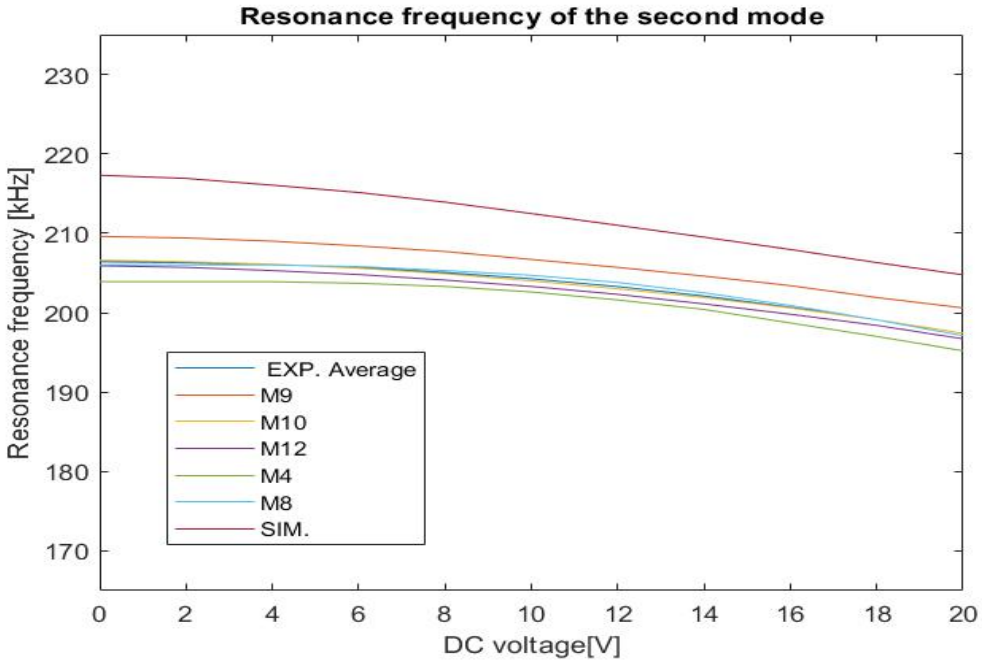

(b)

Figure 6.14: *Comparison between the experimental and simulated resonance frequencies as a function of the DC voltage applied.*

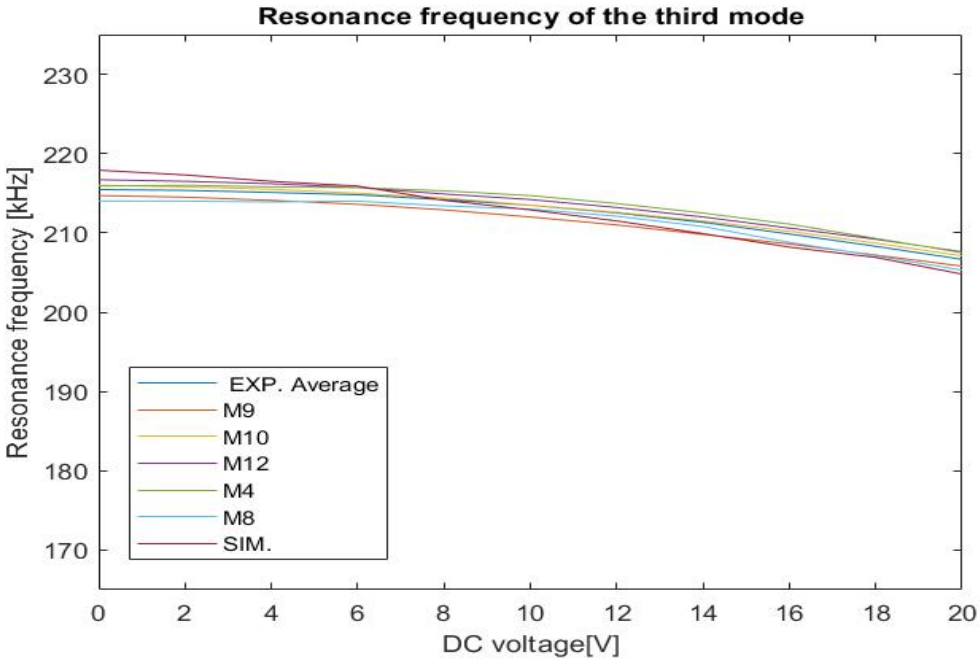

(a)

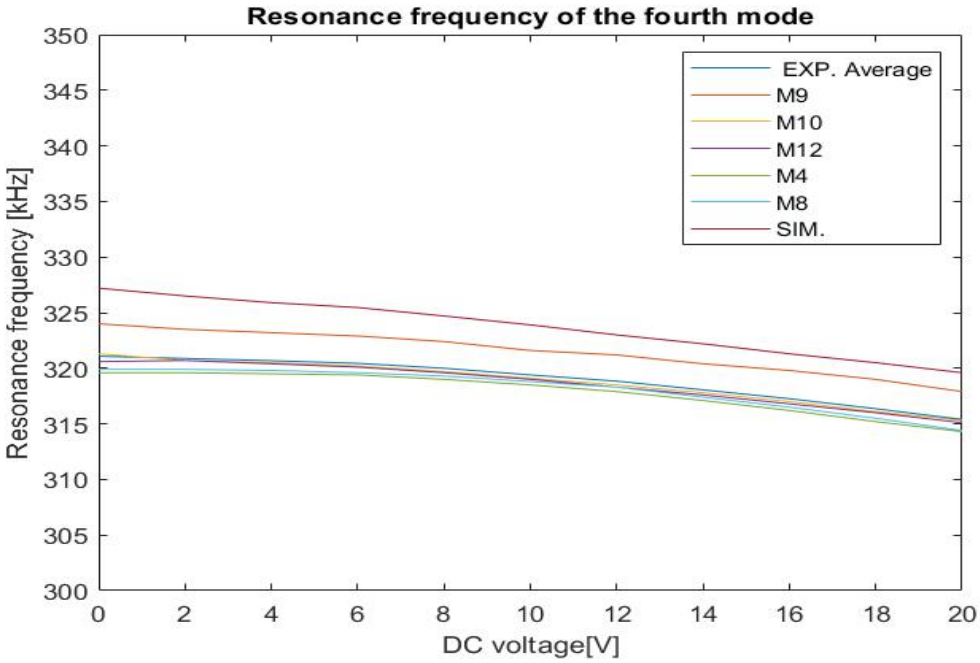

(b)

Figure 6.15: *Comparison between the experimental and simulated resonance frequencies as a function of the DC voltage applied.*

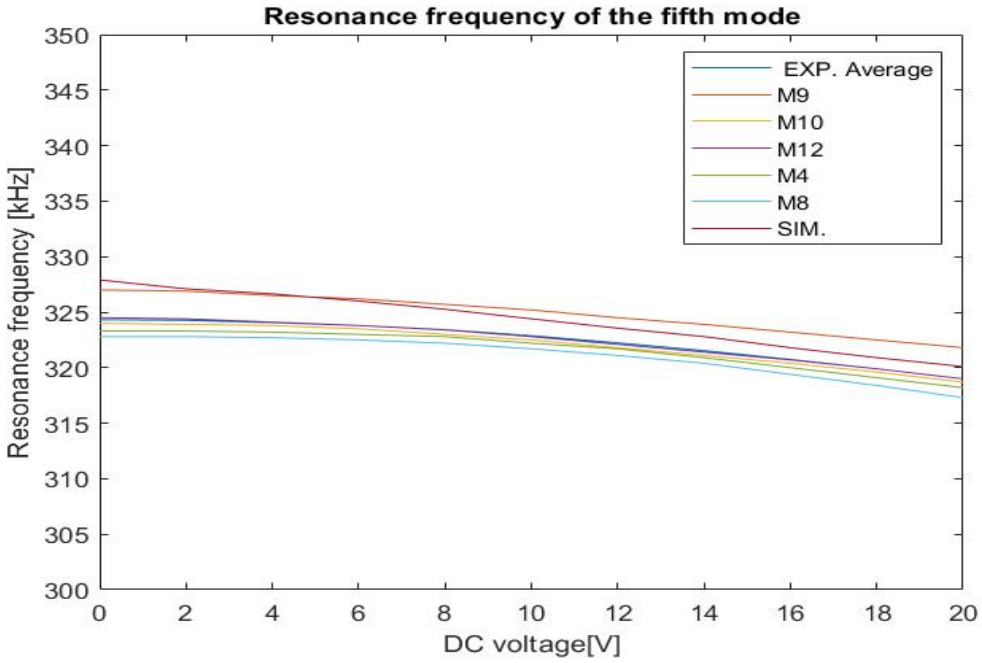

(a)

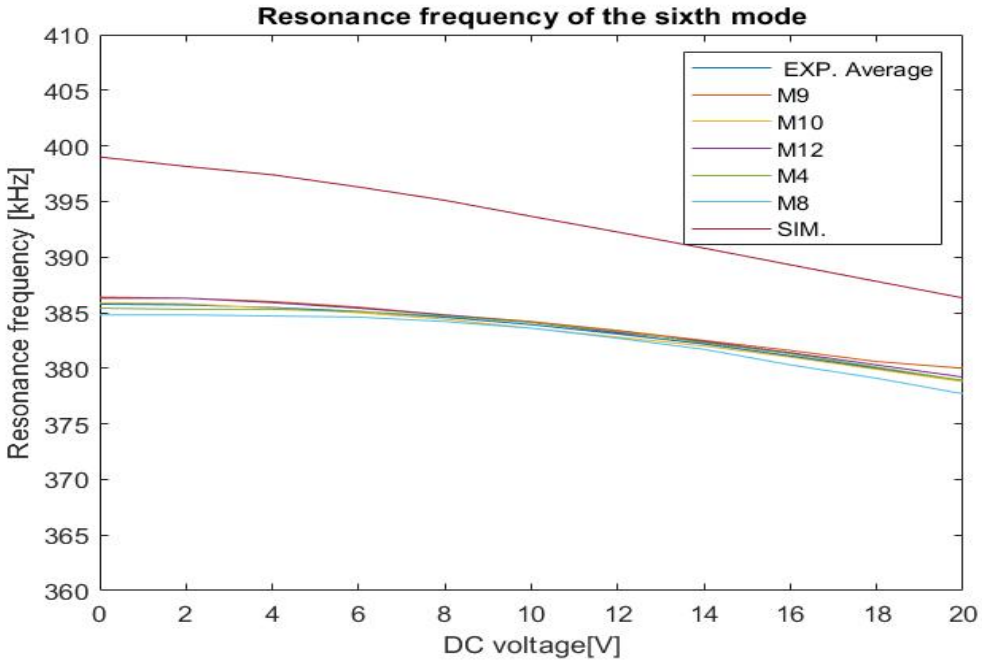

(b)

Figure 6.16: *Comparison between the experimental and simulated resonance frequencies as a function of the DC voltage applied.*

In the previous graphs, a good match between the experimental evidences and simulated ones is achieved. This is a good result that gives us positive feedback related to the properties parameters used in the model. The percentage error between the simulation and the average experimental values is proposed in Table 6.5.

ERROR[%]						
DC Voltage [V]	1^{st}	2^{nd}	3^{rd}	4^{th}	5^{th}	6^{th}
0	6	5	1	2	1	3
2	6	5	1	2	1	3
4	5	5	1	2	1	3
6	5	4	1	2	1	3
8	5	4	0	1	1	3
10	4	4	0	1	0	2
12	3	4	0	1	0	2
14	3	4	-1	1	0	2
16	2	3	-1	1	0	2
18	3	3	-1	1	0	2
20	5	4	-1	1	0	2

Table 6.5: *Summary table: Percentage error between simulation and experimental results.*

Considering the variability of the process, the results can be considered acceptable. Indeed, the fabrication process has a variability of many geometric and mechanical parameters such as diameter of the membranes and residual stresses around 10%. An error below this threshold is within the experimental dispersion. that limit is Moreover, the dispersion of the experimental results could be even greater if membranes belonging to other die were studied.

6.4 Oscillation ring down

The aim of this section is to show the time dependent results of the oscillation ring down. In the previous sections, the piezoelectric characteristics of the model have been well-proven in static regime: how the membrane responds to the application of a DC voltage. Here, in addition to the DC a single pulse AC voltage is applied and the vibration response investigated. The selected voltages are 4V DC and a single sinusoidal pulse centered in 4V with an amplitude ranging from 0.1 to 4V. As already introduced previously, the analysis are performed in air and vacuum: by analyzing the ring down of the oscillation the Q factor can be computed and so in turn the damping characterizing the device. In Fig.6.17 a comparison between the experimental and simulated oscillations of the membrane's centre is shown in the case of air and vacuum. For both situation the driving voltage is 4V DC and 4V AC. Looking at the figure, it is easy to understand how the presence of the air improves the damping phenomena experienced by the membrane.

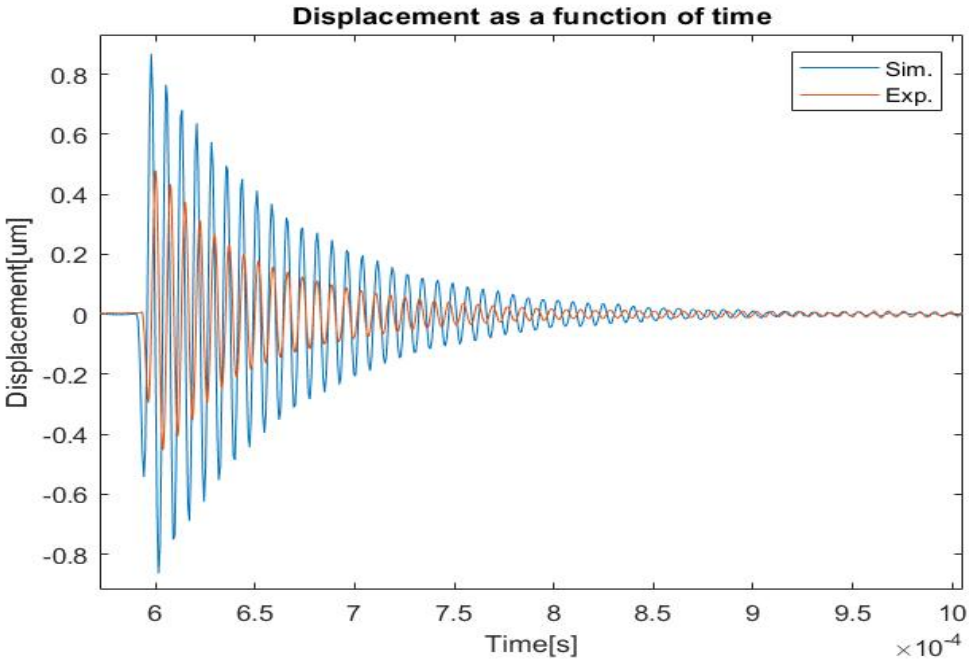

(a)

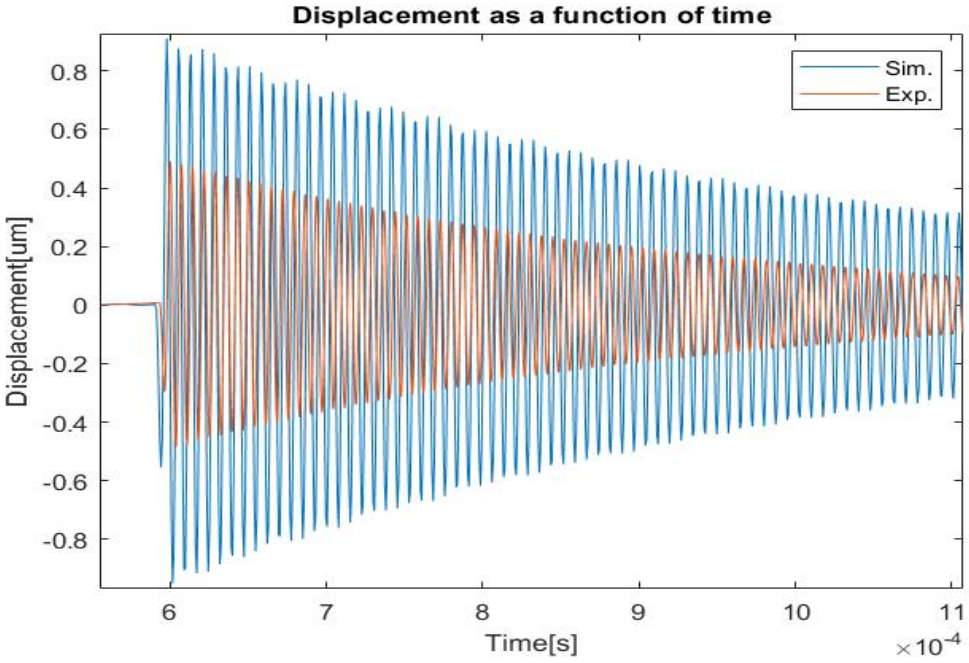

(b)

Figure 6.17: *a) Ring down comparison in Air. b) Ring down comparison in vacuum.*

By analyzing in more detail the graphs, some considerations can be done and the values of Q factor and amplitude of displacement can be computed. The former parameter is measured through two several methods and both give the same result. They are the exponential fitting of the envelope and the logarithmic decrement. Starting from the Eq.6.2 between the damping parameter ζ, Q factor, exponential coefficient α and the angular rate ω.

$$Q = \frac{1}{2 \cdot \zeta} = \frac{\omega}{2 \cdot \alpha} \tag{6.2}$$

In case of exponential fitting the parameter α is determined by the envelope using a MATLAB script (Fig.6.18a) while on the other hand the logarithmic decrement exploits the coefficents showed in Fig.6.18b.

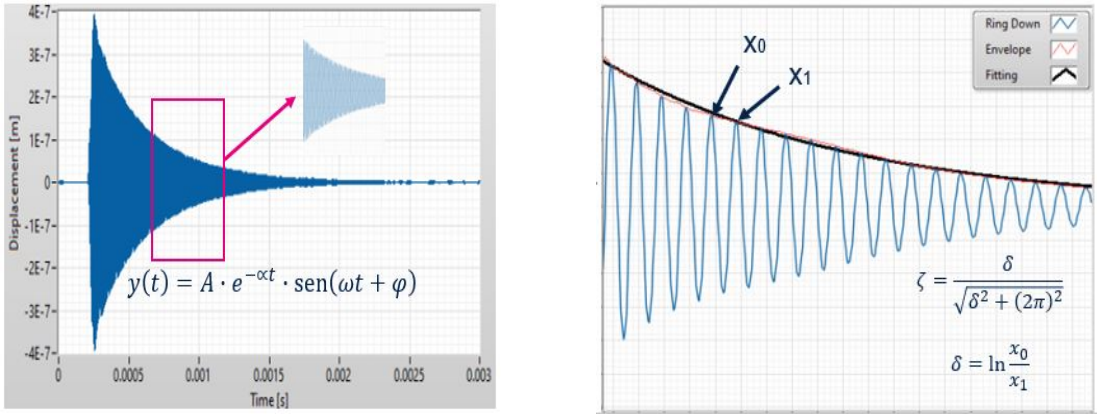

(a) *(b)*

Figure 6.18

In case of air, the values are resumed in the following table 6.6 while the results in vacuum in table 6.7:

	Exper.	Simul.	Error %
Q factor	22	27	18.5
Max amplitude (peak-peak) [nm]	921	1834	50

Table 6.6: *Summary table: ring down air.*

	Exper.	Simul.	Error %
Q factor	182	208	12.5
Max amplitude (peak-peak) [nm]	973	1850	47

Table 6.7: *Summary table: ring down vacuum.*

In both cases the following results are obtained: a relative good matching in Q factor values but at the same time an high error in the displacement amplitude. In the light of these value, it is possible to say that the damping phenomena involved in the two cases are well modelled unlike

the piezoelectric parameters. Indeed, the linear piezoelectric constitutive law and its coupling coefficients implemented in Comsol are not able to match the experimental evidences in case of time dependent driving voltage. It is necessary to develop a new non linear hysterical model able to take into account also this variable stimulus and reduce the error.

The 50% mismatch in term of displacement amplitude is observed with all the driving voltage both in vacuum and in air. In Fig.6.19 the linear increment of the experimental and simulated amplitudes in vacuum as a function of the AC voltage applied are shown.

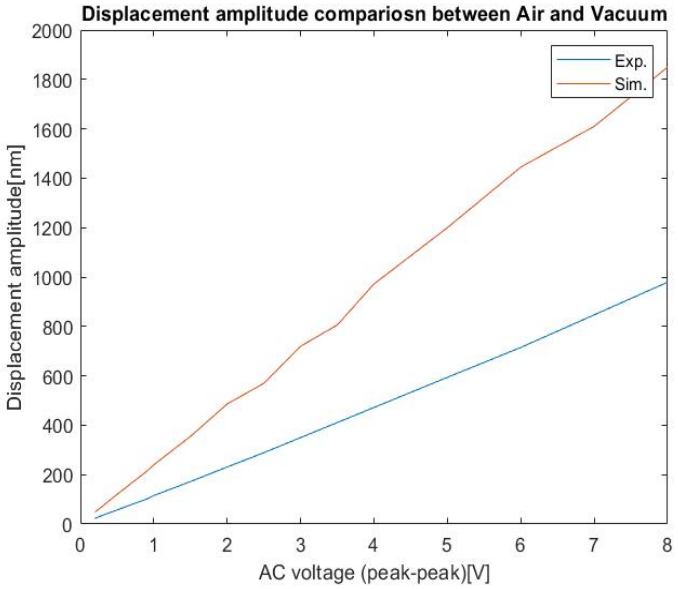

Figure 6.19: *Linear increment of the displacement's amplitude in vacuum: experimental and simulated ones.*

6.5 Cross-talk

The cross-talk characterization is aimed at evaluating the interaction between membranes within the same die. Its presence is clearly visible in Fig.6.20.

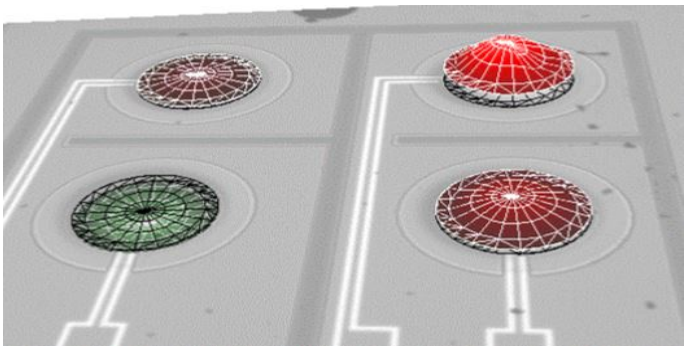

(a)

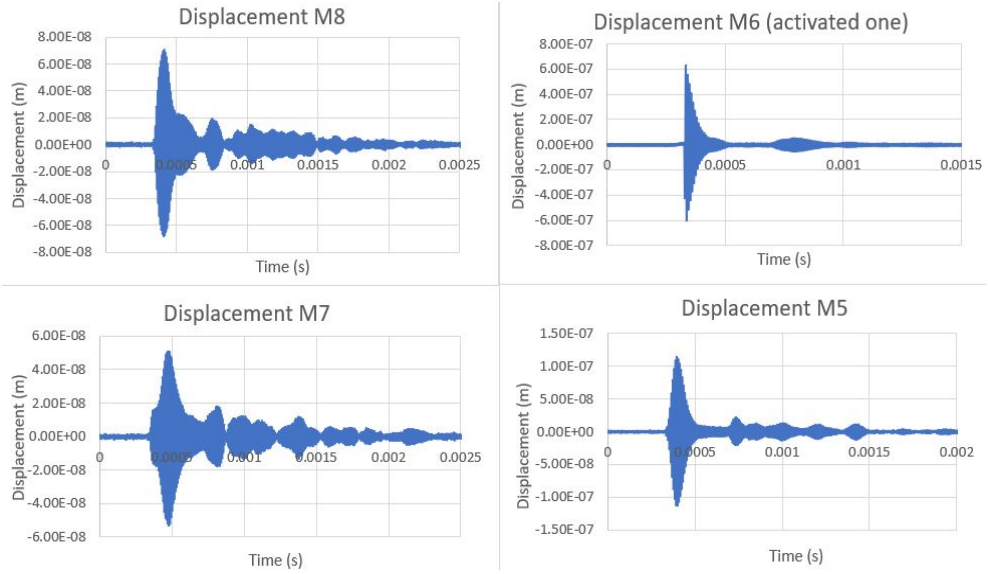

(b)

Figure 6.20: *a) Cross talk displacement of the membranes within the same quadrant in air. Even if only the top-right membrane is activated through a 4DC and 4AC voltage, all the membranes experience a displacement. Of course the order of magnitude is much lower than that of the activated one. b) Ring down of the four membranes. The arrangement of the graph is equal to that of the membranes of the top image.*

This experimental evidence of the presence of the cross-talk offers another explanation of the mismatch in the displacement amplitude. Indeed, a percentage of the electric energy of the driving voltage is exploited to put in motion the close membranes and not the desired one. Once the presence of the cross-talk is highlighted, the discussion moves on the results of the maximum displacement's amplitude of the membranes' centre of two entire dice in case of air and vacuum. In such a way it is possible to split the acoustic cross-talk from the mechanical one: ideally in vacuum the acoustic component is null. In the following figures 6.21, the numerical

values obtained are resumed. Before looking at the results it is worth to say that the 4x4 table faithfully represents the arrangement of the membranes on the device (see Fig.5.25). Moreover, it is chosen to use yellow color to point out the activated membranes, red to highlight the one with the highest displacement and green for the one with the lowest oscillation. Each quadrant is studied separately.

Air DIE 1, Max Ampl. [nm]			
132	206	155	78
158	1159	1218	71
143	1238	1142	44
106	234	140	70
Vacuum DIE 1, Max Ampl. [nm] and variation [%]			
70(-48%)	18(-91%)	19(-88%)	50(-35%)
32(-80%)	1260(+8%)	1296(+6%)	58(-19%)
24(-83%)	1314(+5%)	1230(+7%)	46(+5%)
41(-62%)	96(-59%)	49(-65%)	18(-75%)

(a)

Air DIE 2, Max Ampl. [nm]			
83	179	134	62
84	1085	1095	31
123	1097	1111	28
94	190	129	64
Vacuum DIE 2, Max Ampl. [nm] and variation [%]			
55(-34%)	33(-81%)	27(-80%)	35(-44%)
32(-62%)	1159(+6%)	1172(+6%)	42(+35%)
40(-67%)	1174(+6%)	1185(+6%)	51(+82%)
28(-70%)	33(-82%)	22(-83%)	39(-39%)

(b)

Figure 6.21: *Maximum displacement amplitude (peak-peak) in Air and Vacuum. Each quadrant is analyzed separately and only the central membrane (yellow) is activated. The membrane within the quadrant with the lowest displacement is represented in green while the one with the highest value of displacement in red.*

By analysing the tables the following conclusions can be made:

- The activated membranes experiences slightly higher displacement in vacuum.
- Except for three membranes, all the others show less displacement in vacuum. This evidence is strictly related to the elimination of the acoustic cross-talk: in vacuum only the mechanical cross-talk link each other the membranes' behaviour.

- In air, there is a clear pattern regarding the membranes with greater and lesser displacement. The pattern disappears in vacuum.

As regards to the consequences of the cross-talk in terms of frequency, it is noted that the frequency spectrum is distorted in air. Indeed, additionally to the main peak some secondary peaks appear and these are related to the resonance frequency of the close membranes. In order to clarify this concept, the frequency response of the membranes belonging to a quadrant are shown both in air and vacuum (Fig.6.22).

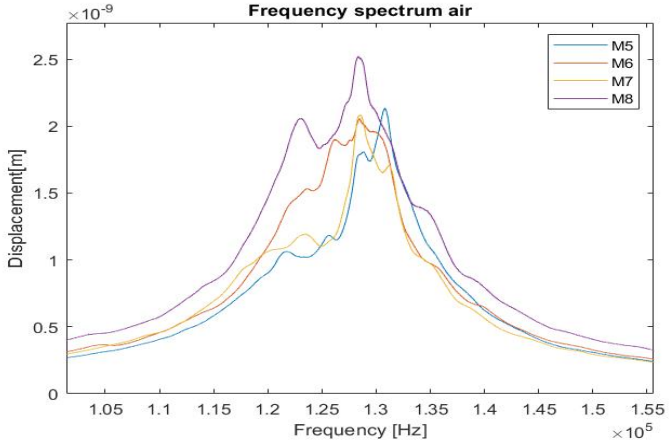

(a)

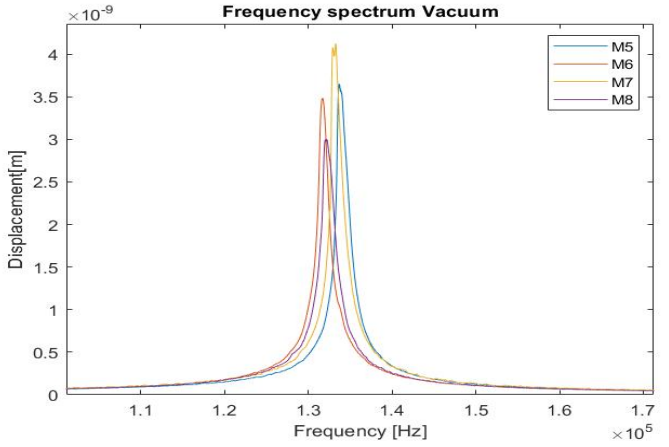

(b)

Figure 6.22: *Frequency spectrum of the membranes of the left-bottom quadrant. a) In air with mechanical and acoustic cross-talk. Secondary peaks are visible and of course the presence of air enlarges the bandwidth as shown in Fig.2.12. b) In Vacuum with the mechanical cross-talk only.*

6.6 Radiation patterns of the acoustic field and sound pressure

The last section of this master thesis shows the results of the acoustic characterization. These are preliminary results and a better investigation of the acoustic field emitted by the device will be done in future STMicroelectronics' activities. Indeed, the initial aim to compute and compare the experimental and simulated radiation patterns has not been achieved: in this section I have limited myself to insert the radiation patterns obtained by means of the model simulation. Conversely, it has been possible to compare the sound pressure level evaluated at 2 cm from the activated membrane over time. Both in the experimental measurement and the simulation, the selected driving voltage is a single sinusoidal pulse with 4DC, 4AC and resonance frequency of the membrane.

Starting from the radiation pattern, in Fig.6.23 the results in db and Pa are shown. As it is already explained in section 5.8, they are computed on a circular surface 6 cm away from the membrane.

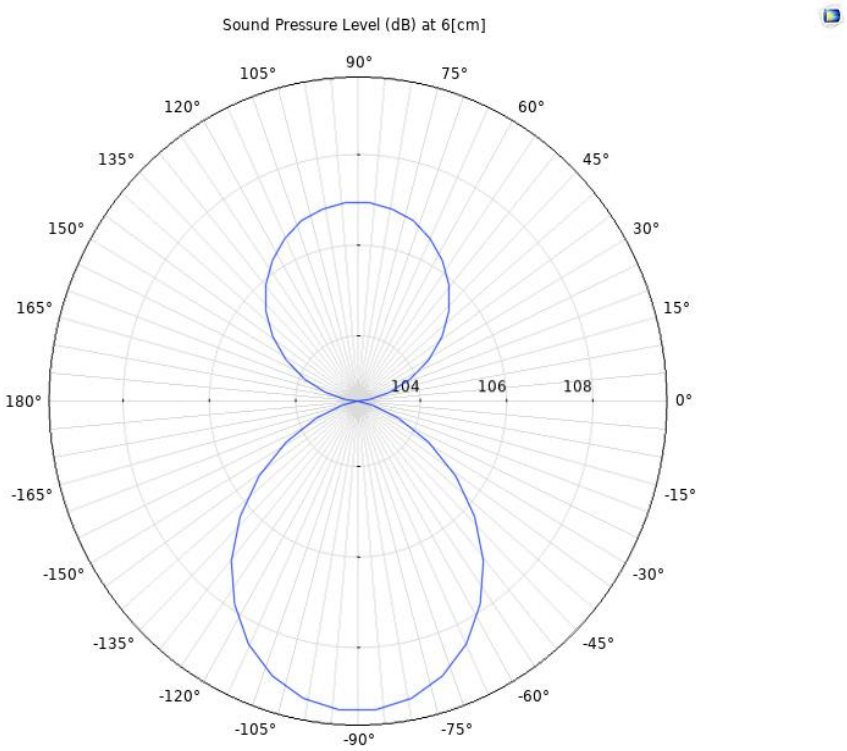

Figure 6.23: *Radiation Pattern at 6*cm *in dB. The direction corresponding to 90° is parallel to the positive z axis, while at 0° there is the positive direction of the axis x. Since the dB are not usual units of measurement, the equivalent value in Pa is the following: 106dB equal to 4*Pa

Looking at the figures, it is possible to note that the intensity of the sound pressure emitted is greater from below the cavity rather than upwards. This behavior can also be visualized through the surface graphs in Fig.6.24.

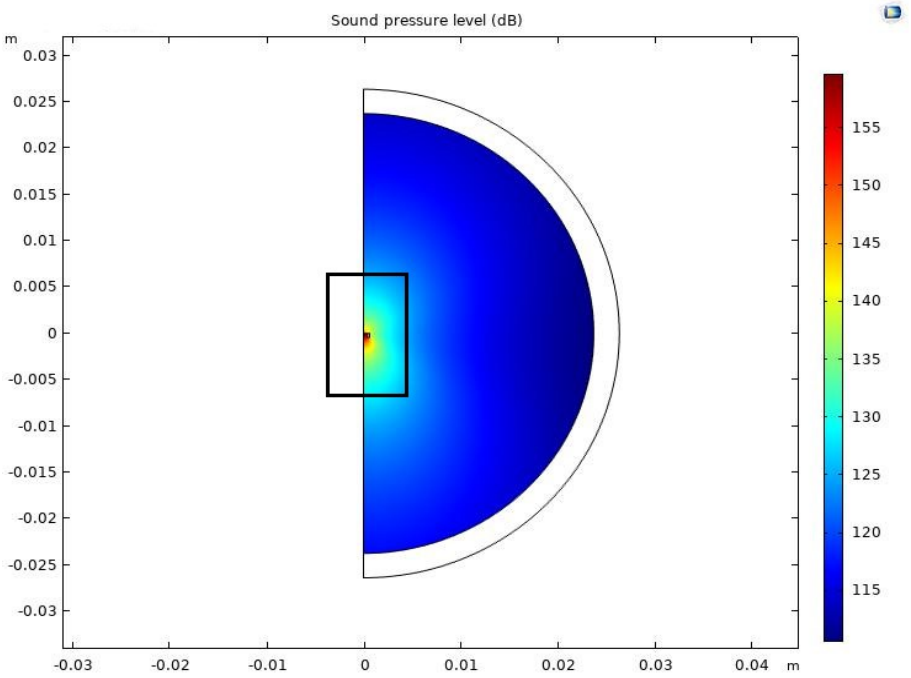

(a)

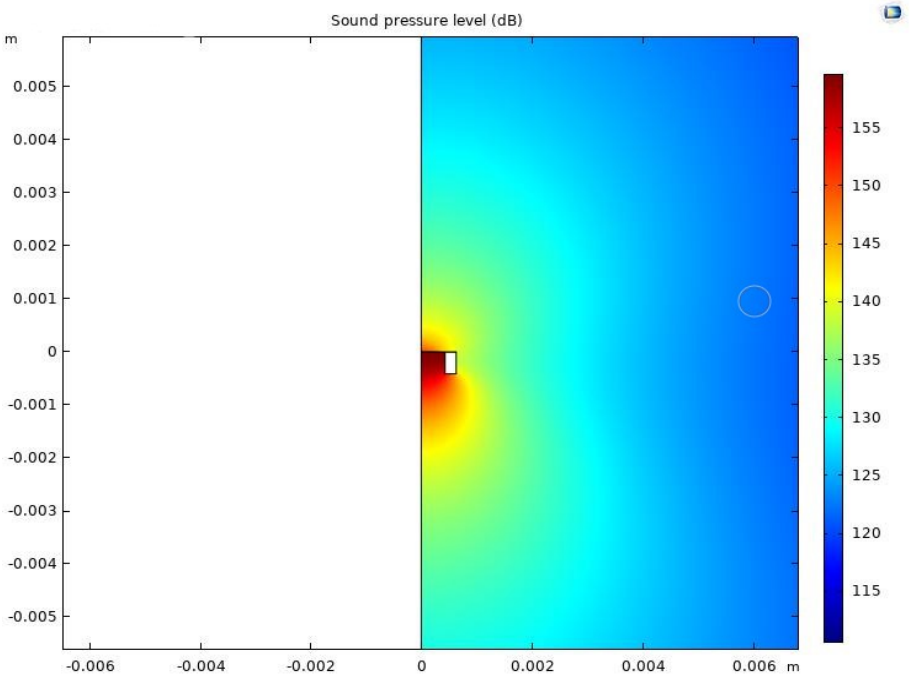

(b)

Figure 6.24: *a) Sound pressure level (SPL) in the all the fluid domain. b) Detail of the Sound pressure level around the single membrane structure.*

The presence of the cavity increases the sound intensity as if this behaves as an amplifier able to confine the acoustic field emitted. Moreover, once the wave-front achieves the end of the cavity the acoustic field is sent over a higher angular amplitude. This is a quite interesting an unexpected discover and a similar concept could be exploited for increasing the upward intensity. Indeed, a rigid amplifier could be fabricated even above the membrane and in such a way obtaining a higher sound pressure level. Simultaneously, it must be taken into account that the focusing of the emitted field would decrease.

After the presentation of the radiation patterns, the discussion moves toward the comparison of the pressure at 2cm between simulation and experimental test. The values of pressure as a function of time are shown in Fig.6.25.

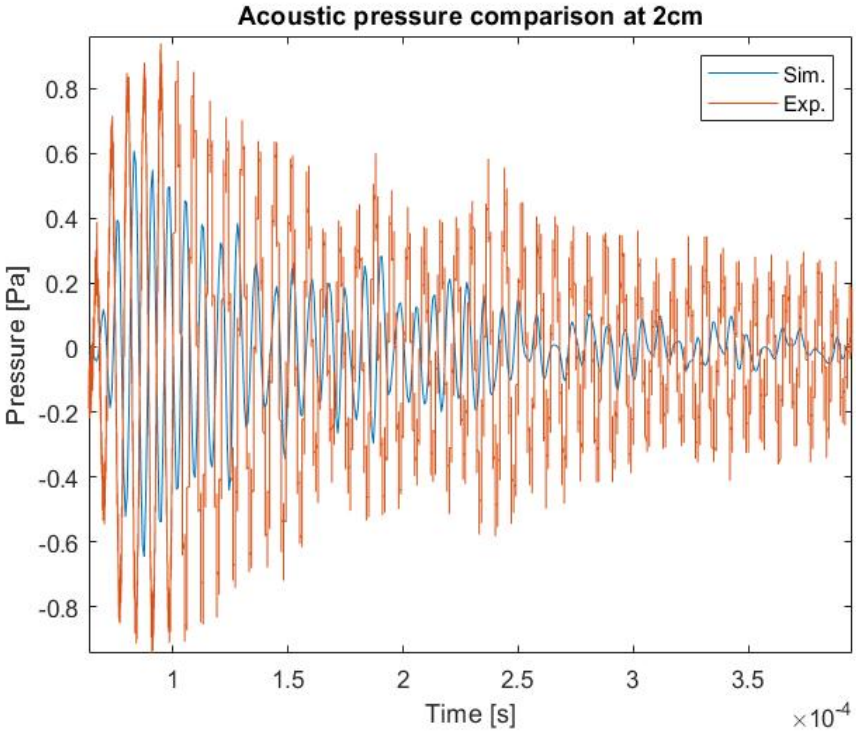

Figure 6.25: *Comparison between the acoustic pressure measured through Comsol simulation and experimentally. Its value is measured at* 2cm *above the membrane's centre.*

Looking at the previous figure, a mismatch between simulation and experimental results is obtained. Conversely to the oscillation ring down, in this case the experimental pressure overestimates the simulated one. This evidence can be explained by taking into account several reasons. The first one could be related to the different attenuation phenomena occurring in the model than the reality. While the second can deal with the cross-talk phenomena. The experimental cross-talk oscillation of membranes close to the activated one can emit an acoustic perturbation which interfere positively with the sound pressure emitted by the activated one: in such a way the ultrasound wave increases its intensity. This phenomena of cross-talk is not completely simulated by the simulation model. Indeed, the fluid domain through which the acoustic cross talk occurs, is modelled only on the top part of the device: the posterior cavities

of the membranes do not have a common fluid through which they can communicate with each other. A new model able to simulate this effect should be built in order to measure a coherent value of pressure intensity.

Chapter 7

Conclusions

In this master thesis several investigations have been carried out with the aim of completely characterizing the mechanical behavior of a PMUT and to start an acoustic analysis of the emitted acoustic field. The design of the device is provided by STMicroelectronics and its main features concern the removal of passivisation over the membranes and the trench to minimize cross-talk phenomena. This device is able to send and receive ultrasonic waves exploiting the piezoeletric effect: all the studies are focused on the sending mode only.

The selected approach to perform the analysis is constituted by a continuous parallelism between numerical simulation and experimental evidences. In such a way, a complete vision of the whole characterization process has been possible. The campaign of measurements includes the static topography of the device, the dynamic vibrometry after an AC voltage application in time domain and the sound pressure level measurements. Both in the simulations and in the experimental part, the same set up conditions have been chosen to guarantee a consistency to the comparison.

First of all, the deformed configuration of the membranes is studied. This non flat state is due to the residual stresses introduced through the manufacturing process; in particular, they are a consequence of the mismatch between the coefficients of thermal expansion of each layer that constitutes the membrane stack. The initial profile is upwards and the center of the membrane is shifted by 7.04 µm to the z^+ axis. Moreover, its variation as a function of a DC voltage applied is analyzed. Since the piezoelectric layer (PZT, Lead Zirconate Titanate) is characterized by a electro-mechanical coupling behavior, the stress state within the material changes upon the application of a voltage. The configuration flattens as the DC voltage increases and this experimental evidence is well simulated by both the 2D and the 3D models. The alignment reassures us about the reliability of the geometry design, the mechanical elastic parameters and residual stresses chosen for each material and the goodness of the piezoelectric model implemented in Comsol in simulating the electro-mechanical static coupling.

Secondly, always by using the tomography measurements, the deformation of the entire die is investigated. Even in this case, the distorted shape is due to the residual stresses but also to the curing process of the epoxy glue used to attached the device on the printed circuit board (PCB). In order to simulate this deformed configuration, a model of the whole device was necessary: after an iterative working flow a good alignment is achieved between real device and simulated one. The main boundary conditions applied concern fixed vertices, springs on the edges with a characteristic stiffness and a force per unit of surface toward the positive direction of z axis.

The configuration obtained will be then exploited in the ring down analysis: the oscillation ring down must be analyzed on a model of the whole die because a single membrane model does not fit properly the boundary conditions of the real device.

After the topography measurements, the attention moves toward the frequency analysis. This is performed by sending a chirp signal (DC voltage in combination with an AC with small amplitude) in a range of frequency between 100kHz and 450kHz. Through this characterization has been possible to compute the resonance frequencies of the vibration and in turn the frequency of the acoustic field emitted. The average experimental values for the first six modes at V=0 are equal to 140, 207, 215, 321, 325 and 387kHz. In addition, its dependence on DC voltage is analyzed and it is demonstrated how the frequency values decrease as the voltage increases. Basically, the upward configuration flattens as the DC voltage increases and subsequently the structure of the device becomes less rigid. The experimental scenario has been properly fitted by Eigenfrequency study performed: the 2D model only fits the centre symmetric vibrations (1^{st} and 6^{th} modes) while the 3D is able to simulate all modes.

Once the deformed state of the whole device and the resonance frequency of piston-like vibration are known, it is possible to send an AC signal to the thin film piezoelectric layer and investigating the dynamic vibration by using polytec in vibrometry configuration. The measurements are performed both in air and in vacuum and the values of Q factor respectively 22 and 182 are almost matched by the Comsol model. This means that the modelling of the damping by means of the loss factors and thin-film damping at the interface between structure and fluid almost reproduces the reality in both cases. Moreover, it is noted that the results' dispersion between experimental measurements is not null. At the same time, the ring down analysis has highlighted some limitations of piezoelectric model used. In contrast to the static case (DC only), the dynamic actuation is not well reproduced in terms of displacement amplitudes: the linear model implemented in Comsol is not able to simulate the real effect within the PZT layer. With respect to this limit, it will be mandatory to remodel the non linear hysterical piezoeletric behavior starting from the typical polarization curves of the material in order to match the dynamic behavior.

Then, the phenomena of cross talk between membranes belonging to the same die was investigated. It is noted that this unwanted effect is due to mechanical and acoustic contributions respectively. The interaction between membranes has been demonstrated experimentally and it has also been possible to divide the acoustic and mechanical contribution by testing in air (both) and then in vacuum (mechanical only). The main responsible is the acoustic component and in particular the interaction occurs through the back side of the device. For this reason, one of the future developments will be to design a new geometries with closed cavity to reduce as much as possible communication between membranes or alternatively to better model the cavities with a communicating fluid between cavities' membranes. Moreover, this effect allows another explanation of the mismatch in the displacement amplitude: part of the electric energy is lost to put in motion the others membranes and not the desired one.

Lastly, the acoustic characterization is carried out. I have limited myself to the analysis of the simulated radiation patterns and a comparison of the pressure over time at two 2cm above the membrane. The former model has given interesting results in terms of higher angle of emission and higher sound pressure through the cavity than from the top. Of course, this model is limited by the 2D-axisymmetric condition: in future analysis a more realistic 3D model should be used. On the other hand, the time dependent measurement of the pressure intensity shows

a mismatch: the maximum experimental pressure intensity is equal to almost 1Pa while the simulated one achieves at most 0.6Pa. Once again, this error is given by the cross-talk presence. Indeed, the experimental pressure has higher value because of the positive interference between the acoustic field emitted by the activated membrane and the close ones. A new model able to take into account the cross-talk oscillations should be realized in future activity. Moreover, another acoustic study to be performed in future works is related to the steering control of the ultrasound field.

The PMUT world is just at the beginning of its journey and further investigations will be needed as described in this conclusion section. My work is a starting point to model new design by considering the elastic, piezo, damping parameters and boundaries conditions used to reproduce the experimental evidences.

Bibliography

[1] K.-M. Hu, P. Bo, X.-Y. Li, Y.-H. Xin, X.-R. Bai, L. Li, and W.-M. Zhang, "Resonant nano-electromechanical systems from 2d materials," vol. 131, no. 5, p. 58 001, Sep. 2020. DOI: 10.1209/0295-5075/131/58001. [Online]. Available: https://doi.org/10.1209/0295-5075/131/58001 (cit. on p. 3).

[2] B. Vigna, "It makes sense: How extreme analog and sensing will change the world," in *Tech. Digest 2012 Solid-State Sensors, Actuators and Microsystems Workshop*, 2012, pp. 58–65 (cit. on p. 4).

[3] Y. Qiu, J. V. Gigliotti, M. Wallace, F. Griggio, C. E. M. Demore, S. Cochran, and S. Trolier-McKinstry, "Piezoelectric micromachined ultrasound transducer (pmut) arrays for integrated sensing, actuation and imaging," *Sensors*, vol. 15, no. 4, pp. 8020–8041, 2015, ISSN: 1424-8220. DOI: 10.3390/s150408020. [Online]. Available: https://www.mdpi.com/1424-8220/15/4/8020 (cit. on pp. 5, 10, 15).

[4] A. Corigliano, B. De Masi, A. Frangi, C. Comi, A. Villa, and M. Marchi, "Mechanical characterization of polysilicon through on-chip tensile tests," *Journal of Microelectromechanical Systems*, vol. 13, no. 2, pp. 200–219, 2004. DOI: 10.1109/JMEMS.2003.823221 (cit. on p. 5).

[5] A. Corigliano, R. Ardito, C. Comi, A. Frangi, A. Ghisi, and S. Mariani, *Mechanics of Microsystems*. John Wiley & Sons, 2017 (cit. on pp. 6, 16, 24, 26, 37, 55).

[6] Y. Lu and D. A. Horsley, "Modeling, fabrication, and characterization of piezoelectric micromachined ultrasonic transducer arrays based on cavity soi wafers," *Journal of Microelectromechanical Systems*, vol. 24, no. 4, pp. 1142–1149, 2015 (cit. on p. 7).

[7] S. Timoshenko and S. Woinowsky-Krieger, "Theory of plates and shells," 1959 (cit. on p. 7).

[8] P. Muralt, N. Ledermann, J. Paborowski, A. Barzegar, S. Gentil, B. Belgacem, S. Petitgrand, A. Bosseboeuf, and N. Setter, "Piezoelectric micromachined ultrasonic transducers based on pzt thin films," *IEEE Transactions on Ultrasonics, Ferroelectrics, and Frequency Control*, vol. 52, no. 12, pp. 2276–2288, 2005. DOI: 10.1109/TUFFC.2005.1563270 (cit. on pp. 7, 8).

[9] M.-A. Dubois and P. Muralt, "Pzt thin film actuated elastic fin micromotor," *IEEE transactions on ultrasonics, ferroelectrics, and frequency control*, vol. 45, no. 5, pp. 1169–1177, 1998 (cit. on p. 8).

[10] D. Akai, T. Katori, D. Takashima, and M. Ishida, "Sensitivity and resonance frequency with changing the diaphragm diameter of piezoelectric micromachined ultrasonic transducers," in *AIP Conference Proceedings*, AIP Publishing LLC, vol. 1709, 2016, p. 020 010 (cit. on pp. 8, 9).

[11] G. Massimino, L. D'Alessandro, F. Procopio, R. Ardito, M. Ferrera, and A. Corigliano, "Air-coupled pmut at 100 khz with pzt active layer and residual stresses: Multiphysics model and experimental validation," in *2017 18th International Conference on Thermal, Mechanical and Multi-Physics Simulation and Experiments in Microelectronics and Microsystems (EuroSimE)*, 2017, pp. 1–4. DOI: 10.1109/EuroSimE.2017.7926253 (cit. on p. 8).

[12] G. Massimino, B. Lazarova, F. Quaglia, and A. Corigliano, "Air-coupled pmuts array with residual stresses: Experimental tests in the linear and non-linear dynamic regime," *International Journal of Smart and Nano Materials*, vol. 11, no. 4, pp. 387–399, 2020 (cit. on pp. 9, 37).

[13] A. Dangi and R. Pratap, "System level modeling and design maps of pmuts with residual stresses," *Sensors and Actuators A: Physical*, vol. 262, pp. 18–28, 2017, ISSN: 0924-4247. DOI: https://doi.org/10.1016/j.sna.2017.05.006. [Online]. Available: https://www.sciencedirect.com/science/article/pii/S0924424716308391 (cit. on p. 9).

[14] F. Akasheh, T. Myers, J. Fraser, S. Bose, and A. Bandyopadhyay, "Development of piezoelectric micromachined ultrasonic transducers," *Sensors and Actuators A: Physical*, vol. 111, pp. 275–287, Mar. 2004. DOI: 10.1016/j.sna.2003.11.022 (cit. on p. 11).

[15] H. Choi, A. Dalakoti, S. Bose, and A. Bandyopadhyay, "Influence of top electrode design on pmuts performance," *Sensors and Actuators A: Physical*, vol. 135, no. 2, pp. 613–619, 2007, ISSN: 0924-4247. DOI: https://doi.org/10.1016/j.sna.2006.08.022. [Online]. Available: https://www.sciencedirect.com/science/article/pii/S0924424706005553 (cit. on p. 12).

[16] A. Corigliano and A. Frangi, "Lecture notes, material engineering and nanotechnology, mems course," (cit. on pp. 13, 16, 25).

[17] *Carson bandwidth rule* (cit. on p. 14).

[18] E. Defaÿ, *Integration of ferroelectric and piezoelectric thin films: concepts and applications for microsystems*. John Wiley & Sons, 2013 (cit. on pp. 16–18).

[19] M. Ahart, M. Somayazulu, R. Cohen, P. Ganesh, P. Dera, H.-k. Mao, R. J. Hemley, Y. Ren, P. Liermann, and Z. Wu, "Origin of morphotropic phase boundaries in ferroelectrics," *Nature*, vol. 451, no. 7178, pp. 545–548, 2008 (cit. on p. 19).

[20] M. Panjan, *Ferroelectrics and ferroelectric domains*, 2003 (cit. on p. 20).

[21] Y. Lu and D. A. Horsley, "Modeling, fabrication, and characterization of piezoelectric micromachined ultrasonic transducer arrays based on cavity soi wafers," *Journal of Microelectromechanical Systems*, vol. 24, no. 4, pp. 1142–1149, 2015 (cit. on p. 20).

[22] T. Iijima, S. Osone, Y. Shimojo, and H. Nagai, "Synthesis of a few um thick lead zirconate titanate films on 2-in. si substrates for piezoelectric film devices," *International journal of applied ceramic technology*, vol. 3, no. 6, pp. 442–447, 2006 (cit. on p. 21).

[23] G. Shilpa, K. Sreelakshmi, and M. Ananthaprasad, "Pzt thin film deposition techniques, properties and its application in ultrasonic mems sensors: A review," vol. 149, no. 1, p. 012 190, 2016 (cit. on pp. 21–23).

[24] E. Defay, "Growth and microsystem, luxembourg institute of science and technology," (cit. on p. 22).

[25] I. Kanno, "Piezoelectric pzt thin films: Deposition, evaluation and their applications," pp. 785–788, 2019 (cit. on p. 23).

[26] K. Tsuchiya, T. Kitagawa, and E. Nakamachi, "Development of rf magnetron sputtering method to fabricate pzt thin film actuator," *Precision Engineering*, vol. 27, no. 3, pp. 258–264, 2003, ISSN: 0141-6359. DOI: https://doi.org/10.1016/S0141-6359(03)00006-0. [Online]. Available: https://www.sciencedirect.com/science/article/pii/S0141635903000060 (cit. on p. 23).

[27] G. Massimino, "Modellazione e simulazione di un micro trasduttore ultrasonico piezoelettrico," 2016 (cit. on p. 24).

[28] O. Thomas, "Dynamique linéaire et non linéaire de structures élastiques et pi'ezo'electriques. Instruments de musique, micro/nano systèmes électromécaniques, contrôle de vibration," Habilitation à diriger des recherches, École normale supérieure de Cachan - ENS Cachan, Nov. 2011. [Online]. Available: https://tel.archives-ouvertes.fr/tel-00718727 (cit. on p. 26).

[29] H. Kuttruff, *Room acoustics*. Crc Press, 2016 (cit. on p. 28).

[30] P. Filippi, D. Habault, J. P. Lefebvre, A. Bergassoli, and R. Raspet, *Acoustics: Basic physics, theory and methods*, 2000 (cit. on pp. 29, 31).

[31] G. Massimino, "Modelling and simulation of piezoelectric micromachined ultrasonic transducers," 2020 (cit. on pp. 29, 31).

[32] A. Corigliano and A. Taliercio, *Meccanica computazionale: soluzione del problema elastico lineare*. Società Editrice Esculapio, 2006 (cit. on pp. 46, 48).